

Habilitation à Diriger des Recherches

Université Pierre et Marie Curie — Sorbonne Universités

Ecole Normale Supérieure — Département de Physique
Laboratoire Pierre Aigrain

présentée par
Carole Diederichs

**The resonance fluorescence of single semiconductor quantum dots for the
generation of indistinguishable photons**

Soutenue le 7 décembre 2016 devant le jury composé de :

M. Alberto Bramati	Examineur
M ^{me} Sara Ducci	Examinatrice
M. Brian Gerardot	Rapporteur
M. Xavier Marie	Rapporteur
M. Peter Michler	Rapporteur (absent)
M ^{me} Valia Voliotis	Membre invité

Contents

Preface	5
Introduction	7
1 The semiconductor quantum dots in the artificial atom model	9
1.1 General properties of semiconductor quantum dots	9
1.2 The artificial atom model and its limits	17
1.3 The resonant excitation: a way to overcome these limits?	23
1.4 Conclusion	28
2 Measurement of the resonance fluorescence of single quantum dots	29
2.1 Strictly resonant excitation experimental setup	29
2.2 Quenching of the resonance fluorescence	32
2.3 Optical control of the resonance fluorescence	34
2.4 Retrieval of the properties of a quasi-ideal two-level system	41
2.5 Conclusion and perspectives for achieving the radiative limit	45
3 The specificity of the resonance fluorescence of single quantum dots	47
3.1 Spectral properties	48
3.2 Photon statistics	54
3.3 The resonant Rayleigh scattering regime	59
3.4 Conclusion	61
4 Photon indistinguishability in the resonant Rayleigh scattering regime	63
4.1 Two-photon interference experiment	63
4.2 Photon indistinguishability under resonant excitation	68
4.3 The coalescence time window	71
4.4 Control of the coalescence time window	74
4.5 Conclusion	76
Conclusion	77
Bibliography	79

Preface

This manuscript gathers the experimental and theoretical works that have been performed on the subject of the resonance fluorescence in single semiconductor quantum dots for the generation of indistinguishable photons, since my nomination as an Assistant Professor at "Université Pierre et Marie Curie" (UPMC), in the coherent and non-linear optics group of "Laboratoire Pierre Aigrain" (LPA). The study of this field emerged step by step in our group after the experimental implementation of a confocal micro-photoluminescence setup specially suited for high resolution spectroscopy of single quantum dots. The studies of Cécile Kammerer [1], Ivan Favero [2] and Alice Berthelot [3] during their PhD thesis, under the supervision of Guillaume Cassabois and Philippe Roussignol, and in close collaboration with the theoreticians Robson Ferreira and Gérard Bastard, highlighted the important role of the solid state environment in the optical properties of a single quantum dot. The investigations of the resulting dephasing processes that are responsible for the degradation of the coherence of the emitted photons led to the questioning of the artificial atom picture where a single quantum dot is considered as an ideal two-level system [4]. In the current context of the development of integrated sources of indistinguishable photons for quantum optics applications, these studies raised the need of implementing in the group a new project devoted to the measurement of the resonance fluorescence of single quantum dots.

My contribution in this project as a permanent LPA member started in 2008, in collaboration with Guillaume Cassabois until his nomination in 2010 as a Professor in the University of Montpellier. It consisted in the conception and the implementation of an original experimental setup based on an orthogonal excitation-detection geometry in order to measure the resonance fluorescence of single quantum dots. At the time this challenging setup was developed, the success of such strictly optical resonant excitation configuration was reported in only two papers [5, 6]. I naturally greatly benefited from the existing experiment, but I also initiated a new field of expertise in the group with the development of quantum optics experiments to measure the emission statistics of a light source with a Hanbury-Brown and Twiss interferometer as well as the indistinguishability degree of the emitted photons with a Hong-Ou-Mandel interferometer. The work presented in this manuscript results from the two PhD theses carried out by Hai Son Nguyen [7] and Raphaël Proux [8] that I directly supervised, with the decisive input of Grégory Sallen and Maria Maragkou during their post-doctorate, and of the LPA permanent members Robson Ferreira and Emmanuel Baudin for the theoretical parts.

Introduction

This manuscript aims at presenting a review of our work on the resonance fluorescence of single quantum dots (QD) at low temperature ($T = 10$ K) for the generation of indistinguishable photons. At the time this work was done, the context was based on the fact that the semiconductor QDs were commonly considered as artificial atoms. This analogy led to an important development of experiments in the field of cavity quantum electrodynamics with semiconductor QDs, similarly to other systems like atoms [9], trapped ions [10], molecules [11], or colored centers in diamond [12]. The QDs constitute in fact promising candidates for the realization of integrated single photon emission devices in the contexts of fundamental quantum optics experiments or quantum information applications. From the pioneering work of P. Michler *et al.* where intensity correlation measurements on the photoluminescence signal of single QDs brought the experimental evidence of the quantum nature of the QD radiation [13], subsequent experiments demonstrated the possibility to use single QDs for the generation of polarization-entangled single photon pairs [14, 15], or indistinguishable single photons [16]. In all these studies, it appeared that an important general issue to get reliable QD-based devices was to reach the so-called fundamental radiative limit $T_2 = 2T_1$ (T_1 being the population lifetime and T_2 the coherence lifetime), where the linewidth of the photoluminescence spectrum corresponds to its lower limit $2\hbar/T_2 = \hbar/T_1$. Several strategies have been then followed in that sense such as the shortening of the population lifetime induced by the Purcell effect [16, 17], or the reduction of the pure dephasing by resonant excitation [5, 6, 18]. As expected from the studies already performed in our group on the dephasing processes in single QDs, the resonant configuration was in fact an efficient strategy for minimizing the residual excitation of the QD environment that acts as a fluctuating reservoir for spectral diffusion. Since the first direct measurement of the optical response of single QDs under resonant excitation performed by A. Muller *et al.* [5], many results on resonance fluorescence in single QDs were presented in the literature [6, 18–21], showing the intrinsic properties of a solid state two-level system (TLS) such as for example the Rabi oscillations [5, 6, 22] or the Mollow triplet [22]. However, the radiative limit was never reached even at very low temperature, suggesting that a fluctuating electrostatic environment which influences the QD coherence still exists, even in case of resonant excitation where the laser photo-creates carriers only in the QD. It is in this context that the work presented in this manuscript fits.

Chapter 1 first introduces the general properties of single semiconductor QDs such as the discretization of the energy spectrum due to the three dimensional confinement of the carriers, the selection rules of the interband optical transitions when the system is coupled to light and the "pseudo" exciton along with the complementary exciton complexes which can populate a single QD. The artificial atom model where, analogously to atomic systems, a single QD is described as a TLS, is then presented: the important implications in quantum optics such as the emission of antibunched photons, but also the limitations caused by the population and the coherence relaxation mechanisms are discussed. It highlights the problematic of the work

presented in this manuscript, namely the requirement of a resonant excitation configuration in order to manipulate a genuine solid-state TLS in a single QD. As an introduction to the experimental results presented in the following chapters, the specificity of the resonance fluorescence emission of a TLS under resonant excitation is presented.

Chapter 2 first presents the experimental setup that was developed to measure the resonance fluorescence of a single QD. It then focuses on the study of the inhibition of the exciton resonance fluorescence induced by the residual doping of the sample, a phenomenon which turns out to be widely met in the QD community. We show that the resonance fluorescence can be retrieved by the mean of an additional non-resonant laser which controls the charge state of the fundamental transition of the QD. The effect of this optical gate is studied by characterizing the resonance fluorescence along with the gate dynamics and the emission statistics as a function of the gate power. These experimental results are supported by a theoretical study based on a random population model which describes the carriers capture mechanisms involved in the gating effect of the resonance fluorescence. The main properties of the resonance fluorescence are restored by the optical gate and the QD then behaves as a quasi-ideal TLS. However, the radiative limit is not perfectly reached contrarily to what is expected for a resonantly-driven TLS, which shows that an additional level of control of the fluctuating electrostatic environment is needed. This work is part of the PhD thesis of H. S. Nguyen [7] and has been published in Ref. [20, 23].

Chapter 3 is devoted to the specificity of the resonance fluorescence in single QDs under continuous wave (cw) excitation. The spectral properties are studied by measuring the first-order correlation function in a Fourier transform spectroscopy setup, while the emission statistics is investigated by measuring the second-order correlation function in a Hanbury Brown and Twiss (HBT) interferometer. These functions exhibit very specific behaviors as a function of the power of the resonant laser, allowing us to differentiate the properties of the elastic and inelastic components which both contribute to the resonance fluorescence signal. In particular at low excitation power, the elastic component, which consists in the resonant Rayleigh scattering (RRS) of the incoming laser photons on the TLS transition, prevails and exhibits original spectral and emission statistics properties. In this regime, the coherence time of the emitted photons is tailored by the coherence of the excitation laser and thus largely exceeds the coherence imposed by the QD electronic properties, while the single photon emission statistics is maintained. Within such a regime, the radiative limit imposed by the QD electronic properties appears less drastic for the generation of highly indistinguishable photons than in the more conventional high power regime. This work is part of the PhD theses of H. S. Nguyen [7] and R. Proux [8], and has been published in Ref. [24].

Chapter 4 aims at showing that the photons emitted in the RRS regime present higher degrees of indistinguishability than the ones imposed by the radiative limit under non-resonant excitation or resonant excitation in the high power regime. The second-order correlation function measured in a two-photon interference Hong-Ou-Mandel (HOM) experiment is studied as a function of the resonant excitation power. After discussing the main fundamental differences between an HOM experiment performed under pulsed or cw excitation, we define a new figure of merit, the coalescence time window (CTW), which allows us to properly investigate the temporal indistinguishability of the photons emitted by a single photon source in the cw operating mode, and more specifically in the RRS regime. By studying the dependence of this CTW with the coherence time of the excitation laser, we show that the photon indistinguishability can be extended to unprecedented levels in the RRS regime. This work is part of the PhD thesis of R. Proux [8] and has been published in Ref. [25].

Chapter 1

The semiconductor quantum dots in the artificial atom model

In this first chapter, we present the general electronic and optical properties of InAs/GaAs semiconductor quantum dots (QD) grown by molecular beam epitaxy. When focusing on the fundamental excitonic transition, these systems can be seen as two-level systems (TLS) in the artificial atom picture because of the three dimensional confinement of the carriers. We introduce some examples of the implications of such artificial atom model regarding the development of QD-based devices for quantum information applications. Single QDs constitute in fact good candidates for the realization of integrated single photon sources. However, these solid state systems face intrinsic limits under non-resonant excitation which lead to the degradation of the coherence of the emitted photons. The main mechanisms responsible for the population relaxation and the decoherence of the emitted photons are presented before introducing the resonant excitation configuration which appears as the fundamental requirement for minimizing these dephasing processes and for considering a single QD as an ideal TLS. Finally, we present the main properties of the emission of a TLS under resonant excitation and we focus in particular on the specificity of the resonance fluorescence of a TLS which results from the elastic and the inelastic scattering of the incoming laser photons.

1.1 General properties of semiconductor quantum dots

1.1.1 Carriers confinement in semiconductors

The motion of the electrons in a solid is studied in the Born-Oppenheimer approximation, where the motion of the nuclei is considered negligible, and in the Hartree-Fock approximation, where a single electron is assumed to be in the average field created by the nuclei and the other electrons [26]. Within these approximations, the Hamiltonian describing the motion of one electron in a solid is:

$$H = \frac{\vec{p}^2}{2m} + V(\vec{r}) \quad (1.1)$$

where $V(\vec{r})$, the interaction potential between the electron and the crystal, shows the same symmetry properties as the crystal. Within the Bloch theorem, due to the periodic structure of the crystal, the eigenstates of the electron are described by the wave functions:

$$\psi_{n,\vec{k}}(\vec{r}) = u_{n,\vec{k}}(\vec{r})e^{i\vec{k} \cdot \vec{r}} \quad (1.2)$$

where $u_{n,\vec{k}}$ refers to the atomic part with the crystal symmetry, n the band index and \vec{k} the electron wavevector. The eigenenergies $E_n(\vec{k})$ of the eigenstates $\psi_{n,\vec{k}}(\vec{r})$ define the crystal energy bands. In particular, under the effective mass approximation, the band structure in the neighborhood of the Γ point (i.e. $\vec{k} = \vec{0}$) can be assimilated to a parabola defined by:

$$E_{n,\vec{k}} = E_{n,0} + \frac{\hbar^2 \vec{k}^2}{2m_{e,n}^*} = E_{n,0} + \frac{\hbar^2}{2m_{e,n}^*} (k_x^2 + k_y^2 + k_z^2) \quad (1.3)$$

where $m_{e,n}^*$ is the electron effective mass in band n . The electronic properties of a solid are thus described by quasi-particles with the effective mass of the corresponding band.

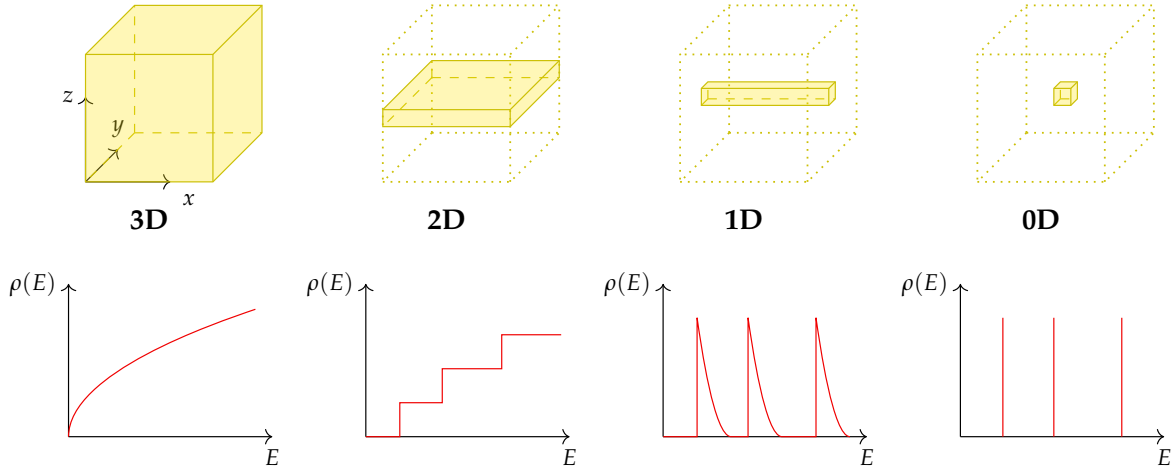


Figure 1.1: Density of states of various low dimensions semiconductor heterostructures.

In a bulk semiconductor, such dispersion relation leads to an energy continuum with a density of states $\rho(E) \propto \sqrt{E}$ (see the 3D structure in figure 1.1), whereas an energy discretization appears in semiconductor heterostructures when the electron motion is confined at a smaller scale than its De Broglie wavelength:

$$\lambda_B = \frac{2\pi\hbar}{\sqrt{2m_e^*k_B T}}, \quad (1.4)$$

where k_B is the Boltzmann constant and T the temperature of the system. Considering the different quantum confinement directions, three types of semiconductor heterostructures can then be distinguished from the 3D bulk system:

- The quantum well (2D structure in figure 1.1): the electrons are confined in one direction (z) and have a free motion in the other ones (x and y). The dispersion relation of such a system is $E = E_{z,n} + \frac{\hbar^2}{2m_e^*}(k_x^2 + k_y^2)$, where $E_{z,n}$ is the confinement energy related to the size of the trap in the z direction. For a given $E_{z,n}$, the density of states is constant and defined for $E > E_{z,n}$, which thus leads to a "walking stairs" density of final states (one "stair" being linked to one energy $E_{z,n}$).
- The quantum wire (1D structure in figure 1.1): the electrons are confined in two directions (y and z) and have a free motion in the remaining direction (x). The dispersion

relation reads $E = E_{y,m} + E_{z,n} + \frac{\hbar^2 k_x^2}{2m_e^*}$, where $E_{m,n} = E_{y,m} + E_{z,n}$ is the energy confinement. For each energy $E_{m,n}$, the density of states writes as $\rho(E) \propto 1/\sqrt{E - E_{m,n}}$.

- The quantum dot (0D structure in figure 1.1): the electrons are confined in all the three directions of space and does not present anymore a quasi-continuum of states due to any translational invariance. The density of states then presents Dirac functions at each confinement energy $E_{l,m,n} = E_{x,l} + E_{y,m} + E_{z,n}$.

Among all the described heterostructures, this manuscript focuses on the QDs which exhibit a lot of similarities with atomic systems due to the three dimensional confinement of the carriers and the induced discrete density of states.

1.1.2 Fabrication of semiconductor quantum dots

The general idea for confining the carriers in the three dimensions of space is to modify the crystalline potential by fabricating a semiconductor heterostructure with typical sizes smaller than the De Broglie wavelength of the carriers¹. From a practical point of view, it consists in inserting a semiconductor in a larger band gap semiconductor in order to create a potential barrier for the carriers. Two main techniques are used to elaborate semiconductor QDs: the chemical synthesis where colloidal nanocrystals are fabricated in solutions [27], and the epitaxial growth where the nanocrystals are fabricated on a substrate by depositing successive atomic layers of semiconductors.

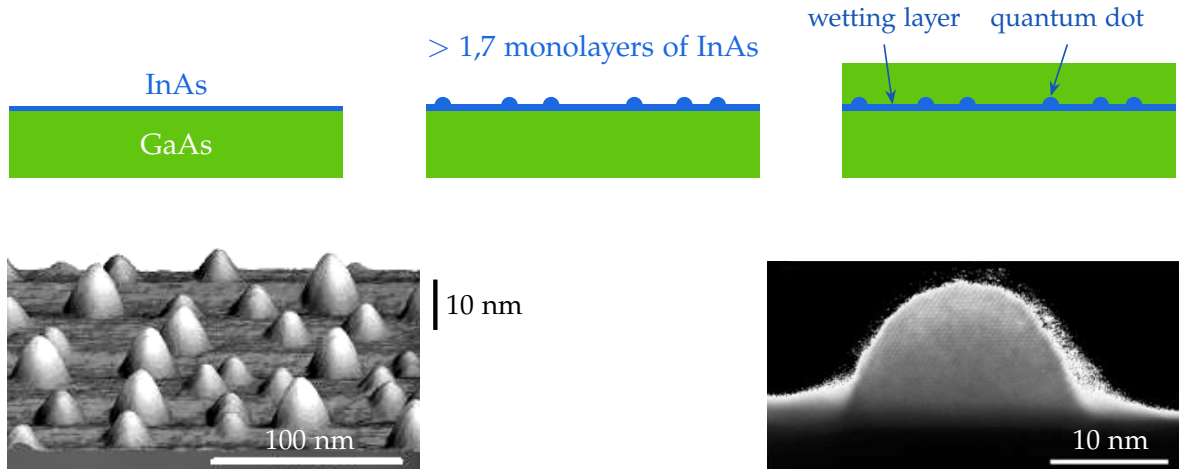


Figure 1.2: Top panels: Fabrication steps in the Stranski-Krastanov epitaxy growth mode. Bottom left panel: AFM image of InAs QDs on a GaAs substrate before the capping step of the epitaxial process (source: Nanostructure Materials & Devices Laboratory of University of Southern California). Bottom right panel: TEM image of a single lens-shaped InAs QD on a GaAs substrate (source: Institute for Microstructural Sciences, NRC, Canada).

The first InAs/GaAs QDs were fabricated in 1985 [28] within this latter technique, in the Stranski-Krastanov growth mode [29]. During this growth process that is schematized in figure 1.2 (top panel), once the thickness of the lower bandgap semiconductor (InAs) has reached 1.7 monolayers [30], the strain accumulated between the two semiconductors due

¹As an example, the De Broglie wavelength in GaAs exceeds 100 nm for temperatures below 50 K.

to the lattice mismatch (the InAs lattice parameter is 7% higher than in GaAs) relaxes by forming self-organized InAs conic islands on top of the GaAs substrate. The remaining 2D InAs layer, the wetting layer, constitutes a quantum well which plays an important role in the QDs optical properties. As shown in figure 1.2 (bottom panels), the conic islands, that are randomly positioned along the surface of the substrate with a typical density of 10^9 - 10^{11} cm^{-2} [31], are typically 20 nm wide and 10 nm high. The capping of the islands by a GaAs layer (\sim ten monolayers) then lead to the final QDs which shapes look like flat lenses with heights of few nanometers. The synthesis of such self-organized strained QDs can be done either by Molecular Beam Epitaxy (MBE), or by Metal Organic Chemical Vapor Deposition (MOCVD)². While the MOCVD ensures a good reproducibility and a faster growth speed, the MBE allows in general a better control of the QDs growth properties (average density and emission wavelength) thanks to possible *in situ* visualization. The InAs/GaAs QDs under study in this manuscript were grown by MBE in the group of Pierre Petroff (University of California Santa Barbara, UCSB).

1.1.3 Electronic states in single quantum dots

In the experimental studies presented in this manuscript, only the interband electronic transitions consisting in the radiative recombination of an electron-hole pair are considered. Therefore, the electronic states of a single QD are deduced from the electronic properties near the Γ point of the InAs and GaAs semiconductors.

The band structures near the gap of these two zinc-blende crystalline structures can be calculated within the k.p perturbation theory either for the non-strained bulk materials [26] or for the strained ones [34]. The electronic states of such crystals present the same symmetry as the atomic orbitals s , p_x , p_y and p_z , where the orbital s is the first conduction band and the three orbitals p are the last valence bands. In semiconductor QDs, the spin-orbit coupling and the strain induced by the lattice mismatch between the InAs wetting layer and the GaAs substrate lift the degeneracy of the valence bands. More particularly, these resulting non-degenerate valence bands exhibit well separated heavy holes and light holes valence bands which allows considering only the electrons conduction band Γ_6 and the heavy holes valence band Γ_8 for the QDs interband transitions. Consequently, by taking into account the spin degeneracy, the eigenstates at stake for the calculation of the confined electronic states in a single InAs/GaAs QD are the two electron states, $|e, \uparrow\rangle = |\frac{1}{2}, +\frac{1}{2}\rangle$ and $|e, \downarrow\rangle = |\frac{1}{2}, -\frac{1}{2}\rangle$, and the two heavy hole states, $|h, \uparrow\rangle = |\frac{3}{2}, +\frac{3}{2}\rangle$ and $|h, \downarrow\rangle = |\frac{3}{2}, -\frac{3}{2}\rangle$, written in the total angular momentum basis $|J, J_z\rangle$.

In the first approximation where a single QD is modeled as a flat lens or a truncated cone of pure InAs embedded in a GaAs matrix, the carriers are in a confinement potential which shows a cylindrical symmetry such that $V(\vec{r}) = V(\rho, z)$, with z the vertical growth axis. Because each InAs island is composed of $\sim 10^4$ atoms, the confinement potential slowly varies at the atomic scale and the electrons wave functions (Eq. (1.2)) can be rewritten in the envelop function approximation [35] as:

$$\psi_{n,\vec{k}}(\vec{r}) = u_{n,\vec{k}}(\vec{r})\varphi_n(\vec{r}) \quad (1.5)$$

²The droplet epitaxy is another growth technique that is used to fabricate non strained QDs, without wetting layer, along crystallographic axes not reachable in the Stranski-Krastanov growth mode [32, 33].

where $\varphi_n(\vec{r})$ is a slowly varying envelop function which verifies the Schrödinger equation:

$$\left(\frac{\hbar^2 \vec{k}^2}{2m_e^*} + V(\rho, z) \right) \varphi_n(\vec{r}) = E_n \varphi_n(\vec{r}) \quad (1.6)$$

In such cylindrical symmetry, the z projection of the angular momentum l_z is a good quantum number and, similarly to the atomic states, the confined electronic states corresponding to $l_z = 0, 1, 2, 3$ are labeled as S, P, D, F . Depending on the potential confinement, the single InAs/GaAs QDs usually show the two confined electronic states S and P : S_e and P_e for the electrons in the Γ_6 conduction band; and S_h and P_h for the heavy holes in the Γ_8 valence band.

In order to give a complete description of the electronic states in realistic QDs, one has to consider the entire system which is composed of QDs on top of a wetting layer, the whole being embedded in a substrate. The carriers can in fact not only populate the confined electronic states of the InAs QDs but also the electronic states of the GaAs barrier (i.e. the bulk states) and the InAs wetting layer (i.e. the quantum well states), characterized by three different types of confinement. The corresponding energy levels and density of states of the entire system are illustrated in figures 1.3 and 1.4, respectively.

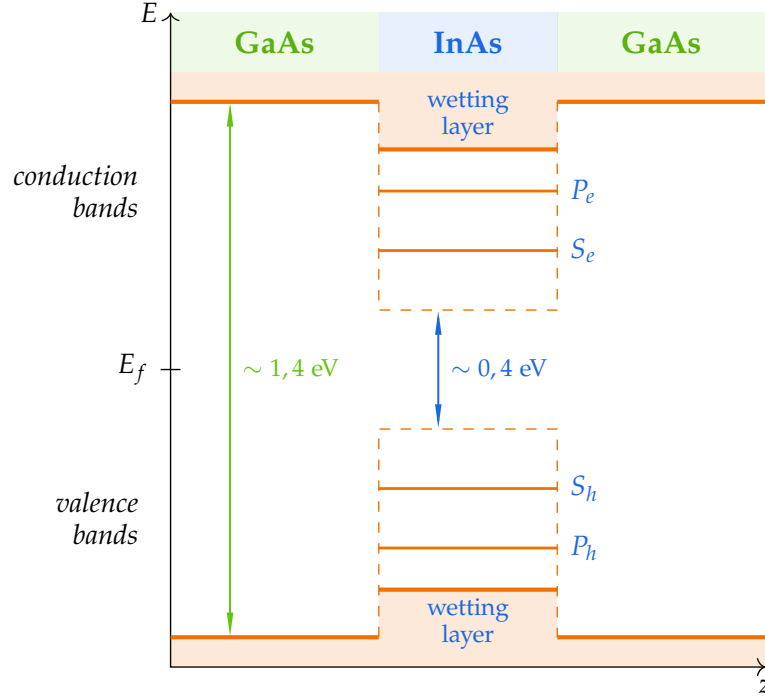


Figure 1.3: Energy states of a single InAs/GaAs QD along the growth axis z . The solid and dashed lines depict the bands of the GaAs and InAs bulk materials, respectively. The confined electronic states S and P in the InAs QD are presented for the valence and conduction bands, along with the continuum of states in the barrier and the wetting layer (orange colored areas). E_f is the Fermi energy. Figure extracted from Ref. [8].

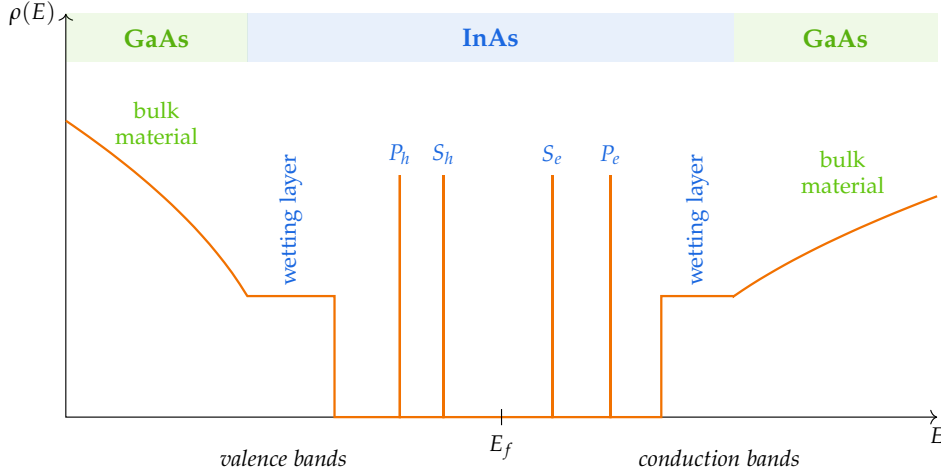


Figure 1.4: Density of the electronic states in a single InAs/GaAs QD showing the 3D continuum and the 2D quasi-continuum of the GaAs barrier and the InAs wetting layer, respectively, as well as the discrete electron and hole states $S_{e,h}$ and $P_{e,h}$ in the InAs QD. E_f is the Fermi energy. Figure extracted from Ref. [8].

1.1.4 Interband optical transitions in single quantum dots

The confined electronic states of a single QD can interact with light. In the envelop function approximation, an optical transition between an initial state $\psi_{i,\vec{k}}(\vec{r}) = u_{i,\vec{k}}(\vec{r})\varphi_i(\vec{r})$ and a final state $\psi_{f,\vec{k}}(\vec{r}) = u_{f,\vec{k}}(\vec{r})\varphi_f(\vec{r})$ is governed by the matrix element $\langle \psi_{i,\vec{k}} | \vec{\epsilon} \cdot \vec{p} | \psi_{f,\vec{k}} \rangle$ in the semi-classical picture of the electric dipole coupling, where $\vec{\epsilon}$ is the polarization of the electric field and \vec{p} the momentum operator. For interband optical transitions, the matrix element is reduced to:

$$\langle \psi_{i,\vec{k}} | \vec{\epsilon} \cdot \vec{p} | \psi_{f,\vec{k}} \rangle = \vec{\epsilon} \cdot \langle u_{i,\vec{k}} | \vec{p} | u_{f,\vec{k}} \rangle \int \varphi_i^*(\vec{r}) \varphi_f(\vec{r}) d^3\vec{r} \quad (1.7)$$

The first term of this interband matrix element leads to the same selection rules as in the bulk material, i.e. only the states $|e \uparrow, h \downarrow\rangle$ and $|e \downarrow, h \uparrow\rangle$ with a total angular momentum ± 1 are coupled to light, contrarily to the states $|e \uparrow, h \uparrow\rangle$ and $|e \downarrow, h \downarrow\rangle$ which have a total angular momentum ± 2 . The second term gives the selection rules between the QD confined states, where only electrons and holes with the same envelop functions symmetry are radiatively coupled. Therefore, the allowed interband optical transitions correspond to the radiative recombination of electron-hole pairs where both electron and hole occupy either a S state or a P state, with opposite spin signs. In the following, for sake of clarity, the spin will not be mentioned and the corresponding optical transitions will be labeled as $1S_h - 1S_e$ (i.e. radiative recombination of one hole in S_h state with one electron in S_e state) and $1P_h - 1P_e$ (i.e. radiative recombination of one hole in P_h state with one electron in P_e state).

When considering the complete QD system, additional optical interband transitions must be considered between the whole set of electron and hole states of the QD, the wetting layer and the barrier. This statement is shown by the theoretical absorption spectrum of a single QD [36] presented in figure 1.5, where crossed interband optical transitions involving one QD state and one wetting layer (WL) state can for example be observed. Signatures of such optical transitions are experimentally observed in the photoluminescence excitation (PLE)

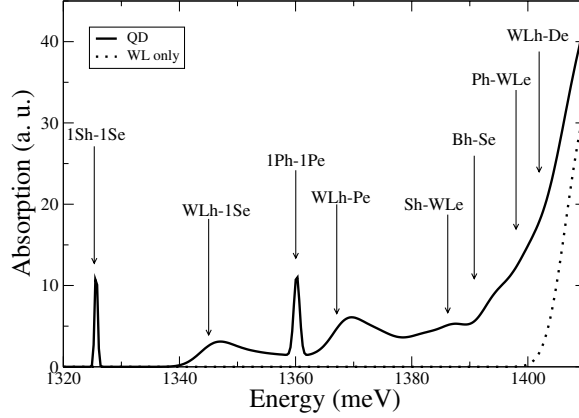


Figure 1.5: Theoretical interband absorption spectra at low temperature of a single QD (solid line) and the sole wetting layer (WL) (dotted line). Figure extracted from Ref. [36].

spectrum of single QDs [1, 37, 38]. In figure 1.5, the first narrow resonance at the lowest energy (1326 meV) corresponds to the transition $1S_h - 1S_e$ and the second narrow resonance at 1360 meV to the transition $1P_h - 1P_e$. Other broader resonances, which correspond to transitions between the S and P confined states of the QD and the WL continuum of states, also appear at 1345 meV and 1370 meV for example. Above 1400 meV, an absorption continuum due to transitions in the wetting layer and in the barrier appear. The energies at stake are typical for InAs/GaAs QDs. In the following, we focus on the only optical transition that is spectrally well isolated from the quasi-continuum of states, i.e. the lowest energy fundamental transition $1S_h - 1S_e$ related to the radiative recombination of one hole in the confined state S_h with one electron in the confined state S_e .

1.1.5 The "pseudo" exciton in single quantum dots

From the general point of view of the bulk material, an electron and a hole that are optically created³ are correlated by the Coulomb interaction and constitute an hydrogen-like system, a 3D exciton, characterized by its Bohr radius a_X^{3D} and a binding energy E_b^{3D} [26]:

$$a_X^{3D} = a_0 \varepsilon_r \frac{m_e}{m} \quad \text{and} \quad E_b^{3D} = -\frac{m}{m_e \varepsilon_r^2} \frac{R_y}{n^2} = -\frac{R_y^*}{n^2} \quad (1.8)$$

where a_0 is the hydrogen Bohr radius, R_y the hydrogen Rydberg energy, m_e the electron mass, m the reduced electron-hole mass and ε_r the relative permittivity of the material. As an example, the Bohr radius and the binding energy of the 3D exciton in GaAs are 115 Å and 4.7 meV, respectively. In a quantum well (here, infinite barriers are considered), the electron-hole pair is still correlated through the Coulomb interaction and the 2D exciton is characterized by the Bohr radius $a_X^{2D} = a_X^{3D}/2$ and a binding energy $E_b^{2D} = 4E_b^{3D}$ (for the exciton $1S$, $n = 1$). For both the 2D and 3D excitons, the binding energy is much smaller than the gap energy ($E_g = 1.427$ eV in GaAs) and the Coulomb interaction acts only as a correction of the exciton energy. Moreover, due to the delocalization of the 3D exciton in the bulk material and of the 2D exciton in the confinement plane of the quantum well, a macroscopic number of excitons can coexist in such systems.

³We focus here on an optical excitation but the injection of an electron-hole pair can also be done by a thermal or an electrical excitation.

In self-assembled QDs, an electron-hole pair mainly results from the strong localization of the carriers which is induced by the strong tridimensional confinement. The energy correction to the binding energy of the electron-hole pair is thus dominated by the confinement energy which is equal to a few hundreds of meVs, while the correction energy due to the Coulomb interaction is only a few meVs (this observation can also be made by comparing the Bohr radius of a 3D or a 2D exciton with the typical QD dimensions of a few nanometers). Moreover, due to the discretization of the density of states and the Pauli principle, only two excitons can coexist in a QD. Nevertheless, even though there are fundamental differences with the 3D and 2D excitons, an electron-hole pair in a QD is commonly considered as a "pseudo" 0D exciton, and we will use the exciton denomination in the following of this manuscript.

As mentioned above, two excitons at most can coexist in the same QD, but different types of excitonic complexes can also populate a QD. First, the neutral exciton X which consists in one electron-hole pair and is four times degenerated when considering the carriers spins. As stated in section 1.1.4, since only electron-hole pairs with opposite spin signs lead to bright states, one can differentiate two bright excitons and two dark excitons. The radiative recombination of a bright exciton, which state is defined as $|1S_h - 1S_e\rangle$, leads to the final QD empty state, $|\text{vac}\rangle$, with $|1S_h - 1S_e\rangle \rightarrow |\text{vac}\rangle$ the corresponding fundamental excitonic transition. Then, the charged excitons which consist in the trions X^\pm formed by an exciton and a supplementary charge (a hole for X^+ and an electron for X^-). Each trion is twice degenerated and one charge remains in the QD after their radiative recombination, the corresponding transitions being $|2S_h - 1S_e\rangle \rightarrow |1S_h - 0S_e\rangle$ for X^+ and $|1S_h - 2S_e\rangle \rightarrow |0S_h - 1S_e\rangle$ for X^- . Finally, the biexciton which is composed of two bright excitons in the QD. The biexciton radiative recombination exhibits the so-called biexciton-exciton cascade where a photon is emitted at the exciton energy after the emission of a photon at the biexciton energy [39], the corresponding transition being $|2S_h - 2S_e\rangle \rightarrow |1S_h - 1S_e\rangle \rightarrow |\text{vac}\rangle$.

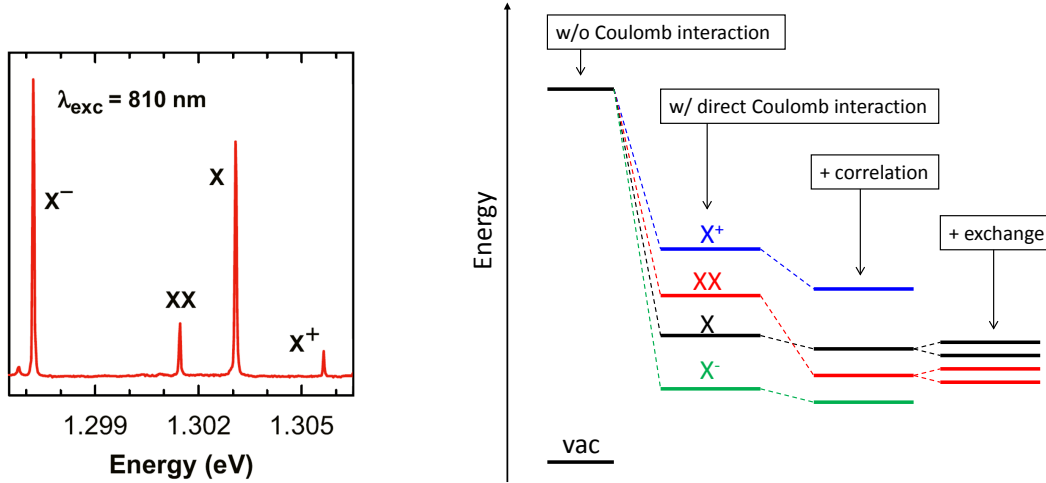


Figure 1.6: Left panel: Photoluminescence spectrum at $T = 4$ K of a non-resonantly excited single QD showing the various excitonic complexes (figure extracted from Ref. [40]). Right panel: Energy diagram of the excitonic complexes in a single QD (the QD empty state $|\text{vac}\rangle$ is also indicated).

As can be observed in the photoluminescence (PL) spectrum of a single QD presented in figure 1.6 (left panel), the radiative recombination of different excitonic complexes lead to photons of different energies. In fact, as schematized in figure 1.6 (right panel), the corresponding emission energies of the exciton, the trions and the biexciton depend on the respective

binding energies which vary from one excitonic complex to another because of two main contributions [41]: the direct attractive and repulsive Coulomb interactions between the carriers constituting the excitonic complexes of the order of 10 meV, and the correlation correction due to the fermionic nature of the carriers of the order of a few meVs. This latter effect explains the usual experimental observation of a lower biexciton emission energy than the exciton one. Finally, a last minor contribution of the order of a hundred of μeV due to the exchange interaction between the spins of the carriers in non symmetrical QDs is responsible for the fine structure of the bright excitons (i.e. the degeneracy lift of the two bright excitons).

1.2 The artificial atom model and its limits

1.2.1 The population relaxation mechanisms

Most of the spectroscopic experiments in single QDs are performed under non-resonant excitation. In such a configuration which is schematized in figure 1.7, the non-resonant laser creates carriers in the barrier or in the wetting layer. The photo-created carriers then relax to the QD excited states via capture of the carriers from the barriers or the wetting layer to the confined QD excited states such as the P states. Then, intra-dot relaxation processes between the different QD discrete states (for example $P_h \rightarrow S_h$ and $P_e \rightarrow S_e$) lead to electron and hole population of the ground states from which the QD PL occurs (at the neutral exciton energy in this example).

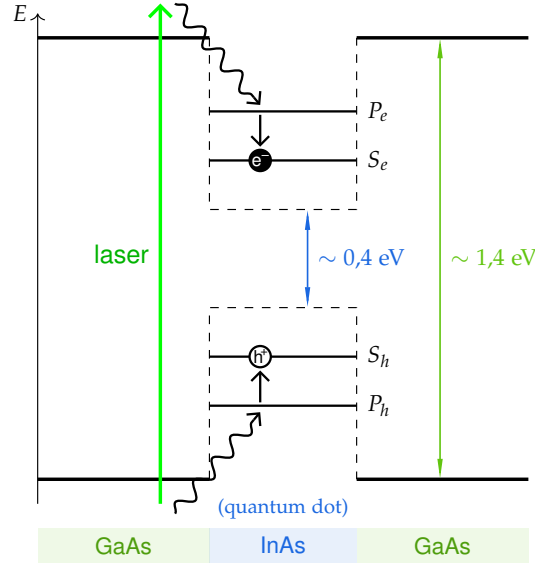


Figure 1.7: Illustration of the population relaxation process when a single QD is non-resonantly excited by a laser in the barriers. Two consecutive relaxation mechanisms are then involved: the capture of one electron and one hole from the barriers to the QD P states (twisted arrows), followed by the intra-dot relaxations between the QD discrete states, $P_h \rightarrow S_h$ and $P_e \rightarrow S_e$, (straight arrows).

Theoretical works show that the capture mechanism relies either on emission of optical phonons [42, 43] with typical capture times between 100 fs and 100 ns, or on electron-electron and electron-hole Auger scattering [44, 45] with typical capture times between 1 ps and 1 μs . These calculations are in perfect agreement with time-resolved experiments performed in QDs ensemble [46] and in single QDs [47] where capture times of the order of 100 ps have been

measured. On the other hand, irreversible Auger scattering is mainly responsible for the intra-dot relaxation process, and theoretical calculations [42, 48] give estimate of the corresponding relaxation times in the 100 fs - 10 ps range. In fact, differential transmission measurements [49], pump-probe spectroscopy [50] and time-resolved experiments [51, 52] showed that the Auger-assisted processes involved in the intra-dot carriers relaxation occur within characteristic times between 1 ps and 10 ps. In total, theoretical and experimental results show that the intra-dot relaxation times are generally much shorter (from 100 fs to 10 ps) than the characteristic times of the carriers' capture from the continuum (up to 1 μ s). The relaxation times to the QD ground states are thus often only attributed to the capture time. Nevertheless, intra-dot relaxation processes, although secondary in the population relaxation, play a very important role in the coherence relaxation [53]. This statement will be discussed in more details in section 1.2.4.

1.2.2 The picture of the two-level system

In the analogy of the artificial atom picture, a QD is commonly described as a TLS when studying the fundamental excitonic transition $|1S_h - 1S_e\rangle \rightarrow |\text{vac}\rangle$ since it is the only optical transition that is spectrally well isolated from the quasi-continuum of states (see figure 1.5). In this context, as shown in figure 1.8, the empty QD state $|\text{vac}\rangle$ corresponds to the TLS ground state $|g\rangle$, whereas the configuration where an exciton populate the QD (i.e. the $|1S_h - 1S_e\rangle$ state) characterizes the TLS excited state $|e\rangle$. The energy difference between these two states is then defined as $\hbar\omega_0 = \hbar\omega_e - \hbar\omega_g = E_X$, where $\hbar\omega_g$ and $\hbar\omega_e$ are the energies of the ground and excited states, respectively, and E_X the exciton energy.

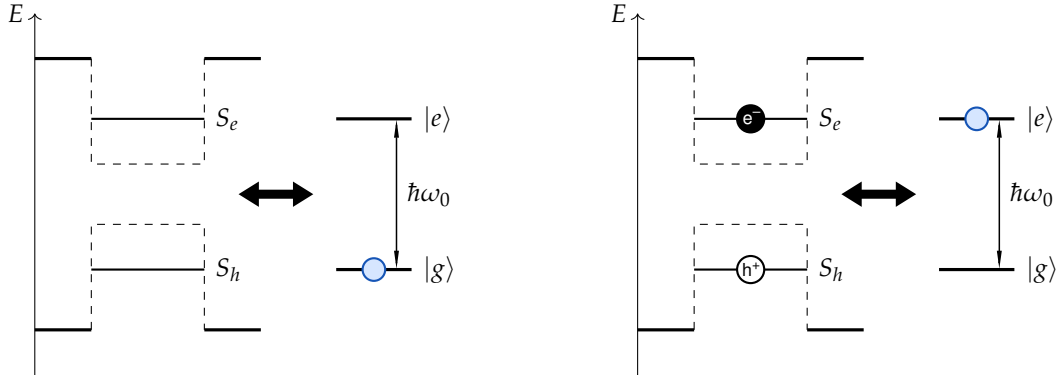


Figure 1.8: The QD two-level system in the ground state (left) and in the excited state (right).

The optical properties of such TLS is described in the density matrix formalism by [54]:

$$\rho = \begin{pmatrix} \rho_{ee} & \rho_{eg} \\ \rho_{ge} & \rho_{gg} \end{pmatrix} \quad (1.9)$$

where the diagonal elements ρ_{gg} and $\rho_{ee} = 1 - \rho_{gg}$ describe the population of the ground and excited states, respectively, and the non-diagonal elements ρ_{ge} and $\rho_{eg} = \rho_{ge}^*$ describe the coherence of the TLS which is directly related to the electric dipole of the transition. In the realistic situation where the optically excited TLS is in interaction with its environment, its evolution is described by the equation:

$$i\hbar \frac{d\rho}{dt} = [H, \rho] + \mathcal{L}(\rho) \quad (1.10)$$

where $H = H_0 + V$ is the hamiltonian of the TLS in interaction with the electromagnetic field via the dipolar interaction hamiltonian V , and \mathcal{L} is an operator describing the relaxation processes. In particular, the relaxation processes are taken into account by phenomenologically introducing two time constants: the population relaxation time T_1 which is most commonly defined as the population lifetime of the excited state; and the relaxation time of the coherence, or the decoherence time, T_2 . The relaxation processes are then described in equation (1.10) by a term written as:

$$\frac{\partial \rho}{\partial t} = \begin{pmatrix} -\frac{\rho_{ee}}{T_1} & -\frac{\rho_{eg}}{T_2} \\ -\frac{\rho_{ge}}{T_2} & -\frac{\rho_{gg}}{T_1} \end{pmatrix} \quad (1.11)$$

This means that, after the optical excitation, the TLS relaxes from its excited state $|e\rangle$ to its ground state $|g\rangle$ by spontaneous emission (i.e. the exciton radiative recombination) after the time T_1 , and the coherence between the two states is lost due to the spontaneous emission process and the interaction with their environment after the time T_2 .

When the spontaneous emission is the only relaxation process which limits the coherence of the TLS, the decoherence time is given by $T_2 = 2T_1$ which is defined as the radiative limit of the TLS [54]. The relation between the two relaxation times shows in fact that the relaxation of the population inevitably induces the relaxation of the electric dipole of the transition⁴. In this case, the homogeneous linewidth of the transition corresponds to the natural linewidth and is directly linked to the spontaneous emission rate. The radiative limit is a good approximation for the case of diluted atomic gases where the interactions between the atoms are negligible. However, a semiconductor QD cannot be considered as an isolated system due to its solid state nature. A single QD is grown on top of a 2D semiconductor layer and capped by a 3D semiconductor, which inevitably present structural defects that play a role in the QD relaxation. Therefore, the coherence of this artificial atom is not only limited by the spontaneous emission process but also by the coupling with the phonons in the solid matrix and the charges that are trapped in the surrounding defects (see the details in the next section). This leads to additional relaxation processes that are responsible for the relaxation of the coherence of the QD TLS within a time constant T_2^* , which is defined as the pure dephasing time since only the phase of the excited state is affected and not the TLS population. In conclusion, the decoherence time of the QD in the TLS picture is given by the more general relation:

$$\frac{1}{T_2} = \frac{1}{2T_1} + \frac{1}{T_2^*} \quad (1.12)$$

1.2.3 The implications of the artificial atom model

From the fundamental point of view, an important implication of the artificial atom model where the exciton can be considered as a TLS is the development of quantum optics experiments in solid state physics. Such experiments that were first restricted to atomic systems have in fact exhibited phenomenons in single QDs which are intrinsically related to the TLS structure. First, the emission of photons with a sub-poissonian statistics is one of the main fundamental phenomenons that can be cited. This effect relies on the Pauli exclusion principle and the Coulomb interaction between the QD carriers which induce different radiative recombination energies and spectrally isolated emission lines. The emission of antibunched photons and the associated photon antibunching dip, which were first demonstrated by P.

⁴The factor 2 reflects that the coherence is proportional to the electric field whereas the populations are proportional to the intensity of the electric field.

Michler et al. [13], is now at the heart of the realization of integrated single photon sources that could be used for applications [55] such as quantum cryptography [56]. In such context, the pure dephasing processes that reduce the coherence of the emitted photons must be inhibited in order to get indistinguishable photons [16] and develop efficient QD-based devices for quantum information processing [57]. Beyond the generation of single photons, the fine structure of the excitonic TLS can also be exploited to generate polarized entangled states, similarly to the Bell's states in atomic physics [58], for quantum cryptography applications. This effect relies on the radiative cascade biexciton-exciton-vacuum which, within the configuration where the spin relaxation is inhibited and the two bright excitons are degenerated, results in entangled orthogonally polarized photons [59–61]. Then, another fundamental phenomenon that can be observed when a single QD is strongly driven by a laser either under quasi-resonant excitation [62] or resonant excitation [6, 63, 64] is the Rabi oscillations. This effect, which is characterized by the sinusoidal temporal evolution of the populations of the TLS ground and excited states with a pulsation imposed by the strength of the coupling, is used to coherently control the quantum bit formed by the excitonic TLS or the corresponding spin states [65].

Last but not least, the coupling between the excitonic TLS and an optical cavity mode paves the way to the Cavity Quantum Electrodynamics (CQED) research field in solid state systems, similarly to single atoms in cavity [66]. In the weak coupling regime, the Purcell effect phenomenon [67], which corresponds to the acceleration of the TLS spontaneous emission rate, has first been observed for single QDs in micropillars [68] and then in photonic crystal microcavities [69]. This effect, which also induces the redirection of the emitted photons in the cavity mode, is notably used to increase the single photon sources efficiency [70]. In the strong coupling regime, the degeneracy lift between the resonant exciton and cavity modes leads to new light-matter states that are energetically separated by the Rabi splitting. This phenomenon, which was first observed in atoms [71], has been observed for QDs in photonic crystal microcavities [72, 73] and microdisks [74]. As a consequence, another approach to coherently control the exciton quantum bit in a single QD and generate non-classical states of light is to benefit from the strong coupling of a QD TLS with an optical microcavity and from the resulting quantum anharmonicity of the energy structure of the QD-cavity system [75]. The non-linear photon blockade phenomenon, where the absorption of a photon at the exciton-photon polariton energy blocks the absorption of a consecutive photon, is one of the possibilities to generate quantum logic gates for quantum computation applications [76]. This effect has first been investigated in atoms [77] and then in single QDs embedded in photonic crystal microcavities [21, 78, 79].

1.2.4 The limits of the artificial atom model

As introduced in section 1.2.2, a non-resonantly excited QD presents inevitably a decoherence time T_2 that is shorter than the one imposed by the radiative limit because of the interaction of the QD carriers with the solid environment. In particular, the relaxation processes that are characterized by the pure dephasing time T_2^* are the coupling with the phonons and the charges that are inherent to the solid matrix in which the QD is grown.

The coupling with the acoustic phonons is the first relaxation process which leads to a drastic linewidth broadening of the fundamental excitonic transition when increasing the temperature. In particular, the radiative recombination assisted by the emission/absorption of acoustic phonons results in a non-lorentzian emission line characterized by a pedestal covering

typically a 5 meV spectral range [80–82]. This effect is clearly illustrated in figure 1.9 (left panel) which presents the temperature dependance of the emission linewidth of a single QD exciton. Below 50 K, the emission of acoustic phonons during the exciton recombination process leads to asymmetric sidebands which, due to the absorption of acoustic phonons above 50 K, tend to get symmetric and dominate the emission spectrum, the latter retrieving a broad lorentzian profile at 80 K. All these processes are well interpreted within the Huang-Rhys framework of the electron-phonon interaction developed in the case of localized electrons [83]. In this theory, a linear coupling between the fundamental excitonic state and a reservoir of acoustic phonons is taken into account via a deformation potential of the crystal, resulting in a system of independent bosons. The fundamental state then corresponds to a non-entangled state between the exciton and the n acoustic phonons of the reservoir. At low temperature ($T \leq 10$ K), because the phonon reservoir is hardly populated, the coupling with the acoustic phonons is negligible and the spectrum is dominated by a central Zero-Phonon-Line (ZPL) which linewidth should be equal to the natural linewidth regardless of the temperature. However, as shown in figure 1.9 (right panel), this statement is not verified experimentally and a thermoactivated broadening of the ZPL is observed instead. This highlights the existence of additional dephasing processes in single QDs.

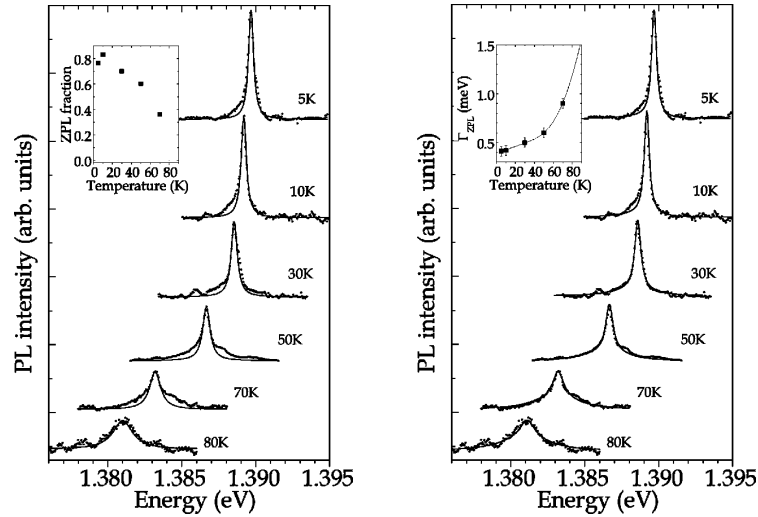


Figure 1.9: Left panel: Photoluminescence spectra of a single QD exciton as a function of the temperature, along with the respective lorentzian fits (solid line); Inset: temperature dependance of the Zero-Phonon-Line (ZPL) fraction of the total integrated intensity. Right panel: Same photoluminescence spectra fitted by calculated spectra, consisting in the convolution of the emission profile given by the Huang-Rhys theory with a lorentzian line; Inset: temperature dependance of the ZPL linewidth (extracted from the lorentzian fits) showing a thermoactivated broadening. Figures extracted from Ref. [82].

The coupling with the optical phonons, which not only contributes to the intra-dot population relaxation process between the QD discrete states [84, 85] but also plays an important role in the QD decoherence, must be considered. The strong coupling between the optical phonons and the QD discrete excitonic states which leads to polaron states (i.e. mixed exciton-phonon states) [86, 87] is a direct coupling which induces a linewidth broadening of the QD exciton [53]. More precisely, due to the interaction with the phonons reservoir, the phonon part of the polarons is very unstable and the phonon-phonon interaction results in

the disintegration of the LO optical phonon into one LO optical phonon and one LA acoustic phonon [88]. This opens a relaxation channel for the high energy polarons states to the lowest energy polaron state which is none other than the zero phonon excitonic state $|e\rangle$. This process results in the broadening of the excitonic transition which follows the temperature dependence:

$$\Delta\Gamma_{\text{LO}}(T) = b \exp\left(-\frac{\Delta E}{k_B T}\right) \quad (1.13)$$

with ΔE the activation energy (~ 25 meV [53, 87]).

Another important relaxation process is the coupling with the fluctuating electrostatic environment in the vicinity of the QD, which is responsible for the spectral diffusion phenomenon. The residual charges, that undergo a series of trapping/detrapping in/from the wetting layer defects and the barriers impurities, constitute in fact a fluctuating electrostatic reservoir which influences the QD emission energy by quantum confined Stark effect. Several experimental studies showed the corresponding temporal fluctuations of the excitonic emission energy in epitaxial QDs, either in the regime of slow fluctuations compared to T_1 [89, 90] or in the regime of fast fluctuations [91, 92], where two distinct emission lines or a broadened emission line is observed, respectively. In particular, the work of A. Berthelot [3] showed that the trapping of a carrier in a defect is similar to the capture of a carrier in a QD by emission of optical phonons and Auger scattering effects (see section 1.2.1). However, the detrapping process is dominated by the absorption of acoustic phonons and Auger effects, and two regimes can then be distinguished [91, 92]. On the one hand, the regime of slow fluctuations ($\Sigma\tau_c \gg \hbar$, Σ being the fluctuations amplitude and τ_c the time constant of the trapping/detrapping process) at high excitation power ($P > 0.5$ kW/cm²) and high temperature ($T > 35$ K), where the excitonic line has a gaussian profile which broadens when the amplitude of the fluctuations increases. On the other hand, the regime of fast fluctuations ($\Sigma\tau_c \ll \hbar$) at low power ($P < 0.5$ kW/cm²) and low temperature ($T < 35$ K), where the excitonic line shows a lorentzian profile which broadens by increasing the temperature according to the following relation:

$$\Delta\Gamma_{\text{fluct}}(T) = a T \quad (1.14)$$

where a is a coefficient related to the trapping/detrapping process by emission/absorption of acoustic phonons (few $\mu\text{eV/K}$). Therefore, the coupling to the acoustic phonons reservoir and its related decoherence effect appears indirectly through the coupling to the fluctuating electrostatic environment.

To summarize, in the usual regime of low temperature and low power excitation, the exciton linewidth follows the general temperature dependence:

$$\Gamma(T) = \Gamma_0 + \Delta\Gamma_{\text{fluct}}(T) + \Delta\Gamma_{\text{LO}}(T) = \Gamma_0 + a T + b \exp\left(-\frac{\Delta E}{k_B T}\right) \quad (1.15)$$

where Γ_0 is the linewidth at 0 K (few μeV). It is thus essential to decrease the temperature and the excitation power in order to minimize the decoherence processes in a single QD and to eventually reach the radiative limit. However, even if a clear linewidth narrowing is observed at low temperature and low excitation power (linewidths of about 5 μeV), the spectral diffusion induced by the coupling to the electrostatic environment that is created by a non-resonant excitation still remains. In this context, a standard micro-PL experiments performed on single QDs under non-resonant excitation limits intrinsically the picture of the artificial atom since the carriers that are photogenerated in the wetting layer or in the barriers can be trapped in

the defects in the vicinity of the QDs and constitute a dephasing reservoir. Moreover, such excitation often leads to the coexistence of several excitonic complexes, as shown in figure 1.6. Therefore, a system composed of eight levels rather than two levels should be rigorously considered in order to describe all the involved transitions of type $|S\rangle \rightarrow |\text{vac}\rangle$ in a single QD.

Regarding the potential applications of QD-based single photon sources, and more specifically for the use of linear optics for quantum information processing [57], the radiative limit must be reached in order to manipulate photons with the longest reachable coherence time and therefore to increase the reliability of such process as well as the number of the possible operations.

1.3 The resonant excitation: a way to overcome these limits?

1.3.1 From a quasi-resonant to a resonant excitation

Regarding the dephasing processes which limit the picture of the artificial atom at low temperature, one main objective is thus to get rid of the fluctuating electrostatic environment which induces spectral diffusion. In this context, an experimental study of the exciton linewidth as a function of the laser detuning with respect to the exciton energy showed that the excitation energy is in fact another important parameter that can act on the dephasing processes. As shown in figure 1.10, the excitonic linewidth decreases when the excitation energy gets closer to the exciton energy and in particular, a strong linewidth narrowing of more than 30% is observed for a quasi-resonant excitation consisting in the resonant excitation of the QD excited P states (i.e. for the creation of the electron-hole pairs directly in the P states of the QD at a detuning of ~ 20 meV). Consequently, these results suggest that a strictly resonant excitation of the neutral exciton should lead to the radiative limit configuration where the exciton could be considered as a genuine TLS with a linewidth Γ imposed by the population relaxation process only, i.e. $\hbar\Gamma = \frac{\hbar}{T_1} = \frac{2\hbar}{T_2}$.

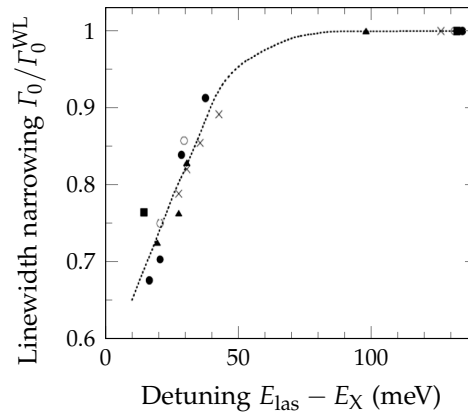


Figure 1.10: Narrowing of the homogeneous linewidth of the exciton line as a function of the detuning between the laser excitation energy E_{las} and the exciton energy E_X , for different QDs (each symbol corresponds to one QD). Γ_0 is the extrapolated linewidth of the exciton at 0 K when excited at the energy E_{las} , and Γ_0^{WL} is the extrapolated linewidth of the exciton at 0 K when excited at the wetting layer (WL) energy. Figure extracted from Ref. [53].

The scenario of the resonant excitation of the fundamental QD state is simpler than the non-resonant excitation configuration since it does not involve anymore the complex phonon

and Auger relaxation mechanisms presented in section 1.2.1. However, from the experimental point of view, it appears as a real challenge because the scattering of the resonant laser completely hides the signal from the QD in a conventional confocal PL experiment. Another experimental configuration has thus to be considered and, for example, an orthogonal excitation-detection allows exciting resonantly a single QD⁵. In that case, one of the bright excitons can be resonantly excited by directly creating the carriers in the corresponding QD S states with an excitation laser with a smaller linewidth than the exciton fine structure splitting. Then, as the spin flip relaxation processes are very slow compared to the exciton lifetime at low temperature (a ms versus a ns) [93,94], only the two states $|g\rangle$ and $|e\rangle$ of the TLS picture can be considered in the whole absorption/emission process. In principle, this should allow us to consider the QD as an ideal TLS characterized by its natural linewidth Γ .

1.3.2 The two-level system under resonant excitation

The ideal TLS is considered here in the second quantification where the electromagnetic field is quantified⁶. The excitation laser, which excites the excitonic transition at the energy $E_L = \hbar\omega_L = \hbar\omega_0 = E_X$ with a much narrower spectral linewidth than Γ , is modeled by a Dirac function. The Hamiltonian of the TLS in interaction with such resonant electromagnetic field is then given in the dipolar approximation by [96]:

$$H = \frac{1}{2}\hbar\omega_0\sigma_z + \hbar\omega_L a^\dagger a + \hbar g(\sigma_+ a + \sigma_- a^\dagger) \quad (1.16)$$

where a and a^\dagger are the photon creation and annihilation operators, g is the dipolar coupling factor, and the operators $\sigma_z = |e\rangle\langle e| - |g\rangle\langle g|$, $\sigma_- = |g\rangle\langle e|$ and $\sigma_+ = |e\rangle\langle g|$ describe the TLS within the spin algebra ($[\sigma_-, \sigma_+] = -\sigma_z$ and $[\sigma_-, \sigma_z] = 2\sigma_-$). In the rotating wave approximation, the TLS is then described by the "spin operator" S where:

$$S_z = \sigma_z \quad \text{and} \quad S_\pm(t) = \sigma_\pm e^{\mp i\omega_L t} \quad (1.17)$$

The operator S_z is related to the population of the TLS and the operators S_\pm to its electric dipole moment μ written as:

$$\mu = \mu_- + \mu_+ = g\sqrt{\frac{2\hbar\epsilon_0 V}{\omega_L}}\sigma_- + g^*\sqrt{\frac{2\hbar\epsilon_0 V}{\omega_L}}\sigma_+ \quad (1.18)$$

with V the mode volume of the electromagnetic field of the laser.

When considering the emission of a resonantly-driven TLS, by analogy with the classical theory of electromagnetism, the electric field of the light detected at a position r and a time t , $E(r, t) = E^{(+)}(r, t) + E^{(-)}(r, t)$ ($E^{(+)}(r, t)$ and $E^{(-)}(r, t)$ are the electric field operators of positive and negative frequency, respectively), is proportional to the dipole radiation at a time $t - \frac{r}{c}$ such as:

$$E^{(\pm)}(r, t) \propto \mu_\mp \left(t - \frac{r}{c}\right) \quad (1.19)$$

⁵The corresponding experimental setup that was developed at LPA to measure the resonance fluorescence of a single QD is described in chapter 2. In this chapter, we focus on the emission properties of a resonantly excited TLS, assuming that it is experimentally feasible.

⁶The complete theory of the resonance fluorescence of a TLS can be found for example in [54, 95, 96].

Moreover, the detected intensity is given by $\langle I \rangle \propto \langle E^{(-)}(r, t) E^{(+)}(r, t) \rangle$ which, in the case of a realistic detector characterized by a much longer time integration than the lifetime of the TLS, can be written in the stationary regime as:

$$\langle I \rangle^{(\text{st})} \propto \langle S_+(t) S_-(t) \rangle^{(\text{st})} = \frac{1 + \langle S_z \rangle^{(\text{st})}}{2} \quad (1.20)$$

We stress that this intensity corresponds to the integrated intensity over the whole emission spectral range. It depends on the laser detuning with respect to the excitonic transition, $\Delta = E_{\text{las}} - E_X = \hbar\omega_L - \hbar\omega_0$, and is related to the spectral density of the intensity:

$$I(\Delta) = \int \mathcal{I}(\Delta, \omega) d\omega \quad (1.21)$$

In the formalism of the matrix density in the rotating frame approximation, the evolution of the TLS is governed by the optical Bloch equations [54]:

$$\begin{aligned} \frac{d\langle S_z \rangle}{dt} &= i\Omega (\langle S_- \rangle - \langle S_+ \rangle) - \Gamma (\langle S_z \rangle + 1) \\ \frac{d\langle S_{\pm} \rangle}{dt} &= - \left(\pm i\Delta + \frac{\Gamma}{2} \right) \langle S_{\pm} \rangle \mp i\frac{\Omega}{2} \langle S_z \rangle \end{aligned} \quad (1.22)$$

where $\langle S_+ \rangle = \tilde{\rho}_{ge}$, $\langle S_- \rangle = \tilde{\rho}_{eg}$ and $\langle S_z \rangle = \tilde{\rho}_{ee} - \tilde{\rho}_{gg}$ (with $\tilde{\rho}_{gg} + \tilde{\rho}_{ee} = 1$), and $\Omega = \frac{|\mu||\mathcal{E}|}{\hbar} = 2g\sqrt{\langle n \rangle}$ is the Rabi pulsation characterizing the strength of the light-matter coupling (Ω^2 is proportional to the excitation power through the field intensity \mathcal{E}^2 or the average photon number $\langle n \rangle$). The intensity of the emission of the ideal resonantly-driven TLS is then deduced from the solutions of the equations (1.22) in the stationary regime and is given by:

$$\langle I \rangle^{(\text{st})} \propto \frac{\Omega^2}{\Gamma^2 + 2\Omega^2 + 4\Delta^2} \quad (1.23)$$

This expression can also be expressed as a function of the relaxation times of the TLS:

$$\langle I \rangle^{(\text{st})} \propto \frac{1}{2} \cdot \frac{\Omega^2 T_1 T_2}{1 + \Omega^2 T_1 T_2 + \Delta^2 T_2^2} = \frac{1}{2} \cdot \frac{s}{1 + s} \quad (1.24)$$

where the saturation parameter s is defined as:

$$s = \frac{\Omega^2 T_1 T_2}{1 + \Delta^2 T_2^2} = \frac{P}{P_0} \quad (1.25)$$

The saturation parameter is directly related to the excitation power P and the TLS saturation power P_0 , above which the TLS cannot emit more than one photon every $2T_1$. More specifically, for excitation powers well above this saturation power, the ground and excited states of the system tend to be equally populated with a constant population occupation number of $1/2$. We stress that the saturation parameter delimitates two different important excitation regimes, defined by $s \ll 1$ and $s \gg 1$, that will be discussed in the next section 1.3.3.

The total intensity of the TLS emission, given by equation (1.24), is presented as a function of the laser detuning in figure 1.11 for different values of the saturation parameter at zero detuning, $s(\Delta = 0) = s_0 = \Omega^2 T_1 T_2$. The corresponding intensity spectrum $I(\Delta)$ is characterized by a Lorentzian line which reflects the typical behavior of the emission of a TLS under

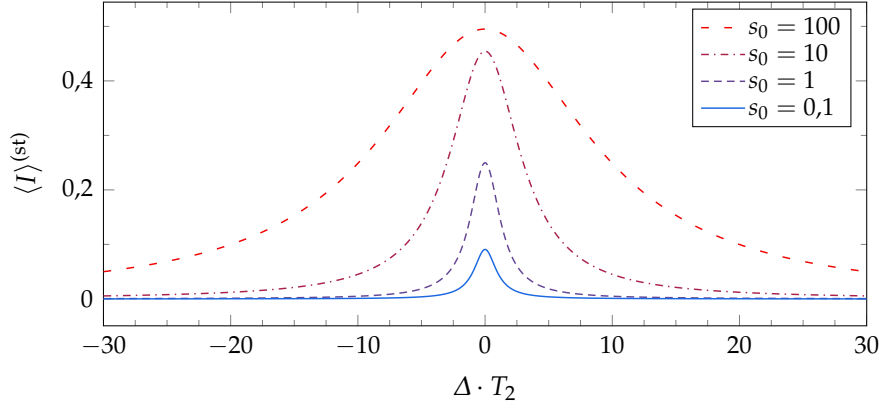


Figure 1.11: Total intensity emitted by a two-level system as a function of the laser detuning with respect to the transition, for different values of the saturation parameter s_0 . The detuning is displayed by the dimensionless quantity $\Delta \cdot T_2$. Figure extracted from Ref. [8].

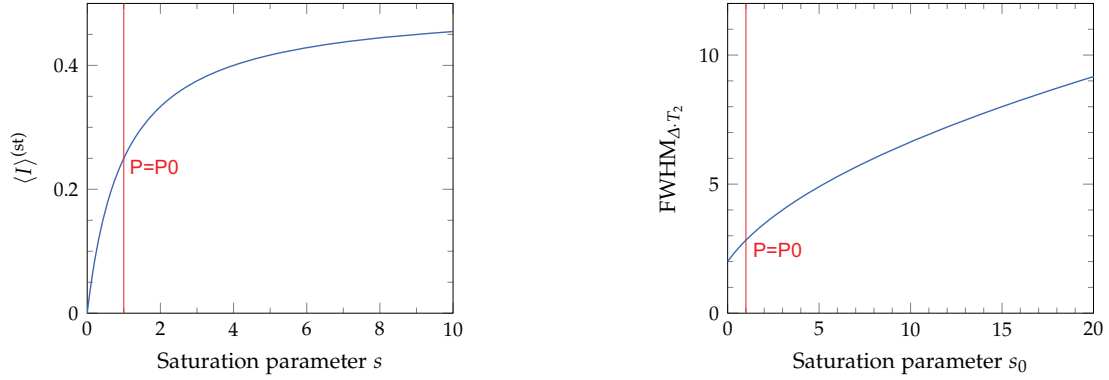


Figure 1.12: Maximum intensity $\langle I \rangle^{(st)}$ ($\Delta = 0$) (left panel) and linewidth $\text{FWHM}_{\Delta \cdot T_2}$ (right panel) of the intensity spectrum $I(\Delta)$ presented in figure 1.11 as a function of the saturation parameter s_0 . Figure extracted from Ref. [8].

resonant excitation, where the saturation of the intensity and the broadening of the spectrum is induced by the population saturation of the transition when $s_0 \gg 1$. This effect is more visible in the power dependence of the maximum intensity and of the associated linewidth presented in figure 1.12. In particular, the linewidth broadening of the emission line follows the relation:

$$\text{FWHM}_{\Delta \cdot T_2} = 2\sqrt{1 + s_0} \quad (1.26)$$

where $\text{FWHM}_{\Delta \cdot T_2}$ stands for the Full Width Half Maximum expressed in the dimensionless quantity $\Delta \cdot T_2$. On this theoretical example, for the particular case where $s_0 \rightarrow 0$, $\text{FWHM}_{\Delta \cdot T_2}(s_0 \rightarrow 0) = 2$, which corresponds to an energy linewidth of $2\hbar/T_2$. Therefore, from the experimental point of view, the linewidth of the intensity spectrum $I(\Delta)$ measured at low excitation power gives a direct estimation of the decoherence time T_2 of the TLS.

1.3.3 The specificity of the resonance fluorescence of a two-level system

In order to fully characterize the properties of the light emitted by a TLS, it is crucial to take into account in the previous theoretical study the contribution of the vacuum fluctuations

of the electromagnetic field since it influences the TLS quantum state. These random fluctuations, that are characterized by short correlation times compared to the TLS lifetime, leads in fact to the relaxation of the average electric dipole moment (i.e. $\langle S_{\pm}(t) \rangle$) and the fluctuation of the instantaneous dipole moment (i.e. $\delta S_{\pm}(t)$) around its average value. In other word, the emission of a TLS is composed of the radiation induced by the average motion of the electric dipole, and the radiation induced by the fluctuations of this average motion. In this context, the dipolar operators previously introduced can be written as:

$$S_{\pm}(t) = \langle S_{\pm}(t) \rangle + \delta S_{\pm}(t) \quad \text{with} \quad \langle \delta S_{\pm}(t) \rangle = 0 \quad (1.27)$$

Consequently, the intensity of the emission of a TLS is given by:

$$\langle I \rangle^{(\text{st})} \propto \underbrace{\langle S_+ \rangle^{(\text{st})} \langle S_- \rangle^{(\text{st})}}_{\langle I_{\text{el}} \rangle} + \underbrace{\langle \delta S_+ \delta S_- \rangle^{(\text{st})}}_{\langle I_{\text{inel}} \rangle} \quad (1.28)$$

where, on the one hand, $\langle I_{\text{el}} \rangle$ corresponds to the radiation of the average dipole moment, which is characterized by a well defined phase compared to the laser one. This emission component is the resonant Rayleigh scattering (RRS) (i.e. the elastic scattering contribution), which is thus coherent with the excitation laser, and the associated spectrum is similar to the laser spectrum centered at the laser energy $E_L = \hbar\omega_L$. The decoherence time of this RRS component is then characterized by the laser coherence time T_L . On the other hand, $\langle I_{\text{inel}} \rangle$ corresponds to the radiation induced by the random fluctuations of the dipole moment, which is characterized by a random phase compared to the laser one. This emission component is the resonance fluorescence of the TLS (i.e. the inelastic scattering contribution), which is thus incoherent with the laser, and the associated spectrum exhibits the so-called Mollow triplet [97] centered at the transition energy $\hbar\omega_0$. The decoherence time of the inelastic component is imposed by the coupling of the TLS with its environment and is thus equal to T_2 .

In the following, we will refer to the general denomination of resonance fluorescence when considering the total emission of the TLS, i.e. the sum of the elastic and inelastic components. The intensities of the elastic and inelastic components of the TLS emission are deduced from the solutions of the Bloch equations (1.22) in the stationary regime and are written in the radiative limit as:

$$\langle I_{\text{el}} \rangle = \frac{\Omega^2 (\Gamma^2 + 4\Delta^2)}{(\Gamma^2 + 2\Omega^2 + 4\Delta^2)^2} \quad \text{and} \quad \langle I_{\text{inel}} \rangle = \frac{2\Omega^4}{(\Gamma^2 + 2\Omega^2 + 4\Delta^2)^2} \quad (1.29)$$

These expressions can also be written as a function of the TLS relaxation times and the saturation parameter as follows:

$$\langle I_{\text{el}} \rangle = \frac{1}{2} \cdot \frac{T_2}{2T_1} \cdot \frac{s}{(1+s)^2} \quad \text{and} \quad \langle I_{\text{inel}} \rangle = \frac{1}{2} \cdot \frac{\left(1 - \frac{T_2}{2T_1}\right) s + s^2}{(1+s)^2} \quad (1.30)$$

The intensity of the resonance fluorescence with its elastic and inelastic contributions, given by equations (1.24) and (1.30) respectively, are presented as a function of the saturation parameter s_0 in figure 1.13. Two main excitation regimes, $s_0 \ll 1$ and $s_0 \gg 1$, can be distinguished. Below the TLS saturation power ($s_0 \ll 1$), the elastic scattering which depends linearly on the excitation power (i.e. $\langle I_{\text{el}} \rangle \propto s_0$) contrarily to the inelastic component which varies quadratically with the excitation power (i.e. $\langle I_{\text{el}} \rangle \propto s_0^2$), dominates the resonance

fluorescence. The TLS is most of the time in the ground state and the decoherence induced by the coupling of its excited state with the vacuum fluctuations is negligible, leading to the highly coherent signal of RRS. Then, above the TLS saturation power where $s_0 \gg 1$, the inelastic scattering increases until the saturation, whereas the elastic component completely vanishes. By increasing the excitation power, the two levels tend to be equally populated, leading to the neutralization of the average dipole and the suppression of the coherent elastic scattering on this dipole. Consequently, only the incoherent contribution due to inelastically scattering on the fluctuating dipole remains. As a result, the total intensity of the resonance fluorescence is linear at low excitation power and saturates at high excitation power.

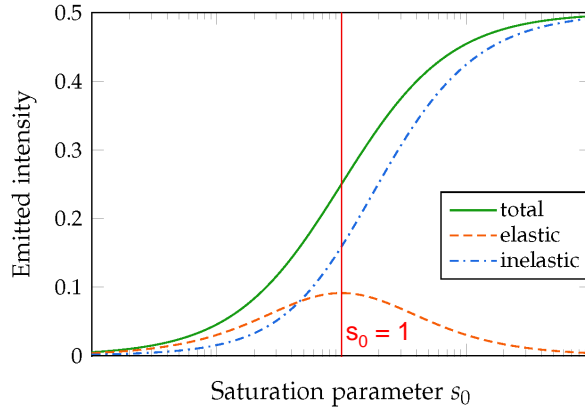


Figure 1.13: Intensity of the resonance fluorescence and of the elastic and inelastic components as a function of the saturation parameter s_0 . The calculation is made for a non-ideal two-level system, where $T_2 = 1.5T_1$. Figure extracted from Ref. [8].

1.4 Conclusion

In this first chapter, we have introduced the general properties of the studied InAs/GaAs semiconductor QDs that are fabricated by epitaxial growth epitaxy techniques in the Stranski-Krastanov mode. Due to the three dimensional confinement of the carriers in semiconductor QDs and the resulting discretization of the energy spectrum, these systems are commonly considered as artificial atoms. Furthermore, when focusing on the fundamental excitonic state, single QDs show very similar optical properties with the atomic TLS and they naturally constitute potential candidates for the development of indistinguishable single photon sources in the solid state. However, in the common non-resonant excitation configuration, the TLS picture for describing such light emitters appears oversimplified. The non-radiative population relaxation processes along with the interactions with the phonons reservoir and the electrostatic environment tend in fact to degrade the temporal coherence of the emitted photons. As a consequence, a strictly resonant excitation of the excitonic transition appears as a fundamental challenge not only to consider a single QD as a genuine artificial atom, but also to realize a source of single photons characterized by high degrees of indistinguishability.

Chapter 2

Measurement of the resonance fluorescence of single quantum dots

As stated in chapter 1, strictly resonant excitation of single quantum dots (QD) appears as a crucial requirement in order to minimize the dephasing processes induced by the phonon and Auger-assisted carriers capture, and therefore to reach the radiative limit and lead to the emission of highly indistinguishable photons. In this chapter, we present the experimental setup that was developed in Laboratoire Pierre Aigrain to measure the resonance fluorescence of a single QD, as well as the specificities of the sample that was used. A typical result of the resonance fluorescence spectrum of a single QD at the energy of the neutral exciton is shown in order to illustrate the success of the resonant excitation setup. However, the reproducibility of such results is limited to only a small amount of QDs and, in most of the cases, a quenching of the resonance fluorescence of the neutral exciton is observed instead. We demonstrate that this serious limitation can be circumvented by the use of an additional ultra-weak non-resonant laser that allows the retrieval and the optical control of the QD resonance fluorescence. A comprehensive experimental study of the main properties of this optical gate along with a theoretical model of the optical gate effect are presented in this chapter.

2.1 Strictly resonant excitation experimental setup

One of the main difficulties of measuring the resonance fluorescence of a single emitter rests in the development of an experimental setup able to suppress the parasitic contribution of the resonant scattered laser (by the sample structural defects for example) that is superimposed with the QD emission in a conventional confocal micro-photoluminescence experiment. We have then developed in the laboratory an original setup which relies on an orthogonal excitation-detection geometry where the excitation and detection optical paths are fully separated and independent¹. At the time this setup was developed, the same configuration was previously used in very few experimental groups [5,6,18]. As sketched in figure 2.1, the excitation of the QDs is done along the lateral facet of the sample by using an optical fiber inserted in the cryostat while the detection is performed along the sample's growth direction by a

¹A cross-polarization configuration, where a polarizer is placed in the collection arm with its polarization perpendicular to the excitation light, can be also used to extinguish the scattered laser and measure the resonance fluorescence [98–101].

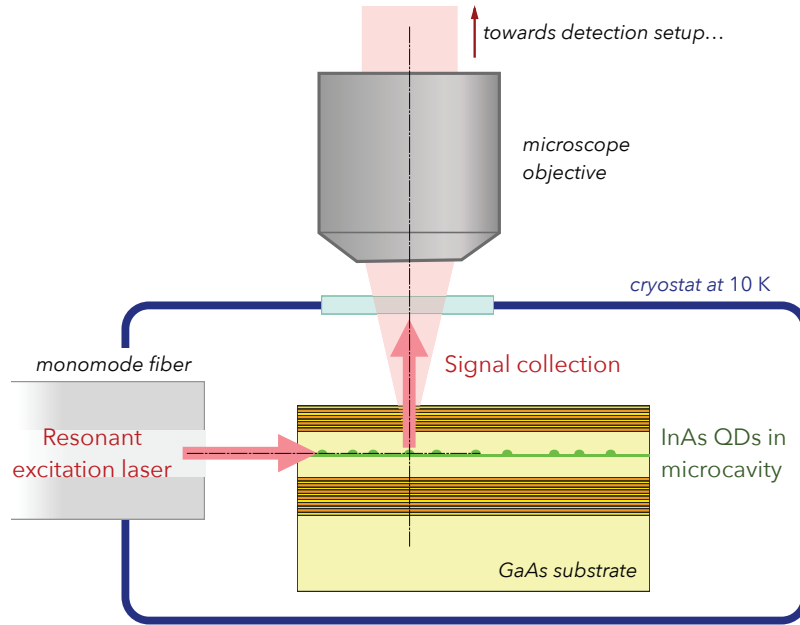


Figure 2.1: Resonant excitation experimental setup showing the schematized sample structure.

microscope objective of a numerical aperture $NA=0.30$. In the cryostat, the sample is fixed whereas the optical fiber is placed on a piezo-electric stage in order to optimize its position with respect to the sample. In the detection path, the emission light passes through a pinhole aperture of $200\ \mu\text{m}$ that is conjugated with the QDs plane, leading to a spatial resolution of $4\ \mu\text{m}$, and is then dispersed by a spectrometer and integrated either by a CCD camera or an avalanche photodiode (APD).

The specificity of the resonant excitation setup also relies on the sample structure that is used (see figure 2.1). In all the experiments presented in this manuscript, the sample consists in a single layer of self-assembled InAs/GaAs QDs inserted in an AlAs/AlGaAs planar microcavity. The planar microcavity is the crucial part of the sample which allows us to succeed in the measurement of the resonance fluorescence of a single QD. Once coupled into the sample through the facet side, due to the large incident angle of the laser on the Bragg mirrors (larger than the total reflection angle) and the strong contrast of the refractive indexes between the air and the GaAs, the laser is confined in the microcavity and propagates along the QDs layer with small divergence. The planar microcavity thus acts as a two-dimensional waveguide for the excitation laser and the main contribution to the laser scattering arises from the edge of the sample or the defects in the Bragg mirrors. The results presented in this manuscript concern QDs located far away from the edge of the sample, approximately at $1\ \text{mm}$, so that the detection of the QD emission is hardly disturbed by the laser scattering on the edge of the sample.

Concerning the characteristics of the sample, the QDs density typically varies from 10^7 to 10^{10} QDs/cm² with an energy distribution of the emission from $1.240\ \text{eV}$ to $1.305\ \text{eV}$ with a maximum at $1.270\ \text{eV}$. In order to perform experiments on single QDs, we focus on the low density region of the sample which is about 10^8 QDs/cm² (i.e. $\sim 1\ \text{QD}/\mu\text{m}^2$). The planar microcavity is a Fabry-Pérot cavity made of two Bragg mirrors which are composed

of alternating AlAs and AlGaAs layers of identical optical thicknesses $\lambda/4$ where $\lambda = \lambda_0/n$ ($\lambda_0 = 1 \mu\text{m}$ and n is the refractive index of the involved material). The cavity spacer is a λ -GaAs layer and the top and bottom Bragg mirrors are respectively composed of 11 and 24 AlAs/AlGaAs pairs, resulting in a finesse of 200. The Fabry-Pérot cavity mode is centered at 1.270 eV (i.e. in resonance with the energy distribution of the QDs emission) with a full width at half maximum of 0.55 meV. Even though the cavity asymmetry degrades the cavity finesse, it facilitates the extraction of the QD emission in the cavity mode in the micro-photoluminescence setup which is used in a reflection configuration.

Two main resonant excitation experiments can be done with the current setup in order to characterize the resonance fluorescence of a single QD: the measurement of the photoluminescence (PL) when the laser energy is fixed at the energy of the studied transition, and the excitation of the photoluminescence (PLE) when the laser energy is varied in the same spectral range as the detection window which is centered at the transition energy. This latter measurement corresponds to a Rayleigh spectroscopy experiment. In both cases, the laser source is a tunable cw external cavity laser diode with a spectral linewidth of 1.25 neV (i.e. 300 kHz) that is much smaller than the exciton linewidth of a few μeV s. The spectral resolution is given by the tuning step that is of the order of 0.5 μeV . Figures 2.2(a) and 2.2(b) show two examples of micro-PL spectroscopy performed with the presented experimental setup on a single QD at 7K. Figure 2.2(a) is a quasi-resonant micro-PL spectrum via the absorption of acoustical phonons, where the energy of the resonant diode laser E_L is slightly detuned from the mean exciton energy E_X ($\Delta = E_L - E_X = -74 \mu\text{eV}$). We observe that the laser light scattering is highly reduced in the orthogonal excitation-detection setup and it is here

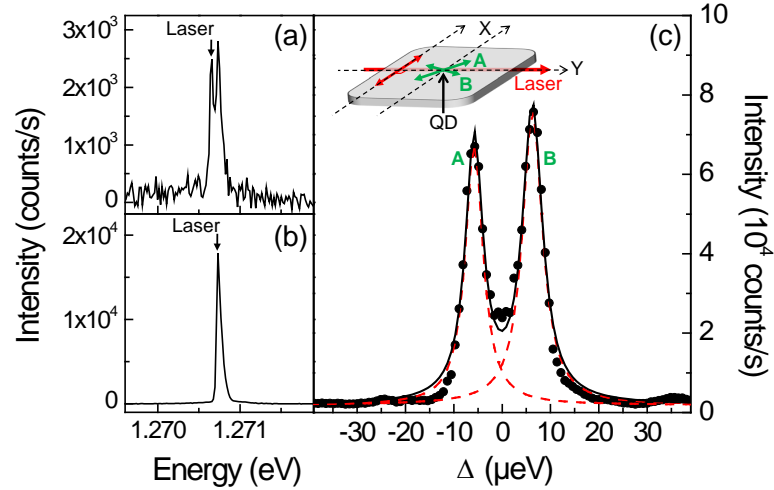


Figure 2.2: Micro-photoluminescence spectrum for a laser detuning with the exciton energy $\Delta = E_L - E_X$ of -74 μeV (a) and -6 μeV (b). (c) Intensity of the QD resonance fluorescence as a function of Δ . The solid line is the sum of two Lorentzian fits (dashed lines) of width 4.4 μeV and 5.0 μeV , separated by 12 μeV , corresponding to the two linear orthogonal polarizations, A and B, of the neutral exciton. Inset: Scheme of the tilted QD axis A and B with respect to the main crystallographic axis [110] and $[1\bar{1}0]$, labeled as X and Y. As only one linear polarization for the excitation laser can be guided in the planar cavity, only one linear polarized component of the exciton would be excited in case of perfect alignment of the QD axis with the main crystallographic axis. Figure extracted from Ref. [24].

comparable to the intensity of the excitonic emission. When the laser is strictly resonant with the exciton line in figure 2.2(b), the intensity is enhanced by a factor 60 due to resonant excitation, this enhancement being only limited by the QD saturation properties. Figure 2.2(c) is an example of a PLE spectrum measured on the same single QD where the intensity of the exciton emission under resonant excitation is plotted as a function of the laser detuning Δ . In comparison to the previous micro-PL spectrum where the exciton linewidth is not resolved, we now observe two Lorentzian lines of width 4.4 μeV and 5.0 μeV , separated by 12 μeV . Additional polarization-resolved measurements show that they correspond to two linear orthogonal polarizations as expected for the fine structure splitting of the neutral exciton [102].

2.2 Quenching of the resonance fluorescence

In practice, it appears that the implementation of the resonant excitation technique is successful for very few QDs since the resonance fluorescence of the neutral exciton is in general not observed. As shown in figure 2.3(b) where the resonance fluorescence is plotted as a function of the laser detuning with respect to the neutral exciton energy, no resonance is observed at zero detuning. This quenching of the resonance fluorescence of the neutral exciton is observed for 90% of the QDs in our sample and, even if the percentage can be different, we stress that this situation is frequently met in other samples coming from other growth facilities [21, 70, 103–106]. Therefore, since the excitation laser is strictly at the energy of the QD fundamental interband transition under resonant excitation, our observation strongly contradicts the expectations for having a quasi-ideal two-level system (TLS), which are based on the upmost reduction of the environment fluctuations under resonant excitation of the QD [53, 102, 107, 108].

The quenching of the resonance fluorescence is typically observed for QDs which show a photoluminescence spectrum under non-resonant excitation in the GaAs barriers with two distinct lines spaced by 1.5 meV (see figure 2.3(a)). Power-dependent studies and photon-correlation measurements [20] were performed to identify the two lines as a neutral exciton X (at $E_X = 1.2736$ eV) and a charged exciton X^+ (at $E_{X^+} = 1.2752$ eV). Moreover, the photoluminescence of the GaAs barriers (see figure 2.4(a)) shows an emission line at 1.495 eV resulting from the radiative recombination of the free electrons in the barriers with the holes bound to the carbon acceptors that constitute the unintentional impurities appearing during the sample growth [109]. These impurities are notably responsible for the presence of residual holes in the sample. Thus, we consider that the charged exciton is a positive trion X^+ , which is further supported by the positive detuning of the charged exciton state with respect to the neutral one [110, 111]. The observation of the positive trion in the non-resonant photoluminescence spectra shows that the QDs in the studied sample may efficiently capture residual holes that exist in the QDs environment. Nevertheless, under these excitation conditions, the simultaneous observation of the two lines indicates that the QD is either empty or populated by at least one hole.

The quenching of the resonance fluorescence of the neutral exciton shows that the situation is completely different under strictly resonant excitation. This is further supported by the result presented in figure 2.3(c) where a signal enhancement is observed when measuring the resonance fluorescence of the positive trion as a function of the laser detuning with respect to the trion energy. We conclude that the resonance fluorescence of the positive trion can be observed because of the presence of at least one residual hole in the QDs. These residual

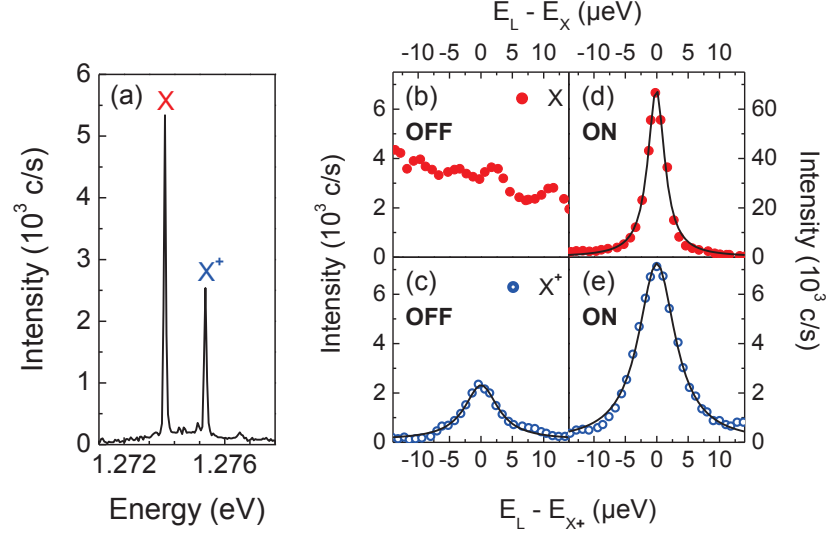


Figure 2.3: (a) Typical spectrum of the non-resonantly excited photoluminescence of a single QD, showing the neutral exciton X and the positive trion X^+ . (b,c,d,e) Resonance fluorescence spectra of X (●) and X^+ (○) as a function of the detuning between the laser energy E_L and the exciton (trion) energy E_X (E_{X^+}) when the optical gate is switched off (b,c) and on (d,e). Figure extracted from Ref. [23].

charges induce a photon absorption at the energy of charged excitonic complexes and not at the neutral exciton one for which the QD must be empty. This phenomenon is similar to the Coulomb blockade effect where the creation of a neutral exciton is blocked by the residual hole in the QD.

This assumption is further supported by the GaAs photoluminescence spectrum presented in figure 2.4(a) and a self-consistent calculation of the QD hole population when no optical excitation is applied, which details can be found in Ref. [23]. First, the emission line at 830 nm in the GaAs photoluminescence spectrum shows that the sample has an unintentional residual carbon doping with bounded holes at low temperature (the carbon binding energy being about 26.7 meV, the thermal activation of the holes is negligible). Then, as schematized in figure 2.4(b), in presence of QDs that introduce bound states well above the Fermi energy, some holes can transfer towards the QDs, leading to the formation of a depletion region around the QD plane. By assuming idealized ensemble of identical QDs, uniformly distributed in the QD plane, one can estimate the density of transferred holes. The main result is presented in figure 2.4(c) where the calculated hole occupancy (left scale) and depletion layer thickness l_A (right scale) are presented as a function of the bulk doping density n_A (at $T = 7$ K, for a QD density of $5 \times 10^7 \text{ cm}^{-2}$). It shows the consecutive filling of the various valence-band QD shells with increasing acceptor density. In particular, we can notice that already two holes dwell in the QDs for a rather low doping density $n_A \approx 10^{11} \text{ cm}^{-3}$.

We stress that, recently, similar quenching effects in electrically tunable QDs have been attributed to the photogeneration by the resonant laser of free carriers from the highly doped back contact of the Schottky diode structure [106]. In that case, the generated electrons by the resonant laser diffuse to the QD and are captured by the QD even at gate voltages where the tunneling is energetically forbidden (this specific configuration is nonetheless observed

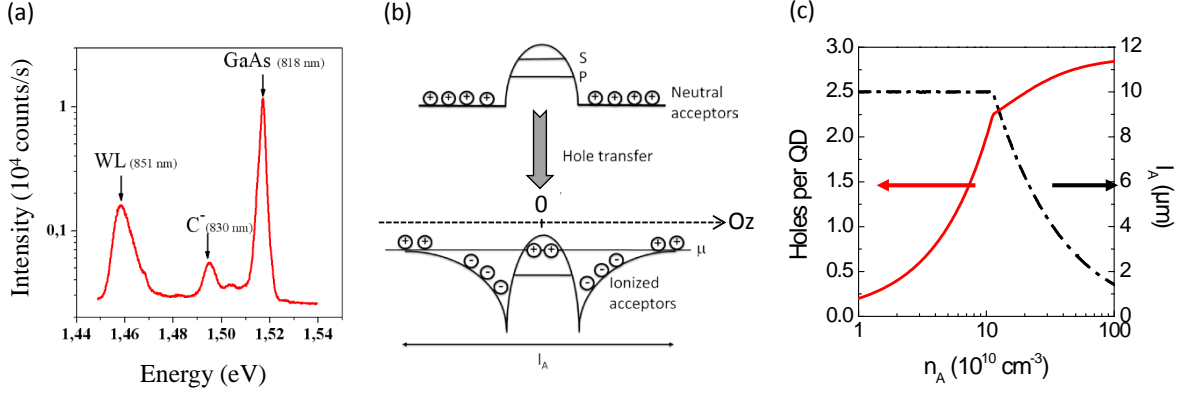


Figure 2.4: (a) Spectrum of the non-resonantly excited photoluminescence of the GaAs, the InAs wetting layer (WL) and the carbon acceptors constituting the unintentional doping introduced during the sample growth. (b) Top: Sketch along the growth direction (Oz) of the valence band of an empty QD surrounded by neutral acceptors from the unintentional residual carbon doping. Bottom: Sketch of the same QD after the acceptors ionization and the resulting holes transfer towards the QD. l_A is the thickness of depletion region around the QD plane and μ the chemical potential fixed to the Fermi energy of the neutral acceptors outside the depletion region. (c) Hole occupancy and depletion length l_A as a function of the bulk doping density n_A , for a QD density $n_{QD} = 5 \times 10^7 \text{ cm}^{-2}$, at $T = 7 \text{ K}$. Figure (a) extracted from Ref. [7]. Figures (b) and (c) extracted from Ref. [23].

for high excitation powers). The quenching effect is here induced by the resonant laser itself for specific gate voltages whereas, in our case, the intrinsic residual doping is responsible for the QD charging prior to the resonant excitation and the resonance fluorescence quenching is observed for every excitation powers of the resonant laser.

2.3 Optical control of the resonance fluorescence

2.3.1 Phenomenology of the optical gate effect

The problem of the quenching of the resonance fluorescence can be circumvented by the use of a very weak additional non-resonant laser that we name in the following as the optical gate. Starting from the experimental configuration used for the QDs resonant spectroscopy, an additional non-resonant laser (a He-Ne laser in resonance with the GaAs barriers or a Ti:Sa laser in resonance with the InAs wetting layer) that is injected perpendicularly to the sample surface via the microscope objective allows retrieving a resonance fluorescence signal of the neutral exciton. This optical gate systematically restores the resonant response of the neutral exciton in the studied QDs. Figure 2.3(d) shows the resonance fluorescence spectrum of the neutral exciton as a function of the laser detuning when the optical gate is switched on. A clear resonance signature with an enhancement factor of about 30 is thus observed at zero detuning when the energy of the laser perfectly matches the exciton one. The optically-gated resonance fluorescence spectrum is fitted with a Lorentzian line of width $3.2 \mu\text{eV}$, comparable to the typical linewidths measured under resonant excitation with various techniques [5, 102, 108]. This optical gate also acts on the trion with an enhancement factor of 3 as shown in figure 2.3(e). As a consequence, we assume that the QD contains possibly more than one hole when the gate is off, which corroborates the role of the residual doping described above.

2.3.2 Main properties of the optical gate effect

Influence on the intensity of the resonance fluorescence: The phenomenology of the optical gate effect shows that an ultra-weak non-resonant laser tends to neutralize the QD and then allows the resonant excitation of the neutral exciton. This optical gate effect has the specificity to occur in a very particular regime where the non-resonant laser does not populate significantly the QD. This statement is illustrated in figure 2.5(a) which presents the intensity of the optically-gated resonance fluorescence and the non-resonant photoluminescence of the neutral exciton as a function of the optical gate power over seven orders of magnitude. The photoluminescence signal, which starts to be significant at $P_{\text{gate}} \sim 0.1 \mu\text{W}$, shows a standard power dependence with a saturation at $P_{\text{gate}}^{\text{sat}} \sim 30 \mu\text{W}$. Concerning the optically-gated resonance fluorescence, measured for a constant resonant excitation power of $5 \mu\text{W}$ ², three remarkable features can be distinguished. First, the resonance fluorescence appears at $P_{\text{gate}} \sim 0.1 \text{ nW}$ and increases to a maximum value $I_{\text{max}} \sim 3.10^4 \text{ counts/s}$ for $P_{\text{gate}} \sim 3 \text{ nW}$, while in this region the non-resonant photoluminescence remains below the detection threshold. Once the maximum signal is reached, the optically-gated resonance fluorescence rapidly decreases for gate powers ranging from 3 nW to 30 nW . At this latter excitation power, the intensity of non-resonant photoluminescence starts to be detectable. From $0.1 \mu\text{W}$, the photoluminescence excited by the optical gate becomes significant while the resonance fluorescence decreases and becomes negligible at $P_{\text{gate}} \sim 30 \mu\text{W}$ where the QD is saturated.

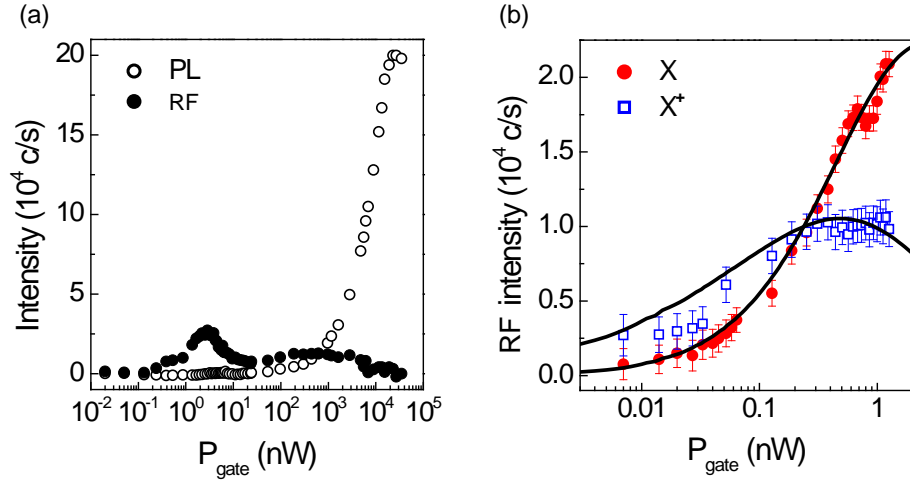


Figure 2.5: (a) Resonance fluorescence (RF) and non-resonant photoluminescence (PL) intensities of the neutral exciton (X) as a function of the optical gate power P_{gate} . (b) Resonance fluorescence intensity of the neutral exciton (X) and the positive trion (X^+) as a function of the optical gate power P_{gate} . Only the region where the non-resonant photoluminescence is completely negligible is displayed. The experimental data are fitted by a population evolution model (solid lines) that is presented in section 2.3.3. Figure extracted from Ref. [23].

The same behavior can be observed on the resonance fluorescence of the positive trion when the optical gate is turned on. Figure 2.5(b) shows the resonance fluorescence intensities of the exciton and the positive trion as a function of the optical gate power in the restricted range

²As will be seen in section 2.4, this power is much lower than the saturation power of the QD resonance fluorescence $P_0 = 16.5 \mu\text{W}$.

0.007 – 2 nW. The experimental results are fitted by a theoretical population evolution model for which a simplified description is given in section 2.3.3. In the studied power range, the non-resonant photoluminescence excited by the gate is completely negligible. For gate powers smaller than 0.5 nW, the trion resonance fluorescence increases with gate power indicating that the residual QD occupation evolves from two to one residual holes. For gate powers larger than 0.5 nW the trion resonance fluorescence saturates before a preliminary decrease, the QD becoming empty.

We assume that the structural defects around the QD contribute to the presence of residual charges inside the QD, which lead to the coexistence of neutral and charged exciton lines. Such a feature is routinely observed in QD samples from different growth facilities [112–114] or made of various materials [90, 115]. Several papers reported the optical control of the QD residual charge in photoluminescence spectroscopy under non-resonant excitation [113, 115]. Although analog to our optical gate effect, it strongly contrasts with our experiments since the techniques used in Ref. [113, 115] refer to a complete incoherent regime where the photoluminescence is non-resonantly excited. Our work demonstrates a novel approach for coherently-driven single QDs. In particular, even in the regime of coherent Rayleigh scattering, where no energy is absorbed in the QD [116], the non-resonant gate laser finely controls the QD ground state (this statement is demonstrated in section 2.4 with figure 2.12).

Influence on the energy of the resonance fluorescence: The latter results demonstrate that the optical gate substantially modifies the QD population. We now consider the consequences related to the QD electrostatic environment. Figure 2.6 displays the resonance fluorescence energies of the neutral exciton, E_X (see figure 2.6(a)), and the positive trion, E_{X+} (see figure 2.6(b)), as a function of the optical gate power P_{gate} . The solid lines are obtained from the theoretical population evolution model presented in section 2.3.3. A red shift of a few μeV s is first observed in the very weak gate power regime, followed by a comparable blue shift when the gate power increases. The transition between the red and blue shift occurs at a typical power of $P_{\text{gate}} \sim 0.05$ nW. This optical gate power is much smaller

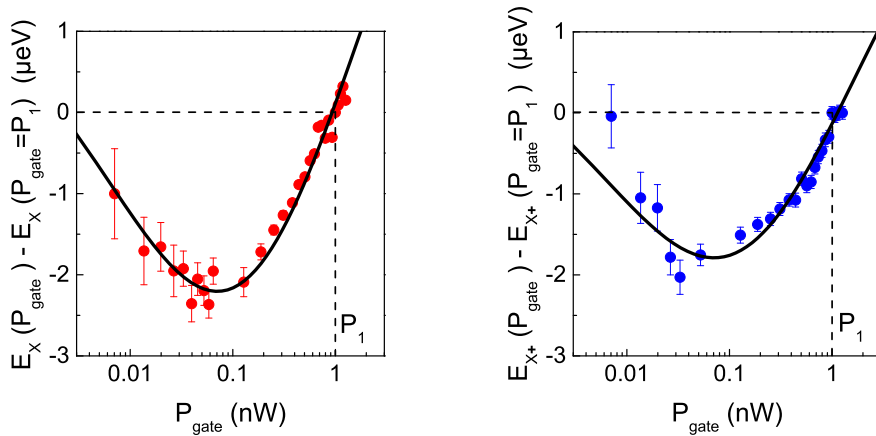


Figure 2.6: Energy of the neutral exciton (left) and positive trion (right) resonance fluorescence as a function of the optical gate power P_{gate} . The experimental data are obtained from the same set of measurements as figure 2.5(b) and are fitted by the population evolution model (solid lines). Figure extracted from Ref. [23].

than the gate powers corresponding to the maximum resonance fluorescence intensities of the exciton ($P_{\text{gate}} \sim 3$ nW) and the trion ($P_{\text{gate}} \sim 0.5$ nW). In fact, the energy shifts of X and X^+ are governed, through the quantum confined Stark effect, by the charge state of the QD environment, while the resonance fluorescence intensity only depends on the charge state of the QD itself.

Transient regime of the optically-gated resonance fluorescence: The two previous studies of the influence of the optical gate power on the intensity and the energy of the resonance fluorescence signal give information on the charge state of the QD and of its surroundings, respectively. In the corresponding experiments, the optical gate is always switched on and the physical properties are average values in the steady state regime. A deeper insight into the physics of the optical gate effect is gained by investigating the switching dynamics of the resonance fluorescence signal and therefore by studying the transient regimes where the optical gate has just been switched on³.

Experimentally, we send two light beams. The first one, provided by the tunable cw external cavity laser diode, resonantly excites the excitonic transition, while the second one is the optical gate (HeNe laser), which is modulated from 0 to a few nWs at 400 Hz by using an acousto-optic modulator. An oscilloscope records a time-histogram of the resonance fluorescence where each detected photon corresponds to one event. The temporal resolution of the experimental setup is evaluated by measuring the system response when the modulated optical gate is directly sent to the photodetector, and turns to be $2 \mu\text{s}$ in the "on stage". In figure 2.7, we observe that the resonance fluorescence intensity increases exponentially with a time constant $t_{\text{on}} = 5 \pm 1 \mu\text{s}$ when the gate laser is switched on, at a power of 3 nW.

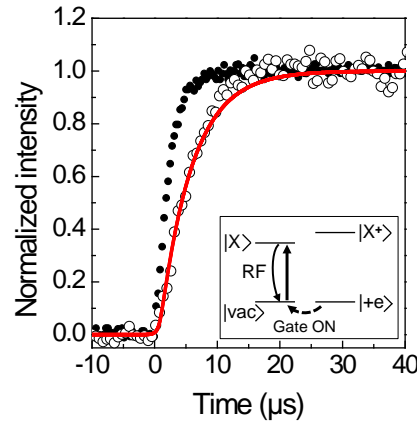


Figure 2.7: Resonance fluorescence intensity as a function of time (\circ) when the gate laser is switched on at $t=0$. The theoretical fit (solid line, red) is the convolution of the system response function (\bullet) with an exponential of time constant $t_{\text{on}} = 5 \pm 1 \mu\text{s}$. Inset: Scheme of the electronic states ($|\text{vac}\rangle$: empty QD; $|+e\rangle$: one hole in the QD; $|X\rangle$: neutral exciton; $|X^+\rangle$: positively charged exciton) and the transitions involved in the optical gate effect (dotted arrow: neutralization of the QD by the optical gate; solid arrows: optical transitions under resonant excitation of the neutral exciton). Figure extracted from Ref. [20].

³The study of the switch-off dynamics has also been studied [23] but is not shown here, the scope of the discussion being the physics of the optical gate effect which allows the retrieval of a resonance fluorescence signal.

An interpretation of this result which is supported by the model described in the section 2.3.3 is the following. Within the time constant t_{on} , an electron that was non-resonantly photogenerated by the gate laser is captured into the QD and radiatively recombines with the residual hole in the QD. Since we use an ultra-weak non-resonant laser for the optical gate, the limiting process for the QD neutralization appears to be the carrier capture into the QD. Contrarily to the standard configuration of photoluminescence spectroscopy under non-resonant excitation where the capture rate is in the range of tens of ps, the optical gate effect occurs in an unprecedented explored regime of ultra-slow capture on microsecond time scales. Therefore, we are led to a picture of a coherently-driven QD where the carriers injected by the gate are slowly captured one-by-one into the QD prior to quasi-simultaneous radiative recombination of an electron-hole pair. The study of the switch-off dynamics shows then that the QD neutralization is limited by the recapture of a hole in the QD: the QD ground state evolves to a stationary hole excess because of the residual doping in the QD environment and the optically-gated resonance fluorescence of the exciton is quenched back after 120 μs [23]. We stress that similar mechanisms relying on ultra-slow captures in the order of milliseconds have been recently reported in electrically tunable QDs [106], where the quenching of the resonance fluorescence is controlled by an additional non-resonant laser which photogenerates free carriers from the doped back contact of the Schottky structure (this optical gating appears nonetheless at much higher optical gate powers with respect to the resonant laser than in our studies).

As a consequence, such capture and recapture processes observed in the transient regime of the optical gate effect leads to a resonance fluorescence intermittency very similar to the blinking phenomenon reported for the nanocrystals [117]. A blinking effect associated to a photon bunching in the auto-correlation function of the neutral exciton measured in a Hanbury Brown and Twiss (HBT) setup (see figure 2.8) is in fact observed⁴. Such a behavior may be reminiscent of the one observed on the non-resonant photoluminescence in QDs and nanocrystals where slow bunching effects due to the so-called spectral diffusion effect [89–91, 118, 119] were observed. Even if the resonance fluorescence flickering due to spectral diffusion has been observed and controlled by an additional laser in QDs [120], the QD charge state fluctuations is in our case the main reason for photon bunching [121, 122] and we observe a blinking between distinct excitonic states, namely the neutral exciton and the other excitonic complexes. Note that a similar blinking behavior had already been observed in the differential transmission of a single QD under resonant excitation [102].

Additional measurements as a function of the optical gate energy show the same intensity variation of the QD resonance fluorescence as the QD photoluminescence non-resonantly excited by the intense optical gate⁵. This similarity between the excitation spectra of the resonance fluorescence and non-resonant photoluminescence confirms the assumption of a radiative recombination as the process involved in the neutralization of the QD by the optical gate.

⁴Even if the HBT setup as well as the second-order correlation function $g^{(2)}$ that is measured in such an experiment are presented in details in chapter 3, these results need to be shown here in order to fully understand the optical gate effect and its limits.

⁵The corresponding PLE measurements can be found in the PhD thesis of Hai Son Nguyen [7]. In that case, the optical gate is a tunable Ti:Sa laser.

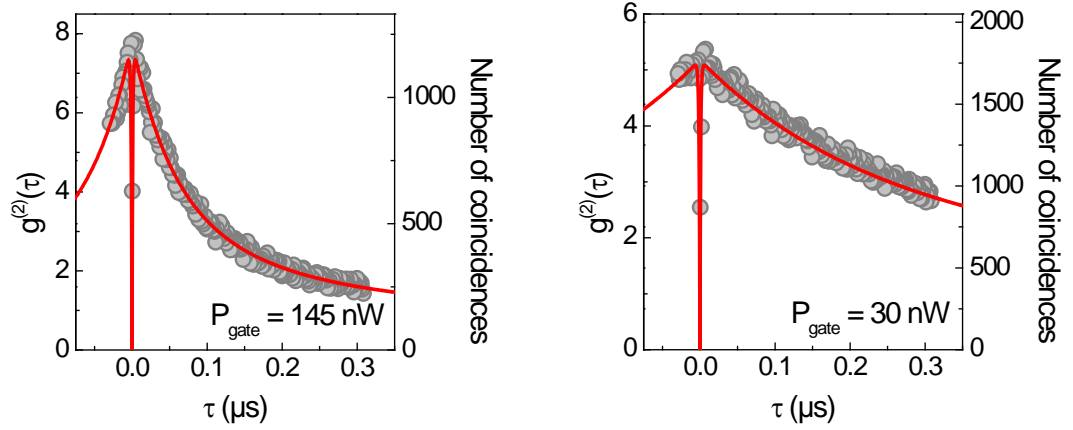


Figure 2.8: Intensity auto-correlation measurements of the optically-gated resonance fluorescence of the neutral exciton, for two optical gate powers (taken from a complete study over 12 gate powers). The experimental data correspond to the number of coincidences as a function of the time delay while the theoretical curves, results of the population evolution model, are plotted on a dual scale by adjusting the experimental and theoretical maxima. Figure extracted from Ref. [23].

2.3.3 Simplified model of the optical gate effect

We interpret the optical gate effect within a model where the QD resonance fluorescence is quenched by Coulomb blockade because of the tunneling of a hole from a structural deep level (DL). The optical gate suppresses Coulomb blockade by switching back the QD into a neutral state. The main processes governing the optical gate effect are sketched in figure 2.9. The defect state is assumed to be close to the QD confined hole state⁶. When the resonant laser and the optical gate are switched off (see figure 2.9(a)), the hole tunnels from the structural deep level to the QD with a time constant τ_{in} , and from the QD back to the deep level with a time constant τ_{out} , the deep level being filled with a rate $1/t_{\text{off}}$. This leads to a residual charge q close to $+e$ in the QD. When the QD is resonantly excited by the resonant laser (see figure 2.9(b)), only the resonance fluorescence of the positive trion is observed since the residual hole in the QD blocks any optical transition at the energy E_X of the neutral exciton because of Coulomb blockade [102]. When the optical gate is switched on (see figure 2.9(c)), the residual hole is ejected from the QD through radiative recombination with one electron photogenerated by the optical gate in the GaAs barriers. The inverse of the t_{on} time thus characterizes the corresponding rate of neutralization. This process is extremely rare since the optical gate is more than four orders of magnitude lower than at the QD saturation. However, when it occurs, it switches the QD back into a neutral state where the resonance fluorescence of the neutral exciton is observable (see figure 2.3(d)). The probability of having no residual hole in the QD is then limited by the recharging of the deep level with a time constant t_{off} .

This phenomenology is well described by a simple rate equations model which gives a rough estimation of the transient time constants t_{on} (and t_{off}) related to the switching dynamics of

⁶Such assumption is corroborated by a recent experimental study where the local electric environment of the QD has been successfully studied by resonant excitation spectroscopy [123].

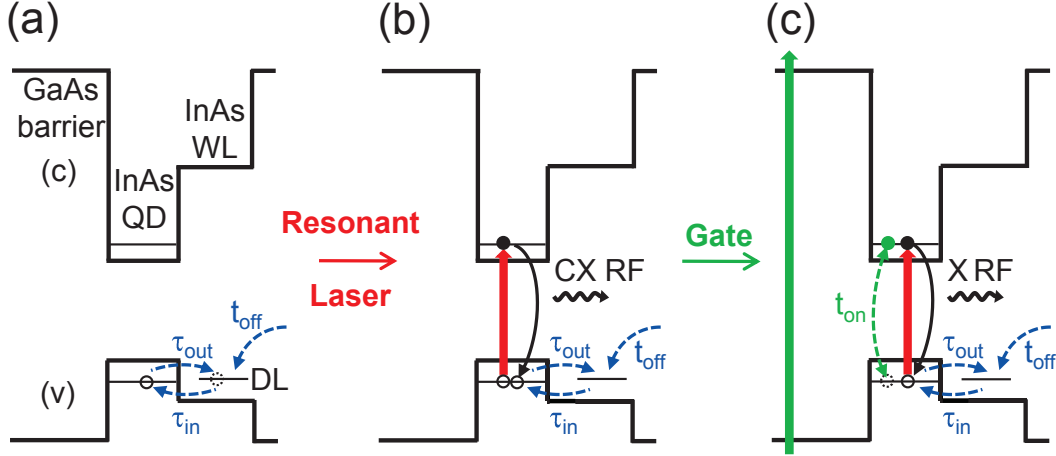


Figure 2.9: Scheme of the valence (v) and conduction (c) band edges in the growth direction of the heterostructure, showing together the InAs wetting layer (WL), the GaAs barriers, the single QD and a deep level (DL) assumed to be close to the confined hole state of the QD, with electrons (\bullet) and holes (\circ). (a) The resonant laser and the optical gate are switched off. A hole tunnels from the DL to the QD and vice-versa, with characteristic times τ_{in} and τ_{out} , respectively. The DL filling with a rate $1/t_{off}$ leads to a residual hole in the QD. (b) The resonant laser (shown by the up solid arrow) is switched on. The QD resonance fluorescence (RF) is observed only at the energy E_{X^+} of the positively charged exciton X^+ . (c) The resonant laser and the optical gate (long solid arrow) are switched on. The residual hole is ejected from the QD after radiative recombination with one electron photogenerated by the optical gate, with a time constant equal to t_{on} . The DL recaptures a hole with a time constant equal to t_{off} . The situation where $t_{on} < t_{off}$ leads to a neutral QD state, and the QD resonance fluorescence is predominantly observed at the energy E_X of the neutral exciton X .

the optical gate effect. The corresponding rate equations are:

$$\begin{aligned} \frac{dp_{DL}}{dt} &= -\frac{p_{DL}(1-p_{QD})}{\tau_{in}} + \frac{p_{QD}(1-p_{DL})}{\tau_{out}} + G(1-p_{DL}) \\ \frac{dp_{QD}}{dt} &= +\frac{p_{DL}(1-p_{QD})}{\tau_{in}} - \frac{p_{QD}(1-p_{DL})}{\tau_{out}} - \mu P_{gate} p_{QD} \end{aligned} \quad (2.1)$$

where p_{QD} and p_{DL} are the probabilities to have one hole in the QD and the deep level, respectively, G the capture rate of one hole in the deep level (assumed to be constant at low optical gate powers), and μP_{gate} the effective radiative recombination rate of the residual hole in the QD, P_{gate} being the optical gate power. This model leads to a transient time t_{on} of the order of $1/\mu P_{gate}$, and to a t_{off} time of the order of $1/G$. In the limit of the QD saturation by the optical gate, μP_{gate} corresponds to the neutral exciton recombination rate γ_R , with $1/\gamma_R = T_1 \sim 500$ ps. Therefore, we rewrite μP_{gate} as $\gamma_R P_{gate}/P_{gate}^{sat}$ with P_{gate}^{sat} the QD saturation gate power of a few tens of microwatts. In the experimental conditions where P_{gate} is equal to a few nanowatts, we get a rough estimate of t_{on} of 5 μ s, fully consistent with the measured one. Moreover, measurements on increasing the optical gate power (not shown here) show (i) a decrease of t_{on} as a function of P_{gate} , and (ii) an approximately constant t_{off} value, as predicted by our model. Finally, the higher the ratio t_{off}/t_{on} , the lower the residual charge q in the QD and the more intense the resonance fluorescence of the neutral exciton.

A detailed model can be found in Ref. [7, 23] where the electron QD population induced by the optical gate is taken into account as well as the electron and hole populations created

by the resonant laser. This detailed model relies on a population evolution model similar to the one proposed by J. Gomis-Bresco *et al.* [124], which adapts for excitons the random population model of M. Grundmann *et al.* [125]. Within this approach, all the processes related to the charge capture, the radiative recombination, and the resonant pumping are taken into account by considering all the possible charge configurations of the QD (restricted in our case to the neutral exciton X , the positive and negative trions X^\pm and the biexciton XX). This population model allows the determination of the nature of the capture processes involved in the resonance fluorescence optical gate effect. While other groups [42, 124] have previously used the non-resonant photoluminescence to evaluate the carriers capture rates, we benefit here from the resonant excitation and its optical gating effect to probe the QD ground state, which is determined by the capture of the electrons and holes created by the non-resonant laser. In particular, this method gives access to ultra-slow capture processes in the very low gate power regime where the non-resonant photoluminescence is completely negligible. Inversely, when the non-resonant photoluminescence is observed, the capture rates are already at least of the order of 1 ns^{-1} [124]. In the context of our unusual experiments, the population model that we used allows us to estimate capture rates from a few ms^{-1} to a few hundreds of ps^{-1} in the explored power range (i.e. seven orders of magnitude) that are in very good agreement with theoretical calculations of the capture processes assisted by Auger effect [44, 45] and optical phonons emission [43].

2.4 Retrieval of the properties of a quasi-ideal two-level system

Up to now, the system of the resonantly-driven QD controlled by the optical gate has been described by a quite complex system involving multiple charge states. However, as suggested by the blinking behavior of the optically-gated resonance fluorescence (see figure 2.8), the resonant laser induces a resonant signal during a typical time of a few hundreds of nanoseconds for which only two states, the excitonic state $|X\rangle$ and the QD empty state $|\text{vac}\rangle$, are concerned. Then, at the operating low powers of the optical gate, the QD emission can be assimilated to the emission of a TLS. This simplified picture is in fact reached in the low power regime where the capture of the carriers can be seen as a one-by-one capture. The following experimental results have then been measured for a constant low optical gate power of $P_{\text{gate}} \sim 3 \text{ nW}$.

We show in the following that intrinsic properties of a quasi-ideal TLS under resonant excitation are recovered when the optical gate is switched on, the power of the resonant laser being equal to $4 \text{ }\mu\text{W}$. Figure 2.10 first presents time-resolved measurements of the optically-gated QD emission under resonant excitation of the excitonic transition. Apart from a spurious contribution of the ID Quantique photodetector that appears at long time delays, one can extract the QD lifetime $T_1 = 330 \pm 20 \text{ ps}$ which is a standard value for epitaxially grown semiconductor QDs [126].

As mentioned in chapter 1, section 1.3.2, the power-dependence of the optically-gated resonance fluorescence then allows for the evaluation of the decoherence time T_2 . Figure 2.11 displays the intensity at zero detuning ($\Delta = 0$) (see figure 2.11(a)) and the linewidth of the optically-gated resonance fluorescence spectrum Γ (see figure 2.11(b)) as a function of the power of the cw resonant diode laser. The intensity of the resonance fluorescence signal first increases linearly with the excitation power, and then displays the typical saturation expected at high powers. This saturation behavior is in fact characteristic of a TLS where

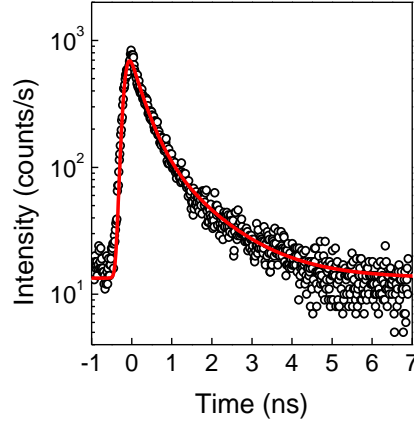


Figure 2.10: Time-resolved resonance fluorescence of the QD when the gate is switched on. The solid line is a fit with a decay time $T_1 = 330 \pm 20$ ps . Figure extracted from Ref. [20].

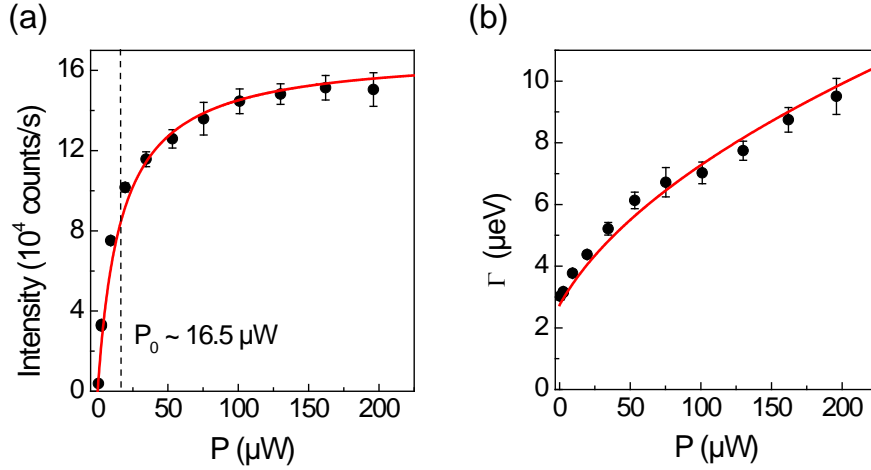


Figure 2.11: Intensity (a) and linewidth (b) of the optically-gated resonance fluorescence spectrum versus the power of the resonant laser. The experimental data are fitted by using equations (2.2) and (2.3), corresponding to a two-level system model (solid line). Figure extracted from Ref. [20].

the charged excitonic states or the biexciton state are not populated. In parallel, we observe the text-book power-broadening of the resonance fluorescence spectrum, with a linewidth increasing by a factor of three in our investigated range of excitation power. The theoretical expressions of the emission intensity I at zero detuning ($\Delta = 0$) and the linewidth $\hbar\Gamma$, that were introduced in chapter 1 for a TLS under resonant excitation (see Eq. (1.24) and Eq. (1.26) where $\text{FWHM}_{\Delta \cdot T_2}$ is equivalent to Γ), are reminded here with the appropriate notations:

$$I \propto \frac{\Omega^2 T_1 T_2}{1 + \Omega^2 T_1 T_2} = \frac{P}{P + P_0} \quad (2.2)$$

$$\hbar\Gamma = \frac{2\hbar}{T_2} \sqrt{1 + \Omega^2 T_1 T_2} = \frac{2\hbar}{T_2} \sqrt{1 + \frac{P}{P_0}} \quad (2.3)$$

where Ω is the Rabi frequency, T_1 the population lifetime, T_2 the decoherence time, P the

power of the resonant laser and P_0 the saturation power of the TLS (the TLS saturation parameter being $s_0 = P/P_0$). The experimental data presented in figure 2.11 are perfectly well fitted to equations (2.2) and (2.3), with $T_2 = 480 \pm 10$ ps and $P_0 = 16.5 \pm 1.5$ μ W.

We then deduce from the extracted value of T_2 that $T_2 \sim 1.5T_1$, meaning that the QD homogeneous linewidth is very close to its radiative limit ($T_2 = 2T_1$). More precisely, our experimental data indicate that the pure dephasing time T_2^* is of the order of 1.8 ns, T_2^* being defined by $1/T_2 = 1/2T_1 + 1/T_2^*$. Such a pure dephasing time attests for the reduction of the environment fluctuations under resonant excitation where spectral diffusion effects are minimized [53, 91]. We further conclude that the intrinsic features of a TLS under resonant excitation are clearly restored by the ultra-weak optical gate. In particular, our technique is validated in both regimes of elastic and inelastic resonance fluorescence. For $P \ll P_0$, the resonance fluorescence consists in the elastic signal of resonant Rayleigh scattering (RRS), whereas at saturation, the inelastic photoluminescence dominates the resonance fluorescence (the specificities of these two regimes for QDs, such as the spectral properties and the photon statistics, are presented in chapter 3). For example, in figure 2.3(d), for a given detuning, the recorded intensity consists in the spectrally integrated signal of both components.

More specifically, to highlight the unique influence of the optical gate and avoid any confusion between the optically-gated resonance fluorescence and a standard non-resonantly excited photoluminescence signal, we show that the elastic component of the resonance fluorescence is also restored by the optical gate⁷. High-resolution measurements by Fourier transform spectroscopy of the resonance fluorescence at zero detuning ($\Delta = 0$) for $P/P_0 = 2.4$ shows in fact the superposition of the elastic and inelastic components of the resonance fluorescence (see figure 2.12(a)). The elastic component corresponds to the quasi constant background which is associated to the coherence time of the resonant laser, whereas the inelastic component corresponds to the fast decay of 480 ps which is the decoherence time T_2 previously measured. Our data are fitted (solid lines in figure 2.12(a)) to the first-order correlation function $g^{(1)}(\tau)$ of the resonance fluorescence of a TLS (see chapter 3, Eq. (3.6)) with the following parameters: $\hbar\Omega = 2.5$ μ eV, $T_1 = 330$ ps and $T_2 = 480$ ps (the contribution of the laser coherence time T_L appears in the quasi-constant background and is assimilated to a constant). We stress that the QD dipole moment, defined as $\mu = \hbar\Omega/\mathcal{E}$ with \mathcal{E} the electric field amplitude, can be deduced from the fitted value of the Rabi frequency. From the power of the resonant excitation laser $P = 40$ μ W (measured before coupling into the optical setup) and the estimated waveguide cross-section $S = 0.83$ μm^2 , we deduce $\mathcal{E} \sim 0.024$ kV/cm from which we obtain an estimation of $\mu \sim 50$ D. This dipole moment is in agreement with other estimations in similar InAs QDs ranging from 20 to 60 D [62, 73, 127, 128]. In the spectral domain, the two components can also be distinguished in the spectrum presented in figure 2.12(b) which corresponds to the Fourier transform of the theoretical fit of the $g^{(1)}$ function. The radiatively-limited spectrum of 2 μ eV width is also superimposed as a reference (gray line in figure 2.12(b)). The inelastic component (dashed line in figure 2.12(b)) is broader than the radiatively-limited emission line, whereas the central peak of the RRS is much narrower than the natural line. Indeed, we demonstrate that the ultra-weak non-resonant optical gate induces the recovery of the properties of an artificial atom even in the coherent regime of

⁷Even if the study of the different components of the resonance fluorescence of a single QD, as well as the different experiments at stake, are presented in details in chapter 3, this statement needs to be developed here in order to give a proper insight of the originality of the optical gate effect. In fact, it must be here differentiated from an optical control of the QD residual charge which has been observed in the incoherent photoluminescence under non-resonant excitation [113, 115].

RRS. Recent experiments also showed that the photo-neutralization of the QD by an optical gate does not degrade the coherence in a pulsed two-photon resonant excitation scheme [129], which is important for the generation of entangled photon pairs with high probability [61].

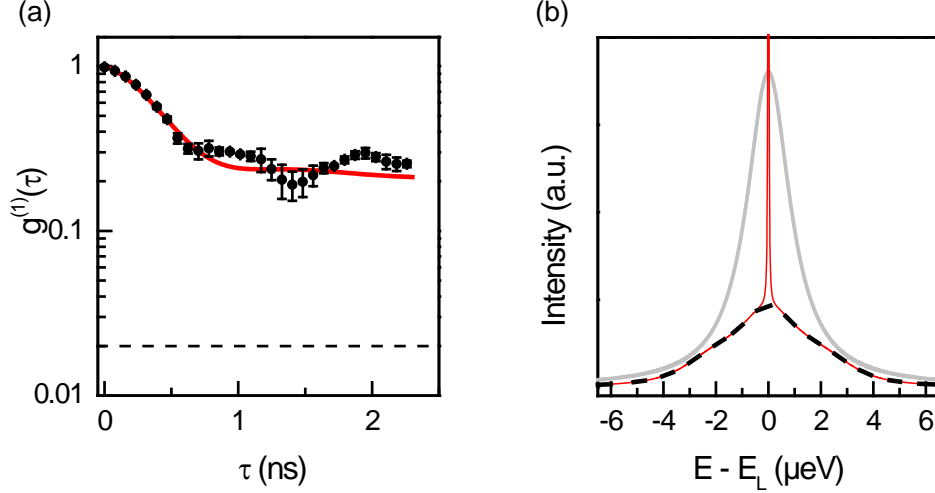


Figure 2.12: (a) High-resolution Fourier transform spectroscopy of the optically-gated resonance fluorescence, at zero detuning ($\Delta = 0$), for $P/P_0 = 2.4$. The data are fitted (solid line) by using the theoretical $g^{(1)}$ function of a two-level system (see chapter 3, Eq. (3.6)) with $\hbar\Omega = 2.5 \mu\text{eV}$, $T_1 = 330 \text{ ps}$ and $T_2 = 480 \text{ ps}$ (the contribution of the laser coherence time T_L appears in the quasi-constant background and is assimilated here to a constant). (b) Spectrum of the resonance fluorescence obtained by Fourier transform of the fit of the $g^{(1)}$ function (red solid line). The inelastic contribution appears as a dashed line and the radiatively-limited emission line of width $2 \mu\text{eV}$ has been superimposed as a gray solid line. Figure extracted from Ref. [20].

We finally discuss the quantum properties of the optically-gated resonance fluorescence in single QDs. Figure 2.13 presents the normalized intensity auto-correlation measurements by the HBT setup⁸ under resonant excitation at zero detuning ($\Delta = 0$), when the optical gate is switched on. This auto-correlation function is presented for a temporal scale much smaller than the bunching time exhibited in figure 2.8 so that the bunching related to the blinking effect is not observed here and the emission can be considered as a continuous stream of photons. After subtracting the noise contribution, we observe a pronounced dip at zero time delay with $g^{(2)}(0) = 0.06$. This is a clear evidence of the characteristic photon antibunching in a single photon source [5, 13, 18]. Most importantly, it further shows that the ultra-weak gate laser does not degrade the non-classical properties of a single QD emission. Our data are well fitted by the convolution of the system response function of 300 ps resolution with the theoretical intensity auto-correlation function $g^{(2)}(\tau)$ of the resonance fluorescence of a TLS (see chapter 3, Eq. (3.22)). Taking into account the previous measured values of T_1 and T_2 , the data are fitted with $\hbar\Omega = 1.4 \pm 0.1 \mu\text{eV}$.

⁸The HBT setup and the second-order correlation function $g^{(2)}$ that is measured in such an experiment are presented in details in chapter 3.

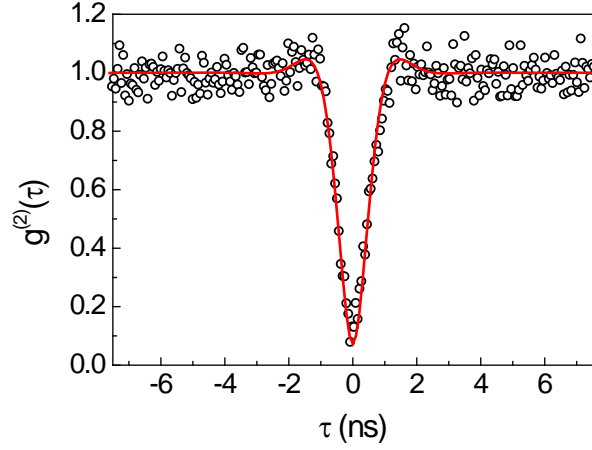


Figure 2.13: Intensity auto-correlation measurements under resonant excitation at $\Delta = 0$, for $P/P_0 = 0.7$, when the optical gate is switched on. The data are fitted by equation (3.22) with the parameters: $T_1 = 330$ ps, $T_2 = 480$ ps, and $\hbar\Omega = 1.4$ μ eV. Figure extracted from Ref. [20].

2.5 Conclusion and perspectives for achieving the radiative limit

This chapter has highlighted the role of the electrostatic environment on the optical resonant response of a single QD. Although a resonant excitation does not create charges in the vicinity of the QD, the presence of residual charges coming from non-intentional doping can induce a quenching of the resonance fluorescence via a phenomenon similar to the Coulomb blockade effect. We demonstrated that the use of an ultra-weak non-resonant laser allows the optical gating of the QD resonant response by controlling the QD ground state. More specifically, the gate effect relies on the photo-neutralization of the QD where the carriers are captured one-by-one in the specific regime of low gate power, leading to the ejection of the residual holes from the QD. Therefore, the population of the QD ground state and thus the intensity of the optically-gated resonance fluorescence depend on the carriers capture rates which vary with the power of the optical gate. In this context, we showed that the optical gate not only restores the resonance fluorescence of the neutral exciton but also induces a recovery of the properties of an artificial atom characterized by the emission of single photons with a decoherence time closed to the one imposed by the radiative limit. In particular, we demonstrated that the optical gate effect is efficient even in the coherent regime of RRS. We stress that the use of an additional weak non-resonant laser also appears to be interesting to probe the local environment fluctuations at the single charge level in single QD [130,131] and to minimize this environment fluctuations to improve the emitted photons indistinguishability [70].

Nevertheless, because the QD neutralization relies on a slow carriers' capture in the operating regime of the optical gate, the resonance fluorescence is restored by intermittency with an "all or nothing" behavior which induces a blinking phenomenon similarly to the one observed in nanocrystals [117]. The resonance fluorescence of the neutral exciton is in fact inhibited during time intervals for which the QD ground state is a charged state, while the photons emitted during the remaining time constitute the emission of a real but non-ideal TLS. The existence of a residual doping in the vicinity of the QD, which is responsible for the blinking of the resonance fluorescence, thus prevents the radiative limit $T_2 = 2T_1$ to be

reached. When demonstrating that semiconductor QDs can constitute efficient sources of single indistinguishable photons or entangled photons pairs for quantum information applications, not reaching the radiative limit appears as a major drawback. In fact, the degree of entanglement is maximum in absence of pure dephasing, the limit condition to fulfill the violation of the Bell inequalities being $T_2/2T_1 > 1/\sqrt{2}$. Note that the studied QD fulfills this condition with the measured T_1 and T_2 , which verifies the ratio $T_2/2T_1 = 0.73 \simeq 1/\sqrt{2}$, but an improvement of this ratio is mandatory to perform quantum optics experiments with good visibilities.

As a consequence, even if the resonant excitation configuration already allows to greatly reduce the interactions of the QD with its electrostatic environment, a better control of the residual doping is necessary to reduce the pure dephasing and increase the decoherence time T_2 . As the doping is inherent to the growth of epitaxial structures and cannot be suppressed, the main perspective is to specifically design a doped sample with electrical contacts in order to control the charge state of the QDs as well as the charge fluctuations in its vicinity by applying a vertical external static electric field. This would not only circumvent the permanent dynamics of the QD states which is responsible for the blinking effect, but also possibly induce an inhibition of dephasing by motional narrowing assisted by tunneling of carriers out of the defects located close to the QD. Such a configuration has been intensively studied at LPA by A. Berthelot et al. [132] for single QDs under non-resonant excitation. In this study, the QDs were embedded in a field-effect structure which consisted in a n-Schottky heterostructure allowing the electrical control of the QD charge state and of the spectral diffusion by varying the applied gate voltage. In the case of resonant excitation, a more complex structure must be designed in order to combine a diode structure and the QD-microcavity sample necessary for the resonant orthogonal excitation-detection geometry. To that end, the photonic structures can be doped to form a p-i-n diode or a n-Schottky diode, the QD layer being located in the intrinsic region and the Bragg mirrors doped. This technique has been employed to photonic structures such as planar microcavities [133], micropillars [134–136] or photonic crystals [137] with great successes.

Chapter 3

The specificity of the resonance fluorescence of single quantum dots

In this chapter, we focus on the specificity of the excitonic emission of a cw resonantly-driven quantum dot (QD) when no optical gate is applied in order to avoid the contribution of the photo-neutralization mechanism described in chapter 2. Nevertheless, we stress that similar experimental results have been observed for the optically-gated resonance fluorescence. The spectral properties of the resonance fluorescence of another single QD are studied by measuring the first-order correlation function, $g^{(1)}(\tau)$, in a Fourier transform spectroscopy setup, while its emission statistics is investigated by measuring the second-order correlation function, $g^{(2)}(\tau)$, in a Hanbury Brown and Twiss (HBT) interferometer. These correlation functions, that are defined in the formalism introduced by R. J. Glauber [138], are first investigated for a resonantly-driven two-level system (TLS). Then, they are experimentally measured as a function of the excitation power, in the low power regime, i.e. before the saturation of the TLS, and in the high power regime once the saturation of the TLS is reached. The two contributions of the QD resonance fluorescence are characterized: the coherent component which consists in the elastic scattering of the laser photons on the TLS; and the inelastic component which corresponds to the fluorescence emission of the QD. We show that these two contributions present very different spectral properties which are related to different coherence time constants while the emission statistics remains the one of a single photon source. In particular, we focus on the properties of the resonant Rayleigh scattering (RRS) regime where the photons are scattered one by one while keeping a coherence time inherited by the excitation laser. This phenomenon has been rarely studied in QDs since the first measurement of the resonance fluorescence of a single QD by A. Muller *et al.* [5]. It has first been investigated in our group in 2011 [24] followed by few other works [98, 120, 139, 140]. As predicted by theory and shown by homodyne and heterodyne detection experiments [120, 139, 140], the scattered photons inherit the coherence time of the excitation laser T_L , which can be much longer than T_2 , while still exhibiting sub-Poissonian statistics [24, 98]. The resulting QD emission spectrum can then be much narrower than the natural linewidth imposed by the radiative limit, even if the percentage of elastically scattered photons remains limited to $T_2/2T_1$

3.1 Spectral properties

3.1.1 First-order correlation function of the resonance fluorescence

The first-order correlation function of the electric field of a light source is directly related to its spectral properties and therefore to the decoherence time T_2 of the emitted photons. The corresponding normalized function is defined in the stationary regime¹ as [95]:

$$g^{(1)}(\tau) = \frac{\langle E^{(-)}(r, t) E^{(+)}(r, t + \tau) \rangle}{\langle E^{(-)}(r, t) E^{(+)}(r, t) \rangle} \quad (3.1)$$

where r is the position of the detector and τ is the time delay between two detection events. Considering only the light emitted by a single source allows us to avoid the spatial dependance of the correlation functions. Then, the first-order correlation function simplifies as:

$$g^{(1)}(\tau) = \frac{\langle E^{(-)}(t) E^{(+)}(t + \tau) \rangle}{\langle E^{(-)}(t) E^{(+)}(t) \rangle} = \frac{G^{(1)}(\tau)}{G^{(1)}(0)} \quad (3.2)$$

where $G^{(1)}(\tau) = \langle E^{(-)}(t) E^{(+)}(t + \tau) \rangle$ is the non-normalized first-order correlation function. When considering a resonantly-driven TLS in the rotating frame approximation, one has to take into account the phase accumulated by the electric field from the origin time t_0 to the times t and $t + \tau$, $\phi_{t_0 \rightarrow t}$ and $\phi_{t_0 \rightarrow t + \tau}$, respectively. Then, using the equations (1.19), (1.18) and (1.17), the $G^{(1)}$ function can be written as:

$$G^{(1)}(\tau) \propto \langle e^{+i\phi_{t_0 \rightarrow t}} S_+(t) e^{-i\phi_{t_0 \rightarrow t + \tau}} S_-(t + \tau) \rangle = e^{-i\phi_{t \rightarrow t + \tau}} \langle S_+(t) S_-(t + \tau) \rangle \quad (3.3)$$

where $\phi_{t \rightarrow t + \tau}$ is the resulting phase accumulated from t to $t + \tau$. This phase is composed of an oscillating part at the laser pulsation ω_L and a fluctuating part such as [96]:

$$e^{-i\phi_{t \rightarrow t + \tau}} = e^{-i\omega_L \tau} \cdot \langle e^{i\theta} \rangle \quad (3.4)$$

where θ is a phase corresponding to a random walk of scattering rate $\Gamma_L = 1/T_L$, such as $\langle e^{i\theta} \rangle = \sum P(\theta) e^{i\theta} d\theta = e^{-\frac{\tau}{T_L}}$, $P(\theta)$ being the probability density of a white gaussian noise over θ and T_L the coherence time of the laser.

As a result, the normalized first-order correlation function can be written as:

$$g^{(1)}(\tau) = e^{-i\omega_L \tau} \cdot e^{-\frac{\tau}{T_L}} \cdot \frac{\langle S_+(t) S_-(t + \tau) \rangle}{\langle S_+(t) S_-(t) \rangle} \quad (3.5)$$

The analytical solutions of the optical Bloch equations² (1.22) in the case of a strictly resonant excitation ($\Delta = E_L - E_X = 0$) leads to [7, 96]:

$$g^{(1)}(\tau) = e^{-i\omega_L \tau} \cdot e^{-\frac{\tau}{T_L}} \cdot \left[\frac{\frac{T_2}{2T_1}}{1 + \Omega^2 T_1 T_2} + \frac{1}{2} e^{-\frac{\tau}{T_2}} + \frac{1}{2} e^{-\eta \tau} \cdot [\alpha \cos(\nu \tau) + \beta \sin(\nu \tau)] \right] \quad (3.6)$$

¹For sake of clarity, we intentionally avoid the indication of the stationary regime in the expressions.

²The calculation consists in the analytical calculation of $\langle S_{\pm}(t) \rangle$ and $\langle S_{\pm}(t + \tau) \rangle$ in order then to deduce the correlation term $\langle S_+(t) S_-(t + \tau) \rangle$ by the quantum regression theorem [54].

with:

$$\begin{aligned} \eta &= \frac{1}{2} \left[\frac{1}{T_1} + \frac{1}{T_2} \right] & \nu &= \sqrt{\Omega^2 - \frac{1}{4} \left[\frac{1}{T_1} - \frac{1}{T_2} \right]^2} \\ \alpha &= 1 - \frac{T_2}{T_1(1+\Omega^2 T_1 T_2)} & \beta &= \frac{\Omega^2 T_1 (3T_2 - T_1) - \frac{(T_1 - T_2)^2}{T_1 T_2}}{2\nu T_1 (1+\Omega^2 T_1 T_2)} \end{aligned} \quad (3.7)$$

We note that the relaxation times T_1 and T_2 play a non symmetrical role in the $g^{(1)}$ function and we stress that this function is fundamentally different from the non-resonant excitation case where it depends only on T_2 .

Finally, at a given detuning and a given excitation power, the spectral density of the intensity defined by (1.21) can be written as a function of the first-order correlation function such as [95]:

$$\mathcal{I}(\Delta, \omega) = \frac{1}{2\pi} \int_{-\infty}^{+\infty} e^{i\omega\tau} G^{(1)}(\tau) d\tau \quad \text{or} \quad G^{(1)}(\tau) = \int_{-\infty}^{+\infty} e^{-i\omega\tau} \mathcal{I}(\Delta, \omega) d\omega \quad (3.8)$$

As presented in chapter 1, section 1.3.3, the emission spectrum of a resonantly-driven TLS, given directly by $\mathcal{I}(\Delta, \omega)$, consists in an elastic (or coherent) and an inelastic (or incoherent) contributions. Therefore, in the case of a QD resonantly excited at the exciton energy (i.e. $\Delta = 0$), the spectrum corresponds to:

$$\mathcal{I}(\omega) = \mathcal{I}_{\text{el}}(\omega) + \mathcal{I}_{\text{inel}}(\omega) \quad (3.9)$$

where $\mathcal{I}_{\text{el}}(\omega)$ and $\mathcal{I}_{\text{inel}}(\omega)$ are the spectra of the elastic and inelastic components of the resonance fluorescence, respectively. These two contributions are written as [7, 96]:

$$\mathcal{I}_{\text{el}}(\omega) = \frac{1}{4\pi} \frac{T_2}{2T_1} \frac{s_0}{(1+s_0)^2} \frac{\frac{1}{T_L}}{(\omega - \omega_0)^2 + \left(\frac{1}{T_L}\right)^2} \quad \text{and}, \quad (3.10)$$

$$\begin{aligned} \mathcal{I}_{\text{inel}}(\omega) &= \frac{1}{2\pi} \frac{s_0}{1+s_0} \left[\frac{\frac{2}{T_C}}{(\omega - \omega_0)^2 + \left(\frac{1}{T_C}\right)^2} + \frac{\tilde{\eta}\alpha + (\omega + \nu - \omega_0)\beta}{(\omega + \nu - \omega_0)^2 + \tilde{\eta}^2} + \frac{\tilde{\eta}\alpha - (\omega - \nu - \omega_0)\beta}{(\omega - \nu - \omega_0)^2 + \tilde{\eta}^2} \right] \\ &\simeq \frac{1}{2\pi} \frac{s_0}{1+s_0} \left[\frac{\frac{2}{T_2}}{(\omega - \omega_0)^2 + \left(\frac{1}{T_2}\right)^2} + \frac{\eta\alpha + (\omega + \nu - \omega_0)\beta}{(\omega + \nu - \omega_0)^2 + \eta^2} + \frac{\eta\alpha - (\omega - \nu - \omega_0)\beta}{(\omega - \nu - \omega_0)^2 + \eta^2} \right] \end{aligned} \quad (3.11)$$

where $\frac{1}{T_C} = \frac{1}{T_2} + \frac{1}{T_L} \simeq \frac{1}{T_2}$ and $\tilde{\eta} = \eta + \frac{1}{T_L} \simeq \eta$, since $T_L \gg (T_1, T_2)$. We remind that $s_0 = \Omega^2 T_1 T_2$ is the saturation parameter of the TLS at $\Delta = 0$.

To illustrate the expected spectral properties of the resonance fluorescence of a single QD, figure 3.1 presents theoretical spectra calculated from equations (3.10) and (3.11) at the radiative limit (i.e. $\Gamma = \frac{1}{T_1} = \frac{2}{T_2}$), for different excitation powers given by the saturation parameter s_0 ($(\frac{\Omega}{\Gamma})^2 = \frac{s_0}{2}$ in the figure). The two distinct power regimes defined by $s_0 \ll 1$ and $s_0 \gg 1$ that were presented in chapter 1, section 1.3.3, can also be distinguished in the power dependence of the resonance fluorescence spectrum: below the saturation power ($s_0 \ll 1$), where the RRS elastic component dominates, the spectrum presents a narrow line which is identical to the spectrum of the excitation laser; whereas above the saturation power ($s_0 \gg 1$), where the inelastic component dominates, the spectrum consists in the so-called Mollow triplet [97] characterized by a central line at the transition energy $\hbar\omega_0$ accompanied by two side lines separated by the Rabi energy at $\hbar\omega_0 \pm \hbar\Omega$.

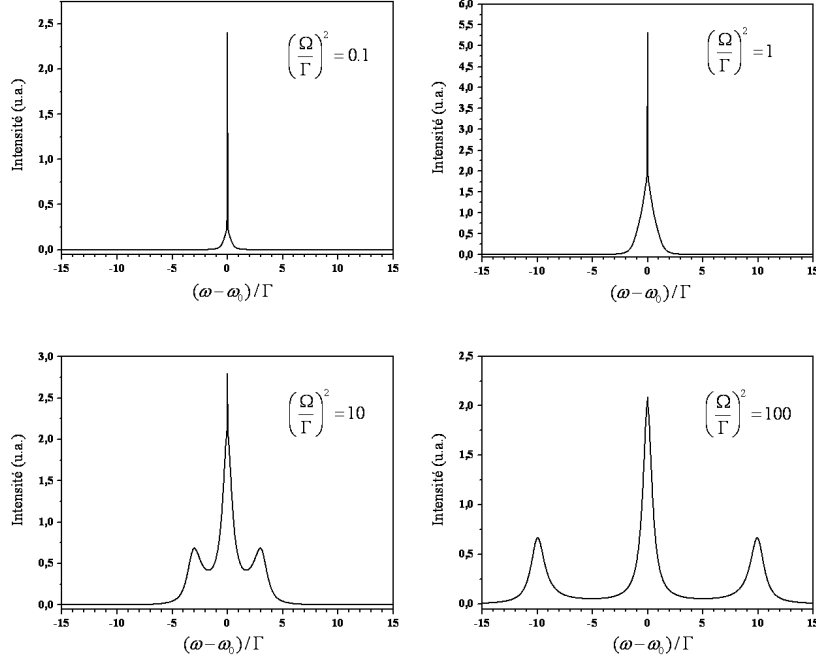


Figure 3.1: Resonance fluorescence spectra of a single QD at the radiative limit for different excitation powers corresponding to $\left(\frac{\Omega}{\Gamma}\right)^2 = \frac{s_0}{2}$. Figure extracted from Ref. [7].

3.1.2 Fourier transform spectroscopy

The micro-PL experimental setup presented in chapter 2 gives access to the spectrum of the radiative states of a single QD but its resolution, of about 100 μeV , does not allow to resolve the fine structure of these states which have typically widths of the order of a few to tens of μeV . We thus use a Fourier transform spectroscopy setup, which relies on a Michelson interferometer (see Fig. 3.2), in order to measure the resonance fluorescence spectrum of the neutral exciton, with a spectral resolution of 1.7 μeV given by the maximum reachable delay between the two arms of the interferometer (i.e. the maximum optical paths difference $\delta_{\text{max}} = 400$ mm, or the maximum temporal delay $\tau_{\text{max}} = 2.5$ ns). In such Michelson interferometer, the stationary electric field emitted by the QD can be expressed at the output of the interferometer as $E_{\text{out}} = \frac{1}{\sqrt{2}} [E(t) + E(t + \tau)]$, where the temporal delay $\tau = c/\delta$. The corresponding average intensity detected at the output of the interferometer then depends on the first-order correlation function at zero detuning, defined by equations (3.2) and (3.6), such as:

$$\langle I \rangle = I_0 \left[1 + \text{Re} \left(g^{(1)}(\tau) \right) \right] = I_0 \left[1 + |g^{(1)}(\tau)| \cos(\omega_0 t) \right] \quad (3.12)$$

In practice, the Fourier transform spectroscopy technique consists in the measurement of the contrast of the interferogram $C(\tau)$, which is directly linked to the first-order correlation function such as:

$$C(\tau) = \frac{I_{\text{max}}(\tau) - I_{\text{min}}(\tau)}{I_{\text{max}}(\tau) + I_{\text{min}}(\tau)} = |g^{(1)}(\tau)| \quad (3.13)$$

Therefore, due to the relation between the intensity spectrum and the first-order correlation function (see Eq. (3.8)), the measurement of the interferogram contrast allows us to measure

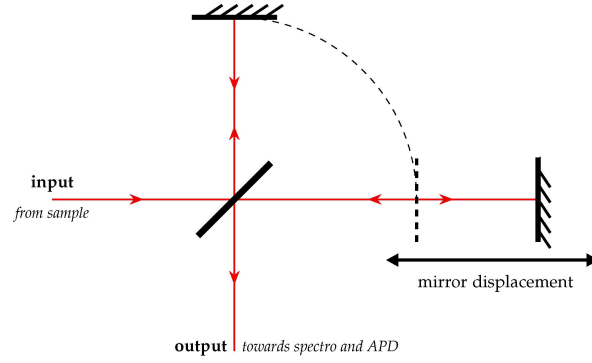


Figure 3.2: Scheme of the Michelson interferometer used for Fourier transform spectroscopy.

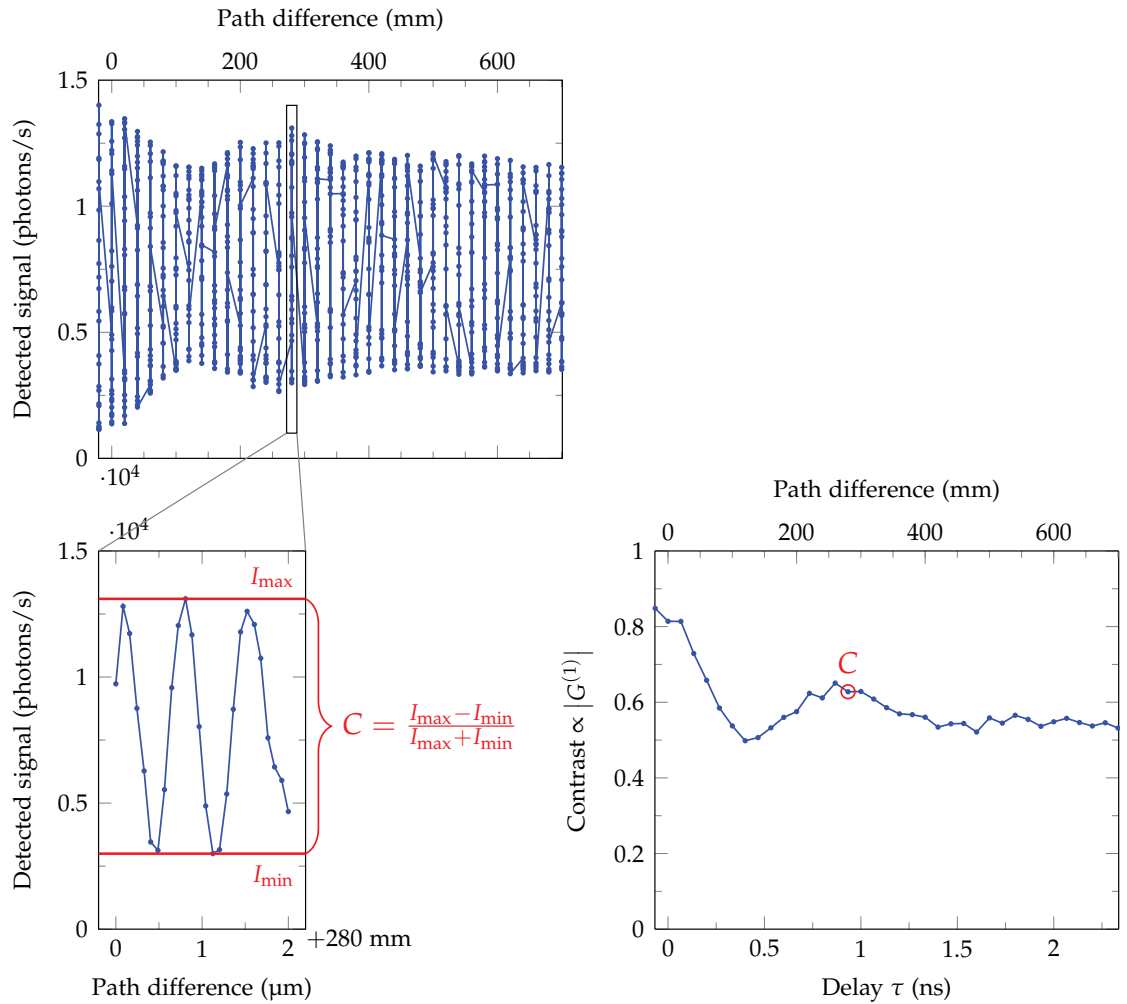


Figure 3.3: Principle of the measurement of the contrast of an interferogram with the Fourier transform spectroscopy setup. Figure extracted from Ref. [8].

the spectrum of the QD resonance fluorescence at zero detuning, $\mathcal{I}(\omega)$, following the relation:

$$\mathcal{I}(\omega) \propto \text{TF}^{-1} \left[g^{(1)}(\tau) \right] \propto \text{TF}^{-1} [C(\tau)] \quad (3.14)$$

where TF^{-1} stands for the inverse Fourier transform. The principle of the measurement is presented in figure 3.3. Each value of the contrast at a specific delay τ (lower right panel) is deduced from the interferograms measured within a fine displacement of the mirror (lower left panel) for several delays preliminary reached by a coarse fine displacement of the mirror (top panel).

3.1.3 Experimental results and discussion

In order to characterize the spectral properties of the resonance fluorescence of a single QD and investigate the different contributions in the signal, the measurement of the $g^{(1)}$ function is performed at various excitation powers. We can notice that in the resonance fluorescence spectrum measured in a PLE experiment, for a given detuning, the recorded intensity consists in the sum of the elastic and inelastic components. One expects the resonance fluorescence signal to be dominated by the elastic RRS at low incident power, and on the contrary by the inelastic component close to the QD saturation power. Contrary to this latter regime that has been well studied in single QDs [5, 6, 18, 22, 141–143] with the evidence for example of the Mollow triplet [22, 141–143], fewer research groups focused on the RRS regime in single QDs [24, 98, 120, 139, 140].

Figure 3.4 shows high-resolution measurements by Fourier transform spectroscopy of the exciton resonance fluorescence, for six excitation powers given by the saturation parameter $s_0 = \Omega^2 T_1 T_2$. These results reflect clearly the different light-matter coupling regimes between the excitation laser and the exciton transition. At high excitation power where the strong coupling regime takes place, we observe a non-monotonous decay exhibiting the Rabi oscillations associated to the Mollow triplet spectrum [97]. Then, a smooth transition to the RRS regime is observed when the excitation power is decreased. In particular, close to the QD saturation, the Rabi oscillations attenuate and the $g^{(1)}$ function exponentially decreases with mostly two characteristic times, the decoherence time T_2 and a longer time determined by the laser coherence time T_L . This latter contribution corresponds to the elastic RRS component. Our data are fitted (solid lines in Fig. 3.4) to the first-order correlation function $g^{(1)}(\tau)$ of the resonance fluorescence of a TLS (Eq. (3.6)). We stress that the theoretical fits must take into account an inherent contribution of a coherent background which is due to the parasitic scattering of the excitation laser. We assume in fact the presence of an elastic scatterer in the vicinity of the QD and close enough for its emission to be collected by the detection system. This scatterer is supposed to be elastic and linear with the excitation power, which means the parasitic scattering associated to it is perfectly coherent with the excitation laser and its intensity is proportional to the excitation power. Therefore, this parasitic scattering has a more complex role than only an additional background on the measurements due to its coherent nature with respect to the resonance fluorescence of the QD. One has thus to take into account the interferences between the electric field of the scattered laser and the electric field of the QD resonance fluorescence. The experimental data in figure 3.4 are then very well reproduced and the QD time characteristics extracted from the theoretical fits are $T_1 = 0.43 \pm 0.12$ ns and $T_2 = 0.54 \pm 0.10$ ns (T_1 and T_2 are joint fitting parameters which values are optimized through the entire set of measurements).

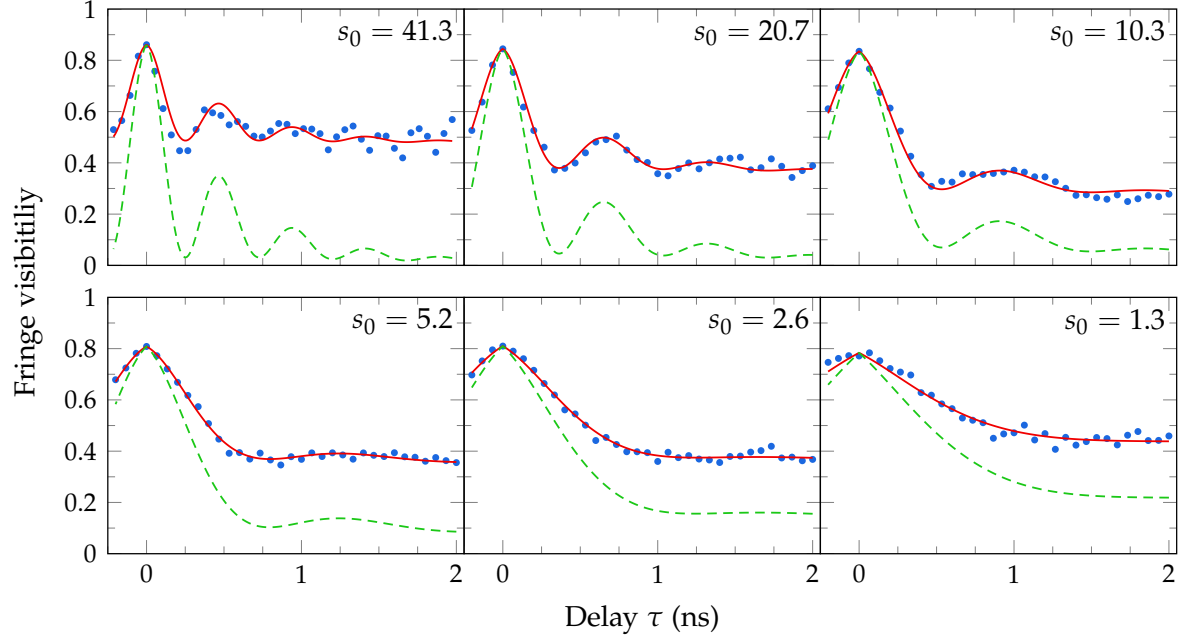


Figure 3.4: High-resolution Fourier transform spectroscopy of the resonance fluorescence of the exciton line for decreasing powers given by the saturation parameter $s_0 = \Omega^2 T_1 T_2$. The solid line is the theoretical fit of the first-order correlation function $g^{(1)}(\tau)$ given by equation (3.6) with $T_1 = 0.43 \pm 0.12$ ns and $T_2 = 0.54 \pm 0.10$ ns. The dashed curve corresponds to the theoretical curve with the same parameters but with zero parasitic background. Figure extracted from Ref. [8].

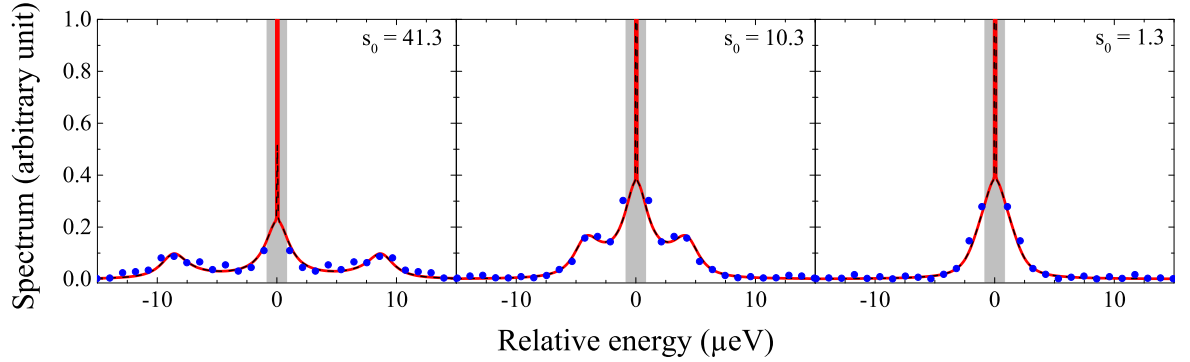


Figure 3.5: Resonance fluorescence spectrum calculated from the measurements of $g^{(1)}(\tau)$ (see Fig. 3.4). The radiative limit of width $1.8 \mu\text{eV}$ is schematized in grey and superimposed on each spectrum. The solid line is the theoretical fit of the spectrum, given by the Fourier transform of the theoretical fits presented in figure 3.4. The dashed curve corresponds to the theoretical curve with the same parameters but with zero parasitic background. Figure extracted from Ref. [8].

The Fourier transform of the $g^{(1)}$ measurements allows a direct comparison, in the spectral domain, of the different resonance fluorescence profiles. The results for three powers are presented in figure 3.5 where the top of the curves have been truncated in order to better resolve the components of lowest intensities. The radiative limit \hbar/T_1 of $1.8 \mu\text{eV}$ is also displayed on each spectrum as a guide of the eye of rectangular form. At high power, the

inelastic component consists in a well-developed Mollow triplet with side bands separated by $8.6 \mu\text{eV}$ from the central peak of width $2.3 \mu\text{eV}$. This Mollow triplet is the spectral counterpart of the Rabi oscillations at the Rabi pulsation Ω . The elastic scattering signal appears as a superimposed weak line, much narrower than the radiative limit. This central component is directly linked to the long time constant contribution in the measured $g^{(1)}$ function (see Fig. 3.4) and is governed by the parasitic laser scattering above saturation, whereas it is governed by the RRS on the TLS below saturation. In fact, upon reducing the excitation power, the Mollow triplet shrinks to a single Lorentzian line with sidebands, while the relative intensity of the narrow RRS peak increases and tends to overwhelm the resonance fluorescence spectrum. The dashed curve which corresponds to the theoretical resonance fluorescence spectrum without the contribution of the parasitic laser background clearly illustrates this behavior. Regarding the linewidth, in the specific RRS regime where the elastically scattered photons contribute to the spectrum, it appears that it can be much narrower than the one imposed by the radiative limit. It further confirms that the elastically scattered photons inherit the coherence of the excitation laser which is much longer than the decoherence time T_2 of the electronic system.

3.2 Photon statistics

3.2.1 Second-order correlation function of the resonance fluorescence

The second-order correlation function of the electric field of a light source is directly related to its statistical properties. The corresponding normalized function is defined in the stationary regime for a single light source as [96]:

$$g^{(2)}(\tau) = \frac{\langle E^{(-)}(t)E^{(-)}(t+\tau)E^{(+)}(t+\tau)E^{(+)}(t) \rangle}{\langle E^{(-)}(t)E^{(+)}(t) \rangle^2} = \frac{G^{(2)}(\tau)}{G^{(1)}(0)^2} \quad (3.15)$$

where $G^{(2)}(\tau) = \langle E^{(-)}(t)E^{(-)}(t+\tau)E^{(+)}(t+\tau)E^{(+)}(t) \rangle$ is the non-normalized second-order correlation function. From a general point of view, the statistical properties of a light source are defined regarding the value of $g^{(2)}(0)$: for $g^{(2)}(0) > g^{(2)}(\tau)$, the emission statistics is super-Poissonian and the photons are bunched (case of a classical thermal light); for $g^{(2)}(0) = g^{(2)}(\tau)$, the emission statistics is Poissonian and the photons are randomly spaced (case of a coherent laser light); for $g^{(2)}(0) < g^{(2)}(\tau)$, the emission statistics is sub-Poissonian and the photons are more equally spaced than a coherent laser field, i.e. the photons are anti-bunched (case of a quantum light source).

The second-order correlation function of a light source is often called the intensity auto-correlation function since it can also be written as a function of the intensity such as:

$$g^{(2)}(\tau) = \frac{\langle : I(t)I(t+\tau) : \rangle}{\langle I(t) \rangle^2} \quad (3.16)$$

where the notation " $:$ " refers to the normal order of the operators consisting in writing the creation operators on the left and the annihilation operators on the right. In the second quantification, the $g^{(2)}$ function can in fact be expressed as a function of the creation and annihilation operators such as:

$$g^{(2)}(\tau) = \frac{\langle a^\dagger(t)a^\dagger(t+\tau)a(t+\tau)a(t) \rangle}{\langle a^\dagger(t)a(t) \rangle^2} \quad (3.17)$$

In the particular case of a light source where the photons are emitted in a single mode of the electromagnetic field (i.e. a Fock state $|n\rangle$), the value at zero delay of the $g^{(2)}$ function depends on the number of photons such as [95]:

$$g^{(2)}(0) = \frac{n(n-1)}{n^2} \quad (3.18)$$

A perfect single photon source where the photons are emitted one by one in the same mode is then characterized by $g^{(2)}(0) = 0$, the value $g^{(2)}(0) = 1/2$ (for $n = 2$) being considered as an experimental limit below which a realistic source can be considered as a single photon source.

When considering the second-order correlation function of a resonantly-driven TLS, the non-normalized $G^{(2)}$ function depends on the dipolar operators such as:

$$\begin{aligned} G^{(2)}(\tau) &\propto \left\langle e^{+i\phi_{t_0 \rightarrow t}} S_+(t) e^{+i\phi_{t_0 \rightarrow t+\tau}} S_+(t+\tau) e^{-i\phi_{t_0 \rightarrow t+\tau}} S_-(t+\tau) e^{-i\phi_{t_0 \rightarrow t}} S_-(t) \right\rangle \\ &\propto \langle S_+(t) S_+(t+\tau) S_-(t+\tau) S_-(t) \rangle \end{aligned} \quad (3.19)$$

where, in the rotating frame approximation, the accumulated dephasing of the electric field emitted by the TLS is compensated. Therefore, the second-order correlation function remains unaffected and can be written as:

$$g^{(2)}(\tau) = \frac{\langle S_+(t) S_+(t+\tau) S_-(t+\tau) S_-(t) \rangle}{\langle S_+(t) S_-(t) \rangle^2} \quad (3.20)$$

By using the quantum regression theorem [54], one can show that the $g^{(2)}$ function, as regard to the TLS, is linked to the probability of emitting a photon at a time $t + \tau$, knowing that a photon has been previously emitted at a time t [144]. The $g^{(2)}$ function can then be calculated by evaluating the population of the excited state at $t + \tau$, knowing that the ground state is fully populated at t . Within the formalism of the matrix density, this statement induces that:

$$g^{(2)}(\tau) = \frac{\rho_{ee}(\tau)|_{\rho_{gg}(0)=1}}{\rho_{ee}^{(st)}} \quad (3.21)$$

The analytical solutions of the optical Bloch equations (1.22) then leads to [7, 96]:

$$g^{(2)}(\tau) = 1 - e^{-\eta\tau} \cdot \left(\cos(\nu\tau) + \frac{\eta}{\nu} \sin(\nu\tau) \right) \quad (3.22)$$

where we remind that:

$$\eta = \frac{1}{2} \left[\frac{1}{T_1} + \frac{1}{T_2} \right] \quad \text{and} \quad \nu = \sqrt{\Omega^2 - \frac{1}{4} \left[\frac{1}{T_1} - \frac{1}{T_2} \right]^2}$$

Contrarily to the first-order correlation function, the relaxation times T_1 and T_2 play a symmetrical role in the $g^{(2)}$ function, and it does not depend on the laser coherence time T_L . However, the $g^{(2)}$ function of a resonantly-driven QD is still fundamentally different from the non-resonant excitation case where it depends only on T_1 .

To illustrate the expected statistical properties of the resonance fluorescence of a single QD, the figure 3.6 presents the theoretical second-order correlation function calculated from equations (3.22) at the radiative limit (i.e. $\Gamma = \frac{1}{T_1} = \frac{2}{T_2}$), for different excitation powers given by the saturation parameter s_0 ($(\frac{\Omega}{\Gamma})^2 = \frac{s_0}{2}$ in the figure). The signature of an ideal

single photon source is observed through the perfect antibunching dip at zero delay, i.e. $g^{(2)}(0) = 0$, for each excitation power. It shows that a resonantly excited single QD at the radiative limit constitutes an ideal single photon source in both elastic ($s_0 \ll 1$) and inelastic regimes ($s_0 \gg 1$). In particular, in the RRS regime, the width of the antibunching dip depends on T_1 (and T_2 when the radiative limit is not reached) and not anymore on the excitation power. However, above saturation, the Rabi oscillations, which characterize the strong coupling regime between the laser and the TLS, appear in the $g^{(2)}$ function around $\tau = 0$. This effect induces a strong narrowing of the antibunching dip due to the power dependence of its width but the value of $g^{(2)}(0)$ is not modified.

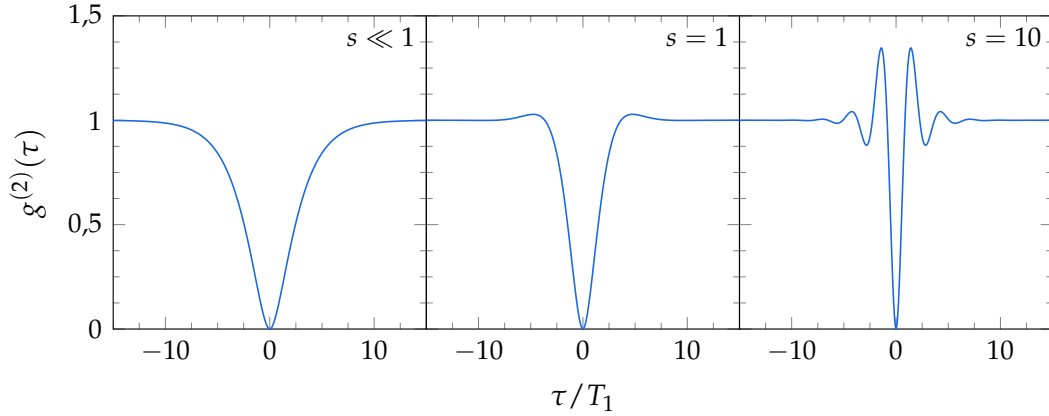


Figure 3.6: Second-order correlation function $g^{(2)}(\tau)$ of the resonance fluorescence of a single QD at the radiative limit for different excitation powers corresponding to $(\frac{\Omega}{\Gamma})^2 = \frac{s_0}{2}$. Figure extracted from Ref. [8].

3.2.2 Hanbury Brown and Twiss experiment

The intensity auto-correlation function is measured in an HBT experiment [145–147], which relies on an intensity interferometer where the correlations between two photodetectors are measured at the two outputs of the beamsplitter where the interferences occur (see figure 3.7). The correlation module measures the probability of a joint photodetection on each of the two detectors, or in other word the probability of detecting two photons separated by a temporal delay τ . Following the theory of the photodetections [54, 96], the corresponding detection rate can be written as:

$$w_2(t, t + \tau) = \sum_f \left| \left\langle f \left| E^{(+)}(t + \tau) E^{(+)}(t) \right| i \right\rangle \right|^2 \quad (3.23)$$

where $|i\rangle$ and $|f\rangle$ are the initial and final states of the electric field. By using the closing relation on the final states, then by summing over all the possible initial states of the electric field (which are known with a probability P_i), and finally by considering the density operator

of the electric field $\rho = \sum P_i |i\rangle \langle i|$, the detection rate can be written as:

$$\begin{aligned} w_2(t, t + \tau) &= \text{Tr} \left[\rho E^{(-)}(t) E^{(-)}(t + \tau) E^{(+)}(t + \tau) E^{(+)}(t) \right] \\ &= \left\langle E^{(-)}(t) E^{(-)}(t + \tau) E^{(+)}(t + \tau) E^{(+)}(t) \right\rangle \\ &= G^{(2)}(\tau) \end{aligned} \quad (3.24)$$

The detection rate measured in an HBT interferometer is then directly related to the non-normalized second-order correlation function. Then, because the electric fields between two detections separated by a long time delay are not correlated anymore, $G^{(2)}(\tau \rightarrow \infty) = (G^{(1)}(0))^2$ and the $g^{(2)}$ function is obtained by normalizing the results by the correlation rate at long time delay.

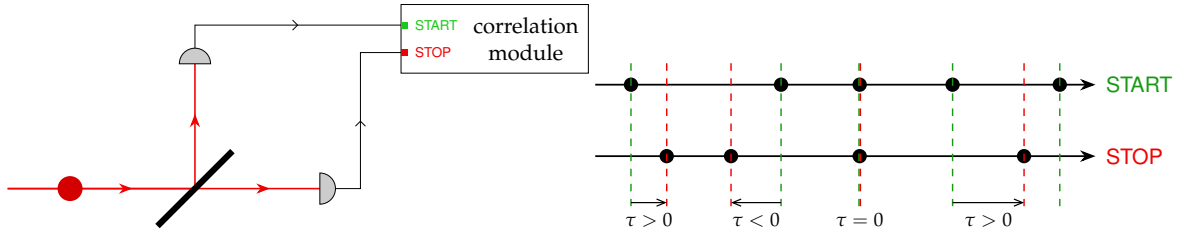


Figure 3.7: Left panel: scheme of a Hanbury Brown and Twiss (HBT) interferometer. Right panel: principle of the correlation module used to measure the probability of detecting two photons separated by a delay τ on the detectors.

3.2.3 Experimental results and discussion

The measurement of the second-order correlation function $g^{(2)}(\tau)$ of the resonance fluorescence as a function of the excitation power allows us to study the photon statistics of the QD emission in both regimes of inelastic and elastic scattering. In order to minimize the inherent contribution of the coherent background due to the parasitic scattering of the excitation laser, this study is first performed at excitation powers corresponding to $s_0 < 10$. The results of the normalized intensity auto-correlation measurements are presented in figure 3.8 along with the Instrument Response Function (IRF, inset) of the HBT setup. One can observe a dip at zero time delay for every excitation powers which is the signature that the QD emits antibunched photons. In particular, for $s_0 \leq 2$, the antibunching dip is characterized by a value of $g^{(2)}(0) < 0.5$, reflecting the single photon emission of the QD. At higher excitation powers such as $s_0 > 2$, the QD undergoes Rabi oscillations which can be seen through the dip sidebands with $g^{(2)}$ values higher than one. This phenomenon induces a narrowing of the antibunching dips [22] and therefore a strong reduction of their visibility with $g^{(2)}(0) \geq 0.5$ for the given IRF.

In order to present a comprehensive study of the photon statistics of the QD resonance fluorescence, the measurement of the intensity auto-correlation function is also done for much higher excitation powers ($s_0 > 10$). As shown in figure 3.9, a peculiar photon bunching at zero time delay corresponding to $g^{(2)}(0) > 0$ appears when the contribution of the coherent background of the parasitic scattered laser is not negligible anymore (for $s > 27$). Since only the resonance fluorescence and the parasitic laser background with a sub-poissonian (i.e. $g^{(2)}(0) < 1$) and poissonian emission statistics (i.e. $g^{(2)}(0) = 1$), respectively, contribute to

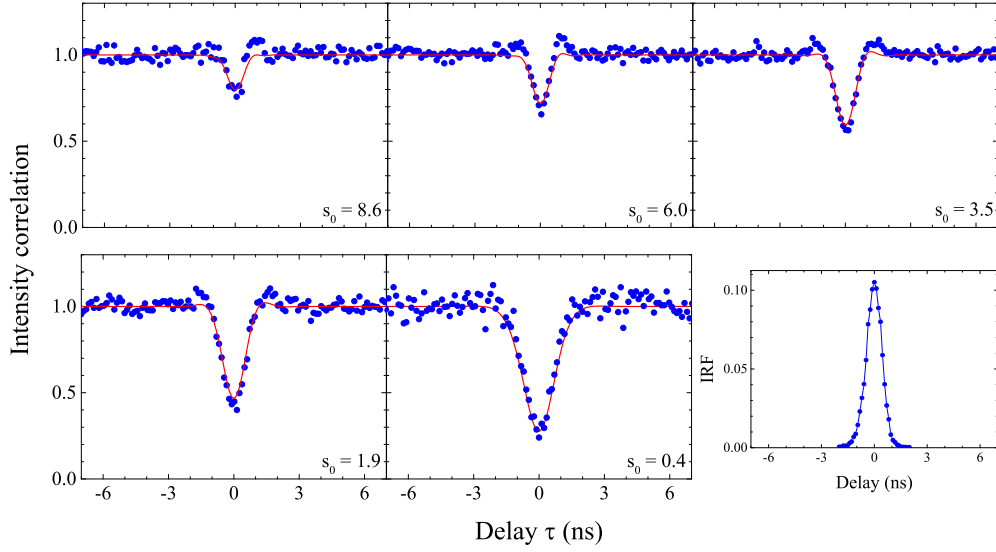


Figure 3.8: Intensity autocorrelation measurements of the resonance fluorescence for decreasing powers given by the saturation parameter $s_0 = \Omega^2 T_1 T_2$. The data are fitted by the theoretical second-order correlation function $g^{(2)}(\tau)$ given by equation (3.22), convoluted by the system time response, with $T_1 = 0.43 \pm 0.12$ ns and $T_2 = 0.54 \pm 0.10$ ns. Inset: Instrument Response Function (IRF) of the Hanbury Brown and Twiss (HBT) setup measured with a picosecond pulsed Ti:Sa laser. The FWHM is equal to 1 ns. Figures extracted from Ref. [8].

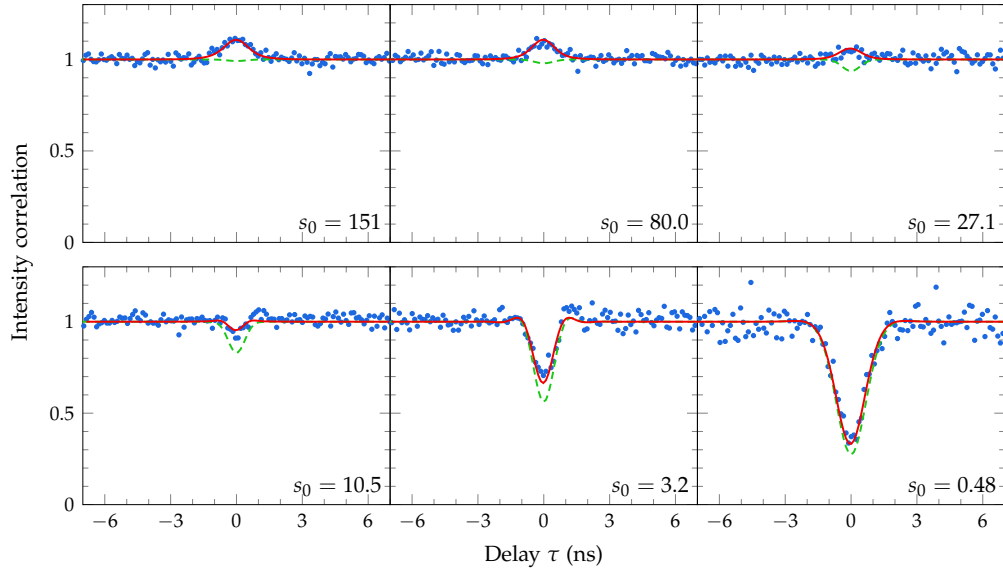


Figure 3.9: Intensity autocorrelation measurements of the resonance fluorescence for decreasing powers given by the saturation parameter $s_0 = \Omega^2 T_1 T_2$. The solid line is the theoretical fit of the second-order correlation function $g^{(2)}(\tau)$ where the parasitic coherent background of the scattered laser is taken into account, with $T_1 = 0.43 \pm 0.12$ ns and $T_2 = 0.54 \pm 0.10$ ns. The dashed curve corresponds to the theoretical curve with the same parameters but with zero parasitic background. Figure extracted from Ref. [8].

the total measured signal, the sum of these two contributions cannot explain by itself the observed photon bunching. As already explained in the previous section, due to the coherent nature of the parasitic laser background, one has to take into account the interferences between the electric field of the scattered laser and the electric field of the QD resonance fluorescence in order to fit the whole set of data. In fact, as shown by the dashed curve in figure 3.9, the photon bunching phenomenon at high power cannot be well fitted when the parasitic laser background is not taken into account. However, even if the effect of the parasitic laser still contributes to the value of $g^{(2)}$ at zero time delay, it does not affect the width of the antibunching dip which allows us to determine the time constants of the system T_1 and T_2 .

These results show that contrary to the case of non-resonant excitation where the second-order correlation function is only governed by the radiative lifetime T_1 and the pumping rate, the photon statistics under resonant excitation is also governed by the decoherence time T_2 . Furthermore, for the specific regime of low excitation powers where $s_0 \ll 1$, the second-order correlation function does not depend anymore on the excitation power (i.e. on Ω^2) and follows the simple dependence on T_1 and T_2 given by:

$$g^{(2)}(\tau) = 1 - \frac{1}{T_2 - T_1} \left(T_2 e^{-\tau/T_2} - T_1 e^{-\tau/T_1} \right) \quad (3.25)$$

In that case, the pronounced dip at zero time delay ($g^{(2)}(0) = 0.3$), which is only limited by the system time response, shows that our system is an efficient single photon source, as expected in the regime where the resonance fluorescence spectrum is dominated by the RRS component [22, 96].

3.3 The resonant Rayleigh scattering regime

In this chapter, we have seen that the resonant excitation of a single QD in the specific RRS regime leads to this very peculiar situation where the first-order correlation function of the radiated electric field has the classical character of the excitation laser, whereas the second-order correlation function has a quantum nature inherited from the light-matter interaction at the scale of a single QD [148, 149]. In fact, when the resonance fluorescence of a single QD is dominated by the coherent laser light scattering, anti-bunching is observed together with a narrow emission spectrum with a smaller linewidth than the one imposed by the radiative limit. This implies that single QDs can produce single photons with a decoherence time that is not limited anymore by the QD electronic properties. As a matter of fact, this system represents an original type of quantum device which emits what we have defined "ultra-coherent" single photons [24], with a coherence time controlled by the excitation laser and the photon statistics by the QD electronic properties. From the practical point of view, we stress that despite a resulting overall collection efficiency of our experimental setup of 0.25 %, 10 000 counts/s were typically detected on each APD when working in the RRS regime. Such detection levels are comparable to the emission rates measured for QD-based single photon sources where the photon extraction and collection efficiencies are optimized thanks to quite complex structures [150].

Nevertheless, an important question is the existence of an upper limit for the RRS fraction and the corresponding physical parameters conditioning it. From the theoretical study of the resonance fluorescence of a TLS presented in chapter 1 (section 1.3.2) and the equations (1.24) and (1.30), the ratio between the RRS contribution $\langle I_{\text{el}} \rangle$ and the total resonance fluorescence

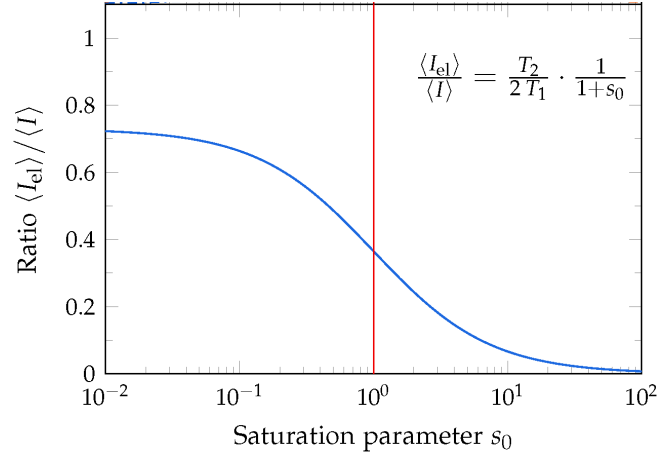


Figure 3.10: Ratio between the elastic component and the total resonance fluorescence as a function of the excitation power given by the saturation parameter s_0 . This ratio is calculated with the time constants extracted from the measurements of the $g^{(1)}$ function, $T_1 = 0.43 \pm 0.12$ ns and $T_2 = 0.54 \pm 0.10$ ns. Figure extracted from Ref. [8].

signal $\langle I \rangle$ is calculated in the stationary regime and results in:

$$\frac{\langle I_{\text{el}} \rangle}{\langle I \rangle} = \frac{T_2}{2T_1} \cdot \frac{1}{1+s_0} = \frac{T_2}{2T_1} \cdot \frac{1}{1+\Omega^2 T_1 T_2} \quad (3.26)$$

In the case of an ideal TLS at the radiative limit, $T_2 = 2T_1$ and the resonance fluorescence signal is completely dominated by the RRS for excitation powers such as $s_0 \ll 1$. On the contrary, as soon as pure dephasing appears, leading to $T_2 < 2T_1$, the highest fraction of RRS in the resonance fluorescence signal is given by $T_2/2T_1$. We conclude that in our system where $T_2 = 1.46 T_1$, the RRS fraction cannot intrinsically exceed 73% of the resonance fluorescence signal. These properties are illustrated by the theoretical figure 3.10 which displays the ratio between the elastic component and the total intensity (i.e. the sum of the elastic and inelastic contributions) as a function of the excitation power given by the saturation parameter s_0 . The ratio $\langle I_{\text{el}} \rangle / \langle I \rangle$ is calculated with the time constants extracted from the previous measurements, $T_1 = 0.43 \pm 0.12$ ns and $T_2 = 0.54 \pm 0.10$ ns. This study confirms that the elastic scattering dominates the resonance fluorescence signal below the saturation power of the TLS, but it also shows that the intensity of the RRS component is intrinsically limited by the ratio $T_2/2T_1$. Therefore, even if the photons emitted in the RRS inherit the coherence of the excitation laser, their proportion will still be limited by the QD decoherence time T_2 through the pure dephasing processes, unless the radiative limit $T_2 = 2T_1$ is reached. This statement is supported by a recent experimental study of the group of B. D. Gerardot [101] which proves that a dephasing process such as the one induced by the fluctuating nuclear spins drastically affects the ratio of the RRS component with respect to the total emission. However, this ratio reaches almost 100% when controlling the fluctuating spins reservoir by applying a modest magnetic field in the growth direction (< 1 T). A closely related study done in the group of R. Warburton [151] also showed that by controlling the nuclear spin noise by a magnetic field, the radiative limit can be reached, leading to Fourier transform limited exciton lines.

3.4 Conclusion

In this chapter, the specificity of the resonance fluorescence of single QDs has been investigated by studying the power dependence of the first-order and second-order correlation functions, which give access to the coherence and the statistic properties of the emitted photons, respectively. We have shown that the resonance fluorescence signal consists in the superposition of an inelastic (or incoherent) component which spectrum exhibits the so-called Mollow triplet with linewidths governed by the coherence of the electronic system, and an elastic (or coherent) component, the RRS, which spectrum is similar to the excitation laser. Both emission contributions exhibit a sub-poissonian statistics which demonstrate that resonantly-driven single QDs constitute single photon sources at all excitation powers. In particular, we have demonstrated that single QDs operated at low power regime (i.e. below the saturation of the TLS), in the rarely studied RRS regime, are original "ultra-coherent" single photon sources where the coherence time of the emitted photons largely exceeds the coherence imposed by the QD electronic properties since it is tailored by the coherence of the excitation laser ($\sim 1 \mu\text{s}$). This implies that single QDs can produce single photons with a coherence time that is not limited anymore by the radiative limit, even though the pure dephasing still needs to be reduced in order to increase the amount of elastically scattered photons. This ultra-coherent single photon source promises high degrees of indistinguishability of the emitted photons which is a crucial requirement for quantum information applications.

Chapter 4

Photon indistinguishability in the resonant Rayleigh scattering regime

In this chapter, we present an experimental study of the indistinguishability of the photons emitted by a single quantum dot (QD) under cw resonant excitation. Single semiconductor QDs under resonant excitation [18, 101, 152, 153], along with other systems under extensive study including atoms [154], molecules [155, 156], trapped ions [157], and colored centers in diamond [158], are in fact promising candidates for sources of single indistinguishable photons. However, photon indistinguishability is either limited by the QD dynamics under pulsed excitation [159], or by the detectors' temporal resolution under cw excitation [160–162]. Here, we focus on the photon indistinguishability of the ultra-coherent single photon source presented in chapter 3 where the scattered photons inherit the coherence time of the excitation laser T_L , which can be much longer than T_2 and the detectors' time response T_R , while still exhibiting sub-Poissonian statistics. Considering the Mandel's notion that coherence equals indistinguishability [163], the resonant Rayleigh scattering (RRS) regime constitutes thus the ideal ground for the generation of highly indistinguishable photons. We first describe the Hong-Ou-Mandel (HOM) two-photon interference setup that was used and we introduce the intensity correlation function that was experimentally investigated as a function of the power and the coherence time of the excitation laser. After detailing the main fundamental differences between an HOM experiment performed under pulsed or cw excitation, we define a new figure of merit, the coalescence time window (CTW), which allows taking into account the nature and the operation mode of a single photon source when characterizing the indistinguishability of the emitted photons. The power dependence of this new quantity is measured in order to characterize the photon indistinguishability of the QD resonance fluorescence in the elastic and inelastic regimes and its dependence as a function of the laser coherence time is also investigated in the RRS regime where the photon coherence time is governed by the laser.

4.1 Two-photon interference experiment

4.1.1 Hong-Ou-Mandel interferometer

The photon indistinguishability of a single photon source is investigated using the coalescence phenomenon where two photons with similar spectral, spatial and polarization properties bunch when arriving simultaneously on two opposite sides of a beamsplitter. This effect

was first experimentally demonstrated by Hong, Ou and Mandel [164] where the photons from two parametric sources were combined at the two inputs of a beamsplitter and the coalescence was detected through a drop of the coincidence rate at the outputs when adjusting precisely the position of the beamsplitter — this is the so-called HOM dip. In the case of a single photon source, this experiment can be reproduced with the use of a strongly unbalanced Mach-Zehnder interferometer where the delay between the two arms is longer than the coherence time of the light source in order to ensure that the incident fields on the beamsplitter remain independent for small time delays compared to the interferometer delay [162].

As illustrated in figure 4.1, the QD resonance fluorescence is sent to a Mach-Zehnder interferometer which is used as an HOM interferometer. In order to prevent fictitious anti-coincidences from one-photon interference when performing two-photon interference in the RRS regime, the paths difference in the HOM interferometer must be larger than the photon coherence time, and thus larger than the laser coherence time T_L . This is ensured using optical fibers to reach an interferometer delay $\Delta\tau = 43.5$ ns. Moreover, a half-wave plate in one of

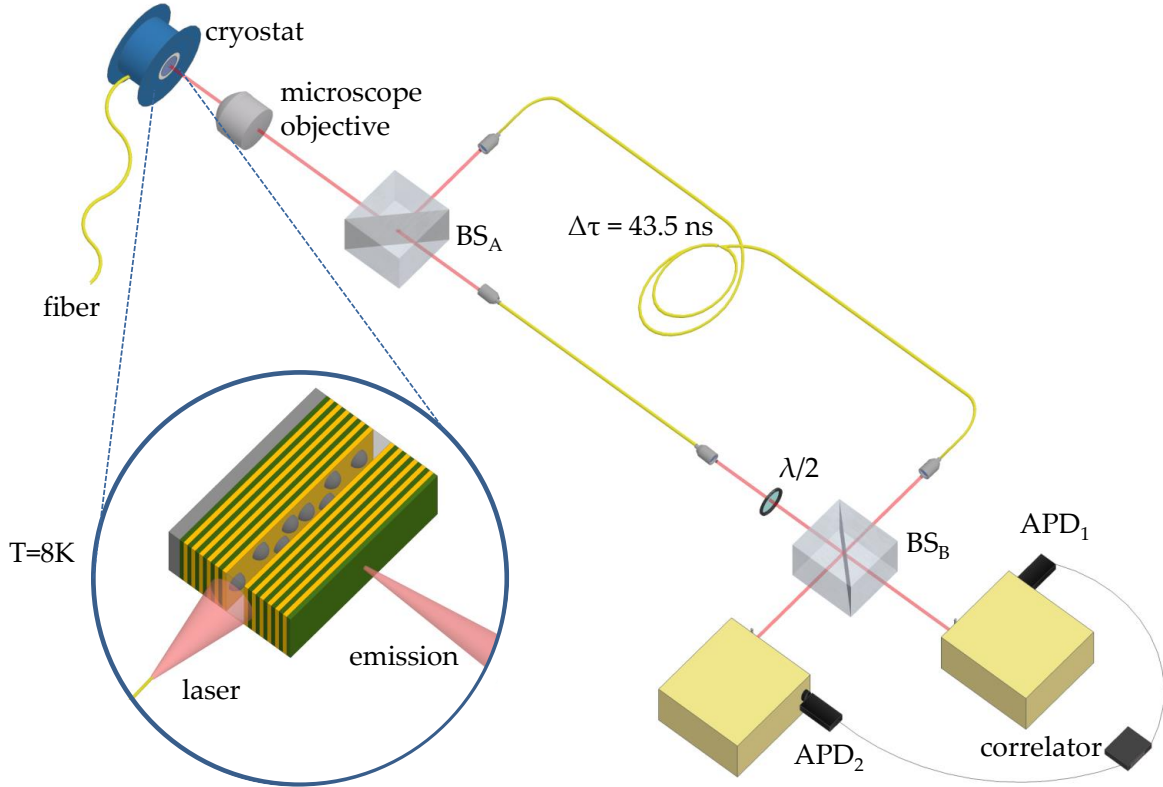


Figure 4.1: Unbalanced Mach-Zehnder interferometer for Hong-Ou-Mandel (HOM) two-photon interference measurements. The QD emission is split by a first beam splitter (BS_A) in two paths of different lengths and recombined at a second one (BS_B). Single mode polarization maintaining fibers ensure high spatial overlap at BS_B and a half-wave plate $\lambda/2$ controls the mutual polarization between the two interferometer arms. Photodetection is monitored by two avalanche photodiodes (APD) placed at the BS_B outputs, combined with spectrometers for spectral filtering and a correlator for the intensity correlation function measurements. Inset: sketch of the orthogonal excitation-detection geometry where a QD is excited via a fiber positioned at the edge of the sample while its emission is collected by a microscope objective in an orthogonal configuration (see chapter 2 for more details). Figure extracted from Ref. [25].

the arms is used to change the polarization. This allows us to make the polarization parallel or orthogonal between the two arms, thus establishing or destroying the interferences at the output of the interferometer, respectively. Photodetection performed at the two outputs of the second beamsplitter allows us to measure, in each polarization configuration, the intensity correlation function $g^{(2X)}(\tau)$, where τ is the delay between two consecutive detections on the APDs.

4.1.2 Theoretical intensity correlation function

In order to calculate the theoretical intensity correlation function that is measured in such an experimental setup¹, one has first to consider the electric field detected at times t_1 and t_2 on each APD at positions r_1 and r_2 , as a function of the incident electric field emitted at time t_0 by the source at position r_0 . This implies taking into account the amplitude reflection and transmission coefficients of the two beamsplitters ($r_{A(B)}$ and $t_{A(B)}$ for $BS_{A(B)}$) when applying the input/output relations at each beamsplitters [165], the propagation times between each optical element, and the relative polarization of the light between the two arms² (in the general case, the polarization in the short arm is taken along the x axis while the polarization in the long arm is rotated by an angle ϕ with respect to the x axis). When considering all the possible polarization configurations, the non-normalized intensity correlation function is written as:

$$\begin{aligned} G^{(2X)}(\tau) &= \sum_{i,j=\{x,y\}} \left\langle E_i^{(-)}(r_1, t_1) E_j^{(-)}(r_2, t_2) E_j^{(+)}(r_2, t_2) E_i^{(+)}(r_1, t_1) \right\rangle \\ &= \sum_{i,j=\{x,y\}} \left\langle E_i^{(-)}(r_1, t) E_j^{(-)}(r_2, t + \tau) E_j^{(+)}(r_2, t + \tau) E_i^{(+)}(r_1, t) \right\rangle \end{aligned} \quad (4.1)$$

where t ($t + \tau$) is the time delay between the detection time t_1 (t_2) and the propagation time of an emitted photon through the short arm of the interferometer (τ is thus the time delay between the propagation times from the BS_B outputs to each APD), and $E^{(\pm)}$ are the electric field operators such as:

$$\vec{E}^{(+)}(r_1, t_1) = t_A t_B E^{(+)}(r_0, t) \vec{e}_x - r_A r_B E^{(+)}(r_0, t - \Delta\tau) (\cos \phi \vec{e}_x + \sin \phi \vec{e}_y) \quad (4.2a)$$

$$\vec{E}^{(+)}(r_2, t_2) = i t_A r_B E^{(+)}(r_0, t + \tau) \vec{e}_x + i r_A t_B E^{(+)}(r_0, t + \tau - \Delta\tau) (\cos \phi \vec{e}_x + \sin \phi \vec{e}_y) \quad (4.2b)$$

A set of 16 terms is obtained after injecting the components E_x and E_y of the electric field in equation (4.1). More specifically, the terms corresponding to the two-photon interferences are asymmetrical correlators where at least three different times appear. For a strong unbalanced HOM interferometer, the electric field operators at a time delayed by $\Delta\tau$ are independent and can be separated so that most of these asymmetrical correlators are equal to zero. Therefore, the only asymmetrical correlator related to the two-photon interference phenomenon (along with its complex conjugate) is:

$$\begin{aligned} &\left\langle E^{(-)}(t) E^{(-)}(t + \tau - \Delta\tau) E^{(+)}(t + \tau) E^{(+)}(t - \Delta\tau) \right\rangle \\ &= \left\langle E^{(-)}(t) E^{(+)}(t + \tau) \right\rangle \left\langle E^{(+)}(t - \Delta\tau) E^{(-)}(t + \tau - \Delta\tau) \right\rangle = \left| G^{(1)}(\tau) \right|^2 \end{aligned} \quad (4.3)$$

¹A detailed calculation of the intensity correlation function $g^{(2X)}(\tau)$ can be found in Ref. [8].

²The method used to take into account the polarization in this calculation is similar to the one used in Ref. [166].

The normalization of the $G^{(2X)}$ function (where $G^{(1)}(\pm\Delta\tau) = 0$) leads to the following intensity correlation function:

$$g^{(2X)}(\tau) = \frac{1}{D} \left[R_B T_B (T_A^2 + R_A^2) g^{(2)}(\tau) + R_A T_A T_B^2 g^{(2)}(\tau - \Delta\tau) + R_A T_A R_B^2 g^{(2)}(\tau + \Delta\tau) - 2R_A T_A R_B T_B \cos^2 \phi |g^{(1)}(\tau)|^2 \right] \quad (4.4)$$

where $D = R_A T_A (R_B^2 + T_B^2) + R_B T_B (R_A^2 + T_A^2)$ is a normalizing factor, $R_{A(B)}$ and $T_{A(B)}$ are the reflection and transmission intensity coefficients of the beam splitters $BS_{A(B)}$ respectively, and ϕ is the angle between the polarizations in each arm of the interferometer. The related coefficient $\cos^2 \phi$, which reflects the polarization mismatch between the two arms of the interferometer, can be generalized and replaced by a more general experimental parameter V_0 which takes into account all the experimental imperfections that destroy the overlap in space or polarization of the two beams at BS_B .

The theoretical $g^{(2X)}(\tau)$ function that is used to fit the experimental data is then written as:

$$g^{(2X)}(\tau) = \frac{1}{D} \left[R_B T_B (T_A^2 + R_A^2) g^{(2)}(\tau) + R_A T_A T_B^2 g^{(2)}(\tau - \Delta\tau) + R_A T_A R_B^2 g^{(2)}(\tau + \Delta\tau) - 2R_A T_A R_B T_B V_0 |g^{(1)}(\tau)|^2 \right] \quad (4.5)$$

In the case of ideal experimental conditions where $R_{A,B} = T_{A,B} = 1/2$ and $V_0 = 1$ and 0 in the parallel and orthogonal polarization configurations, respectively, the intensity correlation functions $g_{\parallel}^{(2X)}$ and $g_{\perp}^{(2X)}$ in the parallel and orthogonal polarization configurations, respectively, get simplified to:

$$g_{\parallel}^{(2X)}(\tau) = \overbrace{\frac{1}{4}g^{(2)}(\tau + \Delta\tau)}^{\text{B1}} + \overbrace{\frac{1}{4}g^{(2)}(\tau - \Delta\tau)}^{\text{B2}} + \overbrace{\frac{1}{2}g^{(2)}(\tau) - \frac{1}{2}|g^{(1)}(\tau)|^2}^{\text{A}} \quad (4.6a)$$

$$g_{\perp}^{(2X)}(\tau) = \frac{1}{4}g^{(2)}(\tau + \Delta\tau) + \frac{1}{4}g^{(2)}(\tau - \Delta\tau) + \frac{1}{2}g^{(2)}(\tau) \quad (4.6b)$$

Both equations (4.6a) and (4.6b) depend on the second-order correlation function $g^{(2)}(\tau)$, which is related to the photon emission statistics of the source, while the first-order correlation function $g^{(1)}(\tau)$, which is linked to the coherence of the two-level system (TLS), appears only in equation (4.6a) as part of the two-photon interference term. This already highlights that coherence and coalescence are dual notions [163, 167], as further investigated in the next section. Moreover, because both $g^{(1)}$ and $g^{(2)}$ depend on the QD time constants T_1 and T_2 , while the laser coherence time T_L appears in $g^{(1)}$ (see chapters 1 and 3), we expect that the dynamics of $g_{\parallel}^{(2X)}$ and $g_{\perp}^{(2X)}$ are significantly different from the non-resonant case [160, 161]. This statement will be further experimentally investigated in the next section, but this specific dynamics can already be observed in figure 4.2 which displays the theoretical functions $g_{\parallel}^{(2X)}(\tau)$ and $g_{\perp}^{(2X)}(\tau)$ in the case of a resonantly excited QD with $T_2 = 2T_1$, in the RRS regime (i.e. $s_0 \ll 1$). Here, the laser coherence time is set to $T_L = 80T_1$ and the interferometer delay to $\Delta\tau = 200T_1$.

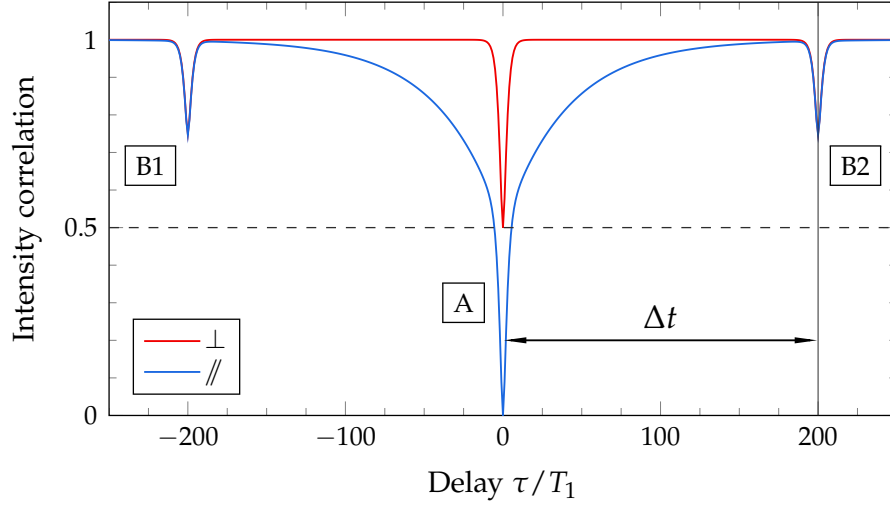


Figure 4.2: Theoretical functions $g_{//}^{(2X)}(\tau)$ (blue) and $g_{\perp}^{(2X)}(\tau)$ (red) for a resonantly-driven QD in the resonant Rayleigh scattering regime (i.e. $s_0 \ll 1$), with $T_2 = 2T_1$, $T_L = 80T_1$ and $\Delta\tau = 200T_1$. Δt on the figure corresponds to $\Delta\tau$ in the text. Figure extracted from Ref. [8].

On the one hand, the theoretical function $g_{\perp}^{(2X)}$, which only depends on the $g^{(2)}$ function (see Eq. (4.6b)), presents three antibunching dips at $\tau = -\Delta\tau$, $\tau = 0$ and $\tau = +\Delta\tau$, labeled B1, A and B2, respectively, with widths governed by both T_1 and T_2 under resonant excitation. The central dip corresponds to the case where two photons propagated through the same paths of the interferometer (short-short or long-long), similarly to a Hanbury Brown and Twiss (HBT) experiment, whereas the side dips corresponds to the case where two photons propagated through two different paths (long-short for dip B1 and short-long for dip B2). In case of an ideal single photon source, the dips values are given by the paths probabilities, and $g_{\perp}^{(2X)}(\pm\Delta\tau) = 1/4$ and $g_{\perp}^{(2X)}(0) = 1/2$ for perfectly equilibrated beamsplitters.

On the other hand, the theoretical function $g_{//}^{(2X)}$, which not only depends on $g^{(2)}$ but also on $g^{(1)}$ (see Eq. (4.6a)), shows first the same antibunching side dips related to the single photon emission property as in the orthogonal configuration. Then, a totally different dip at $\tau = 0$ can be observed, with $g_{//}^{(2X)}(0) = 0$ and a much larger width, due to the interferences between two photons impinging, at the same time, each input of the beamsplitter BS_B . In particular, this additional component in this HOM dip presents a time dependence of $1 - e^{-2\tau/T_L}$, which is directly linked to the first-order correlation function of a resonantly-driven TLS at the radiative limit in the RRS regime, $g^{(1)}(\tau) \propto e^{-\tau/T_L}$ (see chapter 3, Eq. (3.6)). Moreover, we stress that the value $g_{//}^{(2X)}(0) < 0.5$ ($g_{//}^{(2X)}(0) = 0$ for the ideal case) can only be reached for a source of single indistinguishable photons. In fact, the same study with a laser would lead to a value $g_{//}^{(2X)}(0) \geq 0.5$ ($g_{//}^{(2X)}(0) = 0.5$ for an ideal interferometer).

In the following, the visibility of the two-photon interference experiment that is commonly defined as [18, 152, 160]:

$$V_{\text{HOM}}(\tau) = \frac{g_{\perp}^{(2X)}(\tau) - g_{//}^{(2X)}(\tau)}{g_{\perp}^{(2X)}(\tau)} \quad (4.7)$$

is also studied. Within this definition, the HOM visibility, V_{HOM} , allows evaluating the contribution of the two-photon interferences in the HOM dip, knowing that the source emits antibunched photons. That is why this function is commonly used to estimate the degree of

photon indistinguishability of a single photon source. An example of the theoretical visibility calculated for the resonantly excited QD with $T_2 = 2T_1$, in the RRS regime is presented in figure 4.3. Here, for $\tau \gtrsim 10T_1$, the HOM visibility shows the long time dependence of time constant $T_L/2$ related to the two-photon interference contribution, along with the narrow component related to the emission statistics, for $\tau < 10T_1$. Moreover, in the ideal case of a radiatively-limited QD and a perfect interferometer, a maximum contrast is reached at zero delay and $V_{\text{HOM}}(0) = 1$.

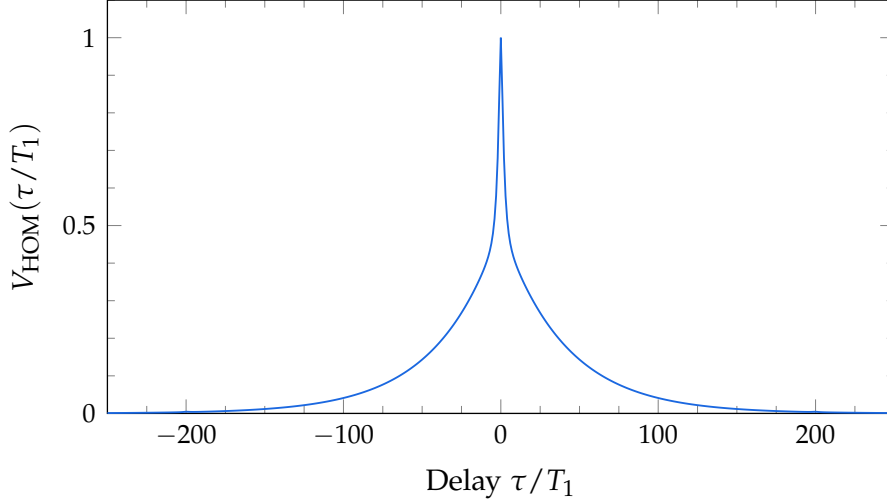


Figure 4.3: Theoretical HOM visibility $V_{\text{HOM}}(\tau)$ for a resonantly-driven QD in the resonant Rayleigh scattering regime (i.e. $s_0 \ll 1$), with $T_2 = 2T_1$, $T_L = 80T_1$ and $\Delta\tau = 200T_1$. Figure extracted from Ref. [8].

4.2 Photon indistinguishability under resonant excitation

The indistinguishability of the photons emitted by a single QD under cw resonant excitation is studied as a function of the excitation power in order to assess both elastic and inelastic scattering regimes. Figure 4.4 presents intensity correlation measurements realized with the HOM setup with parallel and orthogonal polarization configurations, at three excitation powers close to saturation, and $T_L = 16$ ns. The experimental data are normalized and fitted by the theoretical intensity correlation function $g^{(2X)}$ given by equation (4.5) after its convolution with the Instrument Response Function (IRF) of the HOM setup (here, the detectors's time response is characterized by $T_R = 1$ ns). The fitting procedure only concerns the coefficient V_0 , the conversion coefficient between the excitation power and the Rabi pulsation Ω , and the contribution of the coherent parasitic laser background that has been introduced in chapter 3. We stress that the same set of parameters has been used for every fit: $R_{A(B)} = 0.45$ and $T_{A(B)} = 0.55$; $T_1 = 0.37$ ns and $T_2 = 0.54$ ns; $\Delta\tau = 43.5$ ns. Regarding V_0 , its value is $V_0 = 0.80$ (0.14) for parallel (orthogonal) polarization. The discrepancy between these extracted values and the theoretical ones [$V_0 = 1(0)$ for parallel (orthogonal) polarization] comes from the spatial mode mismatch and the non perfect degree of mutual polarizations between the interfering photons. These are mostly due to the use in the experimental setup of combined free space and fibered optics, non polarizing beamsplitters which introduce a

small polarization ellipticity, and the gratings of the spectrometers which have a polarization response that partly reestablishes interferences in the orthogonal configuration.

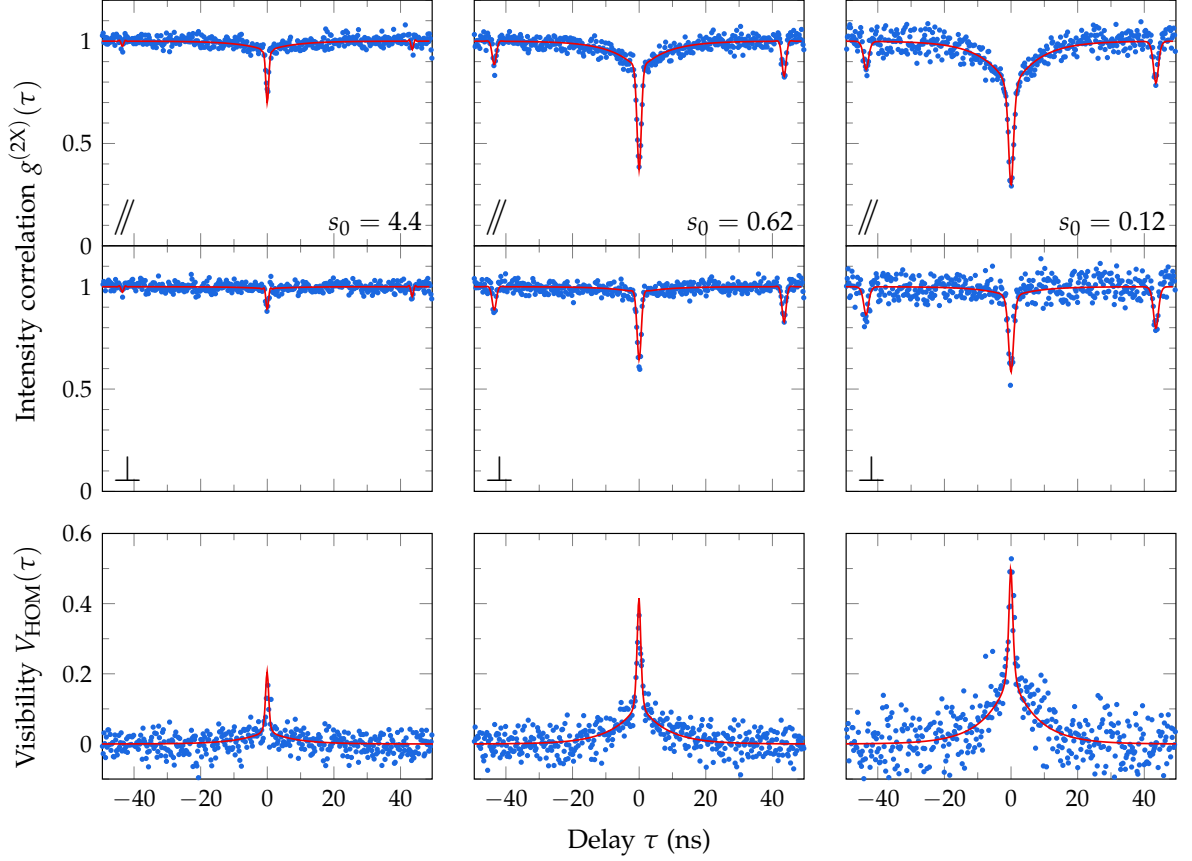


Figure 4.4: HOM two-photon interference measurements for parallel (\parallel) and orthogonal (\perp) polarization configurations for three excitation powers corresponding to $s_0 = 2.64$, 0.57 and 0.09 . Upper panels: intensity correlation functions $g_{\parallel}^{(2X)}$ and $g_{\perp}^{(2X)}$ as a function of the delay τ fitted by equation (4.5) with $V_0 = 0.80$ and $V_0 = 0.14$, respectively. The other parameters are set to $T_1 = 0.37$ ns, $T_2 = 0.54$ ns, $R_A = R_B = 0.45$, $T_A = T_B = 0.55$, and $\Delta\tau = 43.5$ ns. Lower panels: two-photon interference visibilities V_{HOM} deduced from the experimental data (dots) and fitted (line) by equation (4.7). All the fits take into account the coherent parasitic laser background and are convoluted by the Instrument Response Function (IRF). Figure extracted from Ref. [8].

In the orthogonal polarization configuration (second line of the upper panels), as explained in the previous section, no interference is expected and the measured $g_{\perp}^{(2X)}$ function is related to the statistical properties of the single photon source when light is sent through the Mach-Zehnder interferometer. Compared to an HBT experiment, additional antibunching dips shifted by the interferometer paths difference are observed at $\tau = \pm\Delta\tau$ with a slight amplitudes difference due to the non equilibrated beamsplitters. Here, the three measured dip values, which are resolution limited, are determined by the QD intrinsic times T_1 and T_2 . Moreover, at high power, the QD undergoes Rabi oscillations that cannot be resolved with the present setup, inducing a narrowing of the antibunching dips [22] and thus a strong reduction of their visibility for the given T_R .

In the parallel polarization configuration (first line of the upper panels), in addition to

the contribution of the photon statistics, a component due to photon coalescence is observed on the central dip. Furthermore, when focusing on the dip at zero delay, two dynamics can be distinguished at low power: a fast one at $\tau \ll T_R$ characterized by the intrinsic QD time constants T_1 and T_2 , which reflects the photon statistics and the coalescence of the inelastically scattered photons; and a much slower one characterized by half the coherence time of the excitation laser $T_L/2$, which is directly linked to the coalescence of the elastically scattered photons. The two-photon interference measurements performed in the RRS regime thus also exhibit very clearly the two time scales linked to the elastic and inelastic components of the resonance fluorescence as already observed in the measurements of the first-order correlation function $g^{(1)}$ (see chapter 3). Therefore, these results constitute a clear demonstration of the direct link between the additional coalescence component and the $g^{(1)}$ function, and thus the coherence of the emitted photons. Studying the photon indistinguishability in the particular RRS regime provides a straightforward evidence of Mandel's notion regarding the duality between coherence and indistinguishability [163], which cannot be observed in more conventional excitation regimes such as non-resonant excitation or resonant excitation above saturation. In fact, at high power, as the ratio of the elastically scattered photons drops, the long time component gets notably attenuated. The contributions of the statistics and the coalescence of the inelastically scattered photons then becomes difficult to discriminate in the central component because the same time constants are involved. The difference can only be observed in the values of $g_{\parallel}^{(2X)}$ and $g_{\perp}^{(2X)}$ at zero delay: for example at $s_0 = 2.64$, $g_{\parallel}^{(2X)}(0) = 0.57$ and $g_{\perp}^{(2X)}(0) = 0.72$ while the FWHM equals 1.1 ns for both functions.

All these properties are also observed in the visibility of the two-photon interference experiment, $V_{\text{HOM}}(\tau)$, that is deduced from the measurements of the intensity correlation functions $g_{\parallel}^{(2X)}(\tau)$ and $g_{\perp}^{(2X)}(\tau)$, and presented in figure 4.4 (lower panels). The data are fitted by equation (4.7) with the same set of parameters used for the $g^{(2X)}$ functions, where only the coefficients V_0 and s_0 are adjusted. As it is commonly done, the value at zero delay of the visibility, $V_{\text{HOM}}(0)$, can be used to characterize the degree of photon indistinguishability of our single photon source. Within such a figure of merit, as shown by the power dependence of $V_{\text{HOM}}(0)$ in figure 4.5, the maximum degree of photon indistinguishability of our "ultra-coherent" single photon source reaches 0.49 ± 0.06 for $s_0 = 0.09$ in the RRS regime, while the photon indistinguishability drastically decreases above saturation with $V_{\text{HOM}}(0) = 0.14 \pm 0.03$ at $s_0 = 3.4$. As expected, we note that the maximum visibility of 0.49 is well above the visibilities measured for QDs under cw non-resonant excitation ($V_{\text{HOM}}(0) = 0.33$) [160, 161] thanks to the minimization of the pure dephasing processes under resonant excitation leading to a longer decoherence time. However, the maximum visibility measured in our system is comparable to the ones measured for other cw resonantly-driven single QDs below saturation ($V_{\text{HOM}}(0) = 0.44$) [168], with the exception of a study of P. Michler's group [18], where the HOM visibility reaches 0.60 at $\tau = 0$ because of the longer time constants T_1 and T_2 at stake. Nevertheless, in every configurations, the HOM visibility at $\tau = 0$ is mostly limited by the finite time response of the detectors since the non convoluted visibilities can reach values as high as ~ 0.90 at $\tau = 0$ [18, 161], the remaining limitation being only the imperfections of the interferometer alignment given by the parameter V_0 .

This statement is further illustrated by the figure 4.5 where the non convoluted value of $V_{\text{HOM}}(0)$ (dashed line) reaches 0.75 in our case ³ and does not depend on the excitation power. It appears then that the QD time constants and the coherence time of the emitted photons

³The lower value of $V_{\text{HOM}}(0)$ is due to the tricky alignment of our long delayed HOM interferometer.

play only an indirect role in the value of $V_{\text{HOM}}(0)$ and, therefore, to the estimation of the degree of photon indistinguishability of a single photon source. In this context, we assume that a more appropriate figure of merit needs to be defined in order to fully characterize the photon indistinguishability of a cw single photon source.

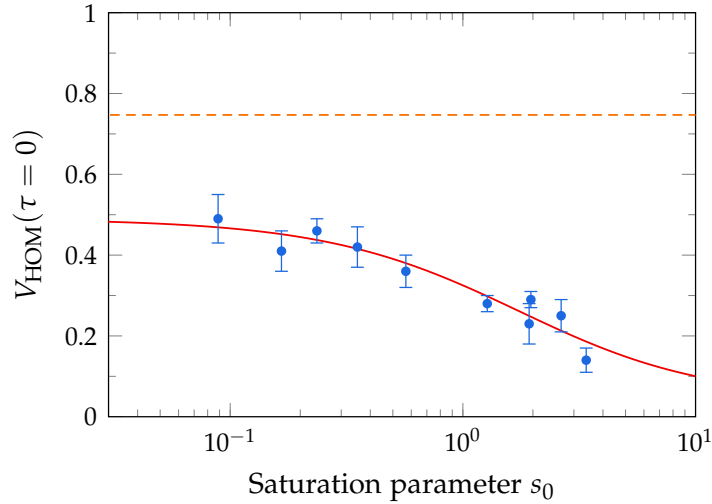


Figure 4.5: Power dependence of the Hong-Ou-Mandel (HOM) two-photon interference visibility, $V_{\text{HOM}}(\tau = 0)$. The experimental data (dots) and the fit (solid line), convoluted by the Instrument Response Function (IRF), are displayed as a function of the saturation parameter s_0 . The corresponding non convoluted values of $V_{\text{HOM}}(\tau = 0)$ are also presented (dashed line). Figure extracted from Ref. [8].

4.3 The coalescence time window

The interpretation of an HOM two-photon interference experiment and thus the estimation of the photon indistinguishability are fundamentally different when considering a pulsed or a cw excitation. This statement is first discussed in order then to define a new figure of merit which better takes into account the nature and the operation mode of a single photon source when characterizing the indistinguishability of the emitted photons.

On the one hand, under pulsed excitation, the experiment which is schematized in figure 4.6 (left panel) consists in adjusting the interferometer delay (2 ns in that case) in order to perfectly match the arrival times on the second beamsplitter of two consecutive photons. The coincidences rate is then measured at the outputs of the beamsplitter and a vanishing value due to the coalescence phenomenon, and therefore a maximum of the two-photon interference visibility, is expected for indistinguishable photons. An example of the first result of an HOM experiment performed under non-resonant pulsed excitation in QDs [16] is presented in figure 4.6 (right panel). This study shows that the minimum coincidence rate is limited by the fluctuations of the QD emission energy due to pure dephasing. The time constants of the QD, T_2 and T_1 , are then tightly linked to the photon indistinguishability and the ratio $T_2/2T_1$ corresponding to the overlap probability of two consecutive photons constitutes a fundamental limit to the coalescence efficiency [159]. Consequently, the value of the two-photon interference visibility at zero time delay directly gives the degree of photon indistinguishability which is maximum when the radiative limit $T_2 = 2T_1$ is reached.

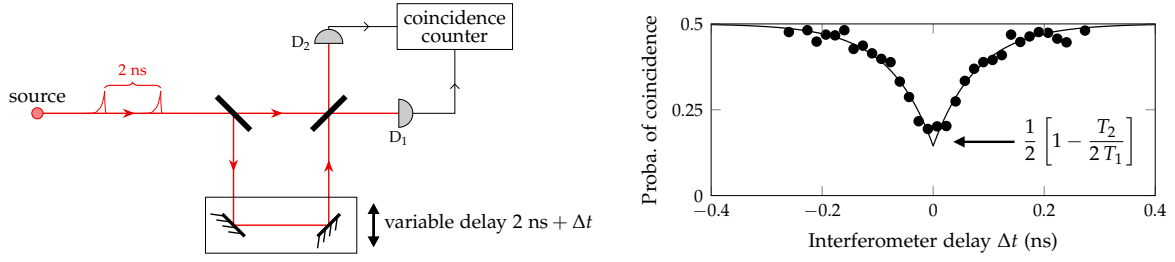


Figure 4.6: Left panel: Scheme of a Hong-Ou-Mandel (HOM) interferometer in case of a pulsed excitation. The delay between the two arms is variable and the number of coincidences between the two photodetectors D_1 and D_2 is measured (Δt on the figure corresponds to $\Delta\tau$ in the text). Right panel: Probability of coincidences as a function of the interferometer delay for a single QD under non-resonant pulsed excitation [16].

On the other hand, as depicted in figure 4.7 (left panel), for a cw excitation, a continuous stream of photons is sent to the HOM interferometer where both mirrors are fixed, and the second-order correlation function $g^{(2X)}$ is directly measured as a function of the electronic delay between the detection times at the photodetectors. An example of a result obtained under cw non-resonant excitation in single QDs is presented in figure 4.7 (right panel). The HOM dip that is observed at zero time delay in the correlation function $g_{//}^{(2X)}$ reflects the coalescence phenomenon of indistinguishable photons and its value is used for assessing the degree of photon indistinguishability. However, the ratio $T_2/2T_1$ has no direct influence on the value of $g_{//}^{(2X)}(0)$ since no time synchronization is required, but it governs the temporal width of the HOM dip. These properties constitute the main difference with the pulsed excitation configuration. In the case of real detectors, the HOM dip is in fact properly resolved only if the temporal resolution of the detectors T_R is shorter than the coherence time of the photons [169]. If $T_R \sim T_1, T_2$, the HOM dip is strongly affected and will disappear completely in the limit of very slow detectors. On the contrary, with two ideal ultrafast detectors, the coincidence rate always vanishes at zero time delay, even for deviations in the properties of the photons [154]. Consequently, under cw excitation, the value at zero delay of the coincidence rate is very sensitive to T_R and does not accurately characterize the intrinsic properties of the source with regard to photon indistinguishability. Moreover, as usual, the convolution of the measurements with the time response of the setup couple both the value at zero delay and

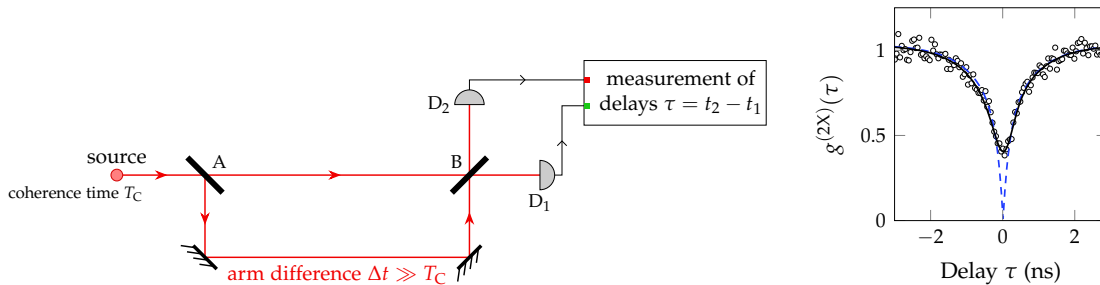


Figure 4.7: Left panel: Scheme of a Hong-Ou-Mandel (HOM) interferometer in case of a cw excitation. The delay between the two arms Δt is fixed and set to be longer than the coherence time of the source T_C (Δt on the figure corresponds to $\Delta\tau$ in the text). The temporal delay $\tau = t_2 - t_1$ between two detections is measured. Right panel: Intensity correlation function $g^{(2X)}(\tau)$ as a function of the delay τ for a single QD under cw non-resonant excitation [160].

the temporal width of the correlation function, which becomes problematic when longer time constants are involved like in the RRS regime.

From a general point of view, we conclude that another figure of merit should be considered to fully characterize the degree of indistinguishability of a cw source. In fact, as far as the resonance fluorescence of a TLS is concerned, a more appropriate figure of merit must be defined in order to give a comprehensive insight of photon indistinguishability on both low and high power regimes. More specifically, in the RRS regime, the long coherence time of the elastically scattered photons along with the visibility of the two-photon interference at $\tau = 0$ have to be taken into account in the estimation of the photon indistinguishability. In this context, the time integration of the visibility curve, or what we call the coalescence time window (CTW), is used under cw excitation in order to investigate the temporal behavior of the coalescence efficiency. As an example, the CTW is directly linked to the width of the visibility curve when only one time constant is involved, whereas the CTW is equal to a weighted average time which takes into account all the temporal components of the coalescence dynamics when different time constants are involved. Therefore, the temporal dynamics of the photon coalescence phenomenon can be experimentally investigated by the CTW which quantifies the time window in which two-photon interference is observed, while being independent of T_R .

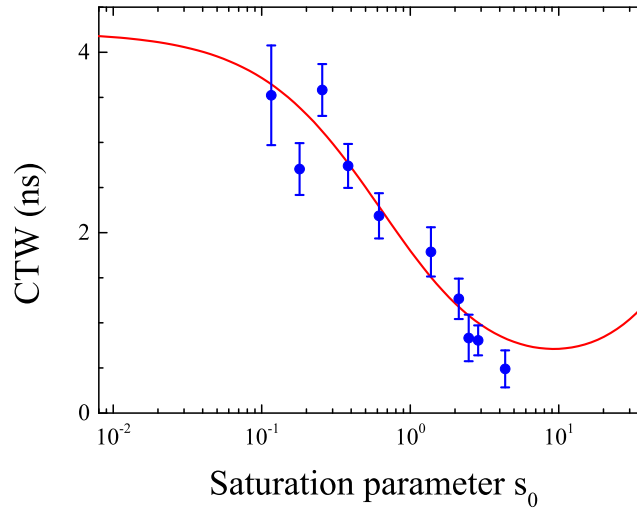


Figure 4.8: Coalescence time window (CTW) deduced from the experimental (dots) and theoretical (line) visibilities V_{HOM} presented in figure 4.4 as a function of the saturation parameter s_0 . The laser coherence time is $T_L = 16$ ns · Figure extracted from Ref. [8].

Applying this method to the set of power measurements presented in figure 4.4 allows us to get a comprehensive study of the power dependence of the CTW and therefore of the indistinguishability of the photons emitted by the resonantly-driven QD. The results are shown in figure 4.8 where the CTW is deduced from the experimental and theoretical visibilities V_{HOM} . At low power (below saturation), it can be as large as 4 ns due to the long coherence of the photons inherited from the excitation laser in the RRS regime. The upper limit of the CTW at low power regime is thus related to the coherence time of the excitation laser, but we stress that the CTW is also limited by the coefficient V_0 and, as it is the case for the fraction of the elastically scattered photons in the resonance fluorescence signal, by the ratio $T_2/2T_1$. In fact, in the ideal case where the radiative limit is reached and the HOM

setup is perfectly aligned with $V_{0,\parallel} = 1$ and $V_{0,\perp} = 0$, the theoretical CTW equals 8.5 ns, which is slightly larger than $T_L/2$ (the excess is linked to the single photon statistic property of the source). When the power increases, the CTW is drastically reduced and goes below 1 ns above the saturation power. In this regime, the QD emission mostly originates from inelastic scattering, governed by the intrinsic time constants T_1 and T_2 which are of the order of T_R . As a comparison, the CTW calculated for a non-resonantly excited QD with the same time constants T_1 and T_2 equals 0.15 ns, similarly to the one measured at high power (i.e. 0.4 ns at $s_0 = 5$). Here, we conclude that photon coalescence can occur for time delays up to 4 times the temporal resolution of the detectors when the QD is operated in the RRS regime (with $T_L = 16$ ns), thanks to the slow dynamics achievable in this particular regime.

4.4 Control of the coalescence time window

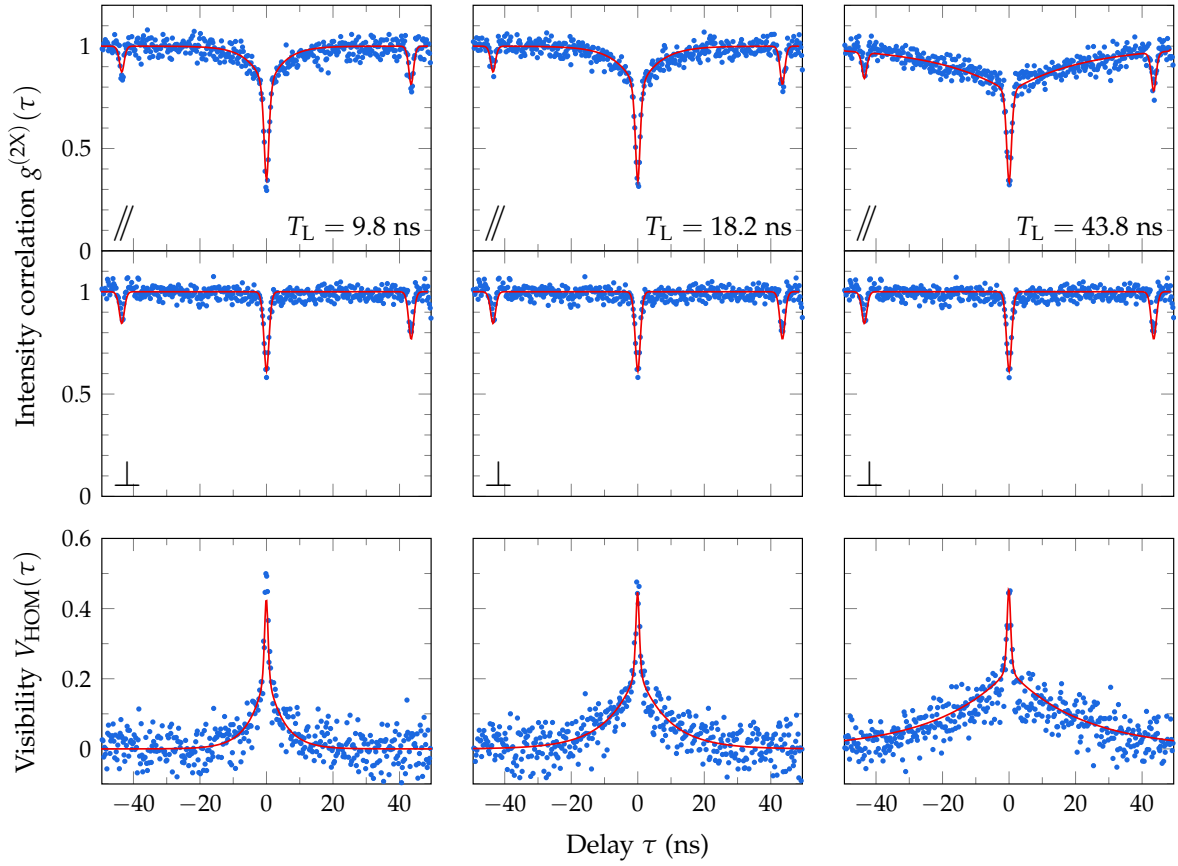


Figure 4.9: Hong-Ou-Mandel (HOM) two-photon interference measurements in the resonant Rayleigh scattering regime (i.e. $s_0 = 0.17$) for parallel (\parallel) and orthogonal (\perp) polarization configurations for three laser coherence times $T_L = 9.8$ ns, 18.2 ns and 43.8 ns. Upper panels: intensity correlation functions $g_{\parallel}^{(2X)}$ and $g_{\perp}^{(2X)}$ as a function of the delay τ fitted by equation (4.5), with $V_{0,\parallel} = 0.80$ and $V_{0,\perp} = 0$. The other parameters are set to $T_1 = 0.37$ ns, $T_2 = 0.54$ ns, $R_A = R_B = 0.45$, $T_A = T_B = 0.55$, and $\Delta\tau = 43.5$ ns. Lower panels: two-photon interference visibilities V_{HOM} deduced from the experimental data (dots) and fitted (line) by equation (4.7). All the fits take into account the coherent parasitic laser background and are convoluted by the Instrument Response Function (IRF). Figure extracted from Ref. [8].

As presented in chapter 3, the photons emitted by the single QD in the RRS inherits the coherence of the excitation laser while still being antibunched. In this context, we have studied the dependence of the photon indistinguishability with the coherence time of the laser T_L , when the QD is operated in the RRS.

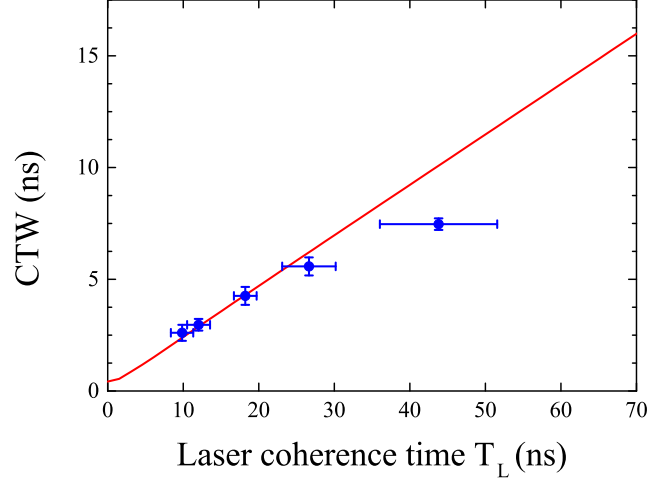


Figure 4.10: Coalescence time window (CTW) deduced from the experimental (dots) and theoretical (line) visibilities V_{HOM} presented in figure 4.9 as a function of the laser coherence time T_L . Figure extracted from Ref. [8].

Figure 4.9 presents intensity correlation measurements realized with the HOM setup in the parallel and orthogonal polarization configurations, at low excitation powers ($s_0 = 0.17$) for three laser coherence times. The correlation function $g^{(2X)}$ (upper panels) is shown as a function of the delay τ in each polarization configuration along with the corresponding two-photon interference visibility V_{HOM} (lower panels). The experimental conditions set the reachable range of T_L , between 9.8 ns due to the limitations of the diode laser and 43.5 ns imposed by the interferometer delay $\Delta\tau$. At a given excitation power, the ratio of the elastically scattered photons remains constant ($I_{\text{RRS}}/I \approx 70\%$), and the increase of T_L is directly reflected on the slow component observed on the intensity correlation functions $g_{\parallel}^{(2X)}$ and on the visibilities. However, the modification of the laser coherence time hardly affects the visibility at zero delay since the contribution of the elastically scattered photons is here well resolved by the time response of the HOM setup. We note that this observation also shows that the value of $V_{\text{HOM}}(0)$ is not sufficient to fully characterize the photon indistinguishability of a cw single photon source operated in the RRS regime.

The experimental CTWs that are deduced from the previous results are presented as a function of T_L in figure 4.10 along with the corresponding theoretical fit. In the RRS regime, the CTW is mostly linear with the laser coherence time with a small deviation at $T_L = 43.8$ ns where the model is not valid anymore (as seen in section 4.1, the interferometer delay must be longer than the laser coherence time). This linear dependance reflects that the CTW is mostly governed by the laser coherence time at low power regime since T_L defines the main part of the area of the visibility curve. This leads to a CTW which can reach up to 8 ns with the current setup. This result has to be compared to the CTW of 0.15 ns that would be reached for a non-resonantly excited QD, or to the CTW of 0.4 ns measured for a resonantly driven QD at high power (above saturation). Moreover, the ratio $T_2/2T_1$ here only gives the

proportion of elastically scattered photons and does not limit intrinsically the CTW in the RRS regime. Therefore, these results show that highly indistinguishable single photons can be generated by a cw resonantly driven QD operated in the RRS regime since the CTW is limited neither by the intrinsic QD time constants nor T_R , and the higher the laser coherence time, the higher the CTW. The CTW fully characterizes the photon temporal indistinguishability of a cw single photon source, particularly in the RRS regime where photon coherence times are much longer than the temporal resolution of the detectors. Finally, this result not only demonstrates that coherence and indistinguishability are entwined, but also that the RRS regime allows for an unprecedented level of control of photon indistinguishability.

4.5 Conclusion

In this chapter, the generation of highly indistinguishable single photons from a cw resonantly driven QD operated in the RRS regime has been presented. In this regime, as the excitation laser drives the photon coherence time beyond the intrinsic properties of the TLS, the temporal dynamics of the photon coalescence phenomenon can be experimentally investigated. In fact, HOM two-photon experiments have shown that the photon indistinguishability can be extended to unprecedented levels and driven externally by the excitation laser which thus becomes a free controllable parameter of the device. An appropriate figure of merit, the coalescence time window (CTW), has been defined in order to quantify the time window in which two-photon coalescence is observed. This criterion sheds new light on the interpretation of HOM experiments under cw excitation of any TLS, which was traditionally restricted to the evaluation of the two-photon interference visibility at zero delay. This CTW then fully characterizes the photon temporal indistinguishability of a cw single photon source, particularly in the RRS regime where photon coherence times are much longer than the temporal resolution of the detectors. In our system, the CTW can be as large as 8ns in the present setup. Our results also highlight the duality between coherence and indistinguishability, first suggested by Mandel [163], and provide a novel way of conducting quantum optics experiments by overcoming the limited response function of the detectors.

Conclusion

This manuscript has presented our contributions in the field of the resonance fluorescence of single semiconductor quantum dots (QD) for the generation of indistinguishable photons. At the beginning of our project, we showed that the experimental studies performed at low temperature ($T = 10$ K) of the optical properties of single QDs under strictly resonant excitation could be strongly limited, even impossible, since most of the QDs show a very strong quenching of the resonance fluorescence at the energy of the neutral exciton. This broadly met experimental situation is problematic for quantum optics experiments with single QDs, and more generally for the development of efficient QD-based single photon sources, but we proposed an efficient way to overcome this issue based on the use of an ultra-weak non-resonant laser that optically gates the QDs resonant response. The different capture and escape processes, that are induced by the optical gate in an unprecedented explored regime of ultra-slow dynamics, result in the photo-neutralization of the QDs charge state and in a complete recovery of the properties of an artificial atom. Nevertheless, the single QDs still behave as non ideal two-level systems (TLS) since the residual doping in the vicinity of the QDs prevents the radiative limit $T_2 = 2T_1$ to be reached. As a consequence, even if the resonant excitation configuration already allows to greatly reduce the interactions of the QDs with their electrostatic environment, a better control of the residual doping remains necessary.

Meanwhile, we proposed an original type of single photon source based on the coherent laser light scattering by a single semiconductor QD, better known as the resonant Rayleigh scattering (RRS), which dominates the resonance fluorescence signal at low power. Besides the antibunching effect showing the non-classical nature of the emitted light in such configuration, the QD emission spectrum is determined by the spectrum of the resonant excitation laser. This leads to the striking feature where single photons are emitted within a narrower spectral linewidth than the one imposed by the radiative limit, resulting in what we called an "ultra-coherent" single photon emission. A direct consequence of such behavior is the emission of highly indistinguishable photons. This statement was demonstrated in a two-photon interference experiment performed in the RRS regime, by investigating the coalescence time window (CTW) – a new criterium which fully characterizes the photon temporal indistinguishability of a cw single photon source by quantifying the time window in which two consecutive photons remain indistinguishable. Even if the ratio $T_2/2T_1$ still governs the fraction of RRS, contrary to the more conventional non-resonant excitation or high power resonant excitation configurations, the radiative limit imposed by the QD electronic properties does not rule anymore the degree of indistinguishability of the emitted photons in the RRS regime. Furthermore, our "ultra-coherent" single photon source opens the way for integrated quantum devices where the generation of indistinguishable single photons is tailored by the excitation laser source since the latter acts as a free tuning parameter of the coherence of the emitted photons.

Concerning the perspectives of such "ultra-coherent" single photon source, the new degree

of freedom on the coherence and thus the indistinguishability of the emitted photons could promote conducting quantum optics with conventional detectors, and circumvent what constitutes one of the main limitations for manipulating indistinguishable photons generated by a solid state cw light source. As the CTW in the RRS regime exceeds the temporal resolution of regular detectors, a precise timing of the photons could be ensured without using narrow spectral filters or superconducting detectors [170], which would then allow implementing time entanglement of photon pairs by the mean of a Franson interferometer [170–172].

The recent work of the group of M. Atatüre on the generation of quadrature squeezed photons by coherently-driven single QDs operated in the RRS regime [173], based on intensity-field correlations measurements [174–177], also shows that a solid state TLS in interaction with a weak resonant light field could play a new role in quantum optics applications such as the development of integrated low quantum noise light sources for interferometry measurements.

Another recent study done in the groups of D. A. Ritchie and A. J. Shields showed that the nonlinear interaction between the coherently scattered light from a single QD and the non-interacted photons of the resonant laser can also be exploited to realize "a photon-sorter" in terms of photon number and polarization [178]. It shows that such "ultra-coherent" single photon source can generate strongly correlated photons without requiring strong coupling or intense optical fields.

To conclude, from a more general applicative point of view, a huge effort is actually made in the development of a new generation of QD-based devices, integrating electrically-controlled single photon sources [136], beamsplitters [179] and photodetectors [180], for on-chip quantum optics experiments [105, 181–184] at a larger scale. This field of research relies on the fabrication of more and more complex structures which elaboration still benefits from the deep understanding of the fundamental phenomena that govern the physics of semiconductor QDs.

Bibliography

- [1] Cécile Kammerer. *Spectroscopie optique de boîtes quantiques uniques: effets de l'environnement*. PhD thesis, Université Pierre et Marie Curie - Paris VI, 2002.
- [2] Ivan Favero. *Décohérence, symétries et relaxation de spin dans les boîtes quantiques de semiconducteurs*. PhD thesis, Université Pierre et Marie Curie - Paris VI, 2005.
- [3] Alice Berthelot. *Diffusion spectrale et rétrécissement par le mouvement dans les boîtes quantiques*. PhD thesis, Université Pierre et Marie Curie - Paris VI, 2008.
- [4] Guillaume Cassabois. *Origines et limites du modèle de l'atome artificiel pour une boîte quantique de semiconducteurs*. Habilitation à diriger des recherches (HDR), Université Pierre et Marie Curie - Paris VI, 2006.
- [5] A. Muller, E. B. Flagg, P. Bianucci, X. Y. Wang, D. G. Deppe, W. Ma, J. Zhang, G. J. Salamo, M. Xiao, and C. K. Shih. Resonance fluorescence from a coherently driven semiconductor quantum dot in a cavity. *Physical Review Letters*, 99:187402, 2007.
- [6] R. Melet, V. Voliotis, A. Enderlin, D. Roditchev, X. L. Wang, T. Guillet, and R. Grousson. Resonant excitonic emission of a single quantum dot in the Rabi regime. *Physical Review B*, 78:073301, 2008.
- [7] Hai Son Nguyen. *Contrôle optique de l'émission résonnante de boîtes quantiques semiconductrices*. PhD thesis, Université Pierre et Marie Curie - Paris VI, 2011.
- [8] Raphaël Proux. *Indiscernabilité des photons émis par une boîte quantique semiconductrice sous excitation résonnante continue*. PhD thesis, Ecole Normale Supérieure, 2015.
- [9] H. J. Kimble, M. Dagenais, and L. Mandel. Photon antibunching in resonance fluorescence. *Physical Review Letters*, 39(11):691–695, 1977.
- [10] F. Diedrich and H. Walther. Nonclassical radiation of a single stored ion. *Physical Review Letters*, 58(3):203–206, 1987.
- [11] Th. Basché, W. E. Moerner, M. Orrit, and H. Talon. Photon antibunching in the fluorescence of a single dye molecule trapped in a solid. *Physical Review Letters*, 69(10):1516–1519, 1992.
- [12] C. Kurtsiefer, S. Mayer, P. Zarda, and H. Weinfurter. Stable solid-state source of single photons. *Physical Review Letters*, 85:290–293, 2000.
- [13] P. Michler, A. Kiraz, C. Becher, W. V. Schoenfeld, P. M. Petroff, Lidong Zhang, E. Hu, and A. Imamoglu. A quantum dot single-photon turnstile device. *Science*, 290(5500):2282–2285, 2000.
- [14] R. M. Stevenson, R. J. Young, P. Atkinson, K. Cooper, D. A. Ritchie, and A. J. Shields. A semiconductor source of triggered entangled photon pairs. *Nature*, 439:179–182, 2006.
- [15] N. Akopian, N. H. Lindner, E. Poem, Y. Berlatzky, J. Avron, D. Gershoni, B. D. Gerardot, and P. M. Petroff. Entangled Photon Pairs from Semiconductor Quantum Dots. *Physical Review Letters*, 96:130501, 2006.
- [16] C. Santori, D. Fattal, J. Vučković, G. S. Solomon, and Y. Yamamoto. Indistinguishable photons from a single-photon device. *Nature*, 419(6907):594–597, 2002.
- [17] S. Varoutsis, S. Laurent, P. Kramper, A. Lemaître, I. Sagnes, I. Robert-Philip, and I. Abram. Restoration of photon indistinguishability in the emission of a semiconductor quantum dot. *Physical Review B*, 72:041303, 2005.
- [18] S. Ates, S. M. Ulrich, S. Reitzenstein, A. Löffler, A. Forchel, and P. Michler. Post-selected indistinguishable photons from the resonance fluorescence of a single quantum dot in a microcavity. *Physical Review Letters*, 103:167402, 2009.

- [19] A. N. Vamivakas, Y. Zhao, C. Y. Lu, and M. Atatüre. Spin-resolved quantum-dot resonance fluorescence. *Nature Physics*, 5:198–202, 2009.
- [20] H. S. Nguyen, G. Sallen, C. Voisin, Ph. Roussignol, C. Diederichs, and G. Cassaboïs. Optically gated resonant emission of single quantum dots. *Physical Review Letters*, 108:057401, 2012.
- [21] A. Reinhard, T. Volz, M. Winger, A. Badolato, K. J. Hennessy, E. L. Hu, and A. Imamoglu. Strongly correlated photons on a chip. *Nature Photonics*, 6(2):93–96, 2012.
- [22] E. B. Flagg, A. Muller, J. W. Robertson, S. Founta, D. G. Deppe, M. Xiao, W. Ma, G. J. Salamo, and C. K. Shih. Resonantly driven coherent oscillations in a solid-state quantum emitter. *Nature Physics*, 5:203, 2009.
- [23] H. S. Nguyen, G. Sallen, M. Abbarchi, R. Ferreira, C. Voisin, Ph. Roussignol, G. Cassaboïs, and C. Diederichs. Photoneutralization and slow capture of carriers in quantum dots probed by resonant excitation spectroscopy. *Physical Review B*, 87:115305, 2013.
- [24] H. S. Nguyen, G. Sallen, C. Voisin, Ph. Roussignol, C. Diederichs, and G. Cassaboïs. Ultra-coherent single photon source. *Applied Physics Letters*, 99(26):261904, 2011.
- [25] R. Proux, M. Maragkou, E. Baudin, C. Voisin, Ph. Roussignol, and C. Diederichs. Measuring the photon coalescence time window in the continuous-wave regime for resonantly driven semiconductor quantum dots. *Physical Review Letters*, 114:067401, 2015.
- [26] P. Yu and M. Cardona. *Fundamentals of semiconductors*. Springer.
- [27] A. I. Ekimov, A. L. Efros, and A. A. Onushchenko. Quantum size effect in semiconductor microcrystals. *Solid State Communications*, 56(11):921–924, 1985.
- [28] L. Goldstein, F. Glas, J. Y. Marzin, M. N. Charasse, and G. Le Roux. Growth by molecular beam epitaxy and characterization of InAs/GaAs strained layer superlattices. *Applied Physics Letters*, 47(10):1099–1101, 1985.
- [29] I. Stranski and L. Krastanov. Abhandlungen der Mathematisch-Naturwissenschaftlichen Klasse IIb. *Akademie der Wissenschaften Wien*, 146:797–810, 1938.
- [30] J. M. Gérard, J. B. Génin, J. Lefebvre, J. M. Moison, N. Lebouché, and F. Barthe. Optical investigation of the self-organized growth of InAs/GaAs quantum boxes. *Journal of Crystal Growth*, 150, Part 1:351 – 356, 1995.
- [31] D. Leonard, M. Krishnamurthy, C. M. Reaves, S. P. Denbaars, and P. M. Petroff. Direct formation of quantum sized dots from uniform coherent islands of InGaAs on GaAs surfaces. *Applied Physics Letters*, 63(23):3203–3205, 1993.
- [32] N. Koguchi, S. Takahashi, and T. Chikyow. New MBE growth method for InSb quantum well boxes. *Journal of Crystal Growth*, 111:688 – 692, 1991.
- [33] K. Watanabe, N. Koguchi, and Y. Gotoh. Fabrication of GaAs quantum dots by modified droplet epitaxy. *Japanese Journal of Applied Physics*, 39(2A):L79, 2000.
- [34] T. B. Bahder. Eight-band $\mathbf{k} \cdot \mathbf{p}$ model of strained zinc-blende crystals. *Physical Review B*, 41:11992–12001, 1990.
- [35] G. Bastard. *Wave mechanics applied to semiconductor heterostructures*. Les éditions de physique.
- [36] A. Vasanelli, R. Ferreira, and G. Bastard. Continuous absorption background and decoherence in quantum dots. *Physical Review Letters*, 89:216804, 2002.
- [37] Y. Toda, O. Moriwaki, M. Nishioka, and Y. Arakawa. Efficient carrier relaxation mechanism in InGaAs/GaAs self-assembled quantum dots based on the existence of continuum states. *Physical Review Letters*, 82:4114–4117, 1999.
- [38] C. Kammerer, G. Cassaboïs, C. Voisin, C. Delalande, Ph. Roussignol, and J. M. Gérard. Photoluminescence up-conversion in single self-assembled InAs/GaAs quantum dots. *Physical Review Letters*, 87:207401, 2001.
- [39] E. Moreau, I. Robert, L. Manin, V. Thierry-Mieg, J. M. Gérard, and I. Abram. Quantum cascade of photons in semiconductor quantum dots. *Physical Review letters*, 87:183601, 2001.
- [40] G. Munoz-Matutano, J. Gomis, B. Alén, J. Martínez-Pastor, L. Seravalli, P. Frigeri, and S. Franchi. Exciton, biexciton and trion recombination dynamics in a single quantum dot under selective optical pumping. *Physica E: Low-dimensional Systems and Nanostructures*, 40(6):2100 – 2103, 2008.

- [41] P. Michler, editor. *Single Quantum Dots: Fundamentals, Applications, and New Concepts*. Springer.
- [42] R. Ferreira and G. Bastard. Phonon-assisted capture and intradot Auger relaxation in quantum dots. *Applied Physics Letters*, 74(19):2818–2820, 1999.
- [43] I. Magnusdottir, A. V. Uskov, S. Bischoff, B. Tromborg, and J. Mørk. One- and two-phonon capture processes in quantum dots. *Journal of Applied Physics*, 92(10):5982–5990, 2002.
- [44] A. V. Uskov, J. McInerney, F. Adler, H. Schweizer, and M. H. Pilkuhn. Auger carrier capture kinetics in self-assembled quantum dot structures. *Applied Physics Letters*, 72(1):58–60, 1998.
- [45] I. Magnusdottir, S. Bischoff, A. V. Uskov, and J. Mørk. Geometry dependence of Auger carrier capture rates into cone-shaped self-assembled quantum dots. *Physical Review B*, 67:205326, 2003.
- [46] B. Ohnesorge, M. Albrecht, J. Oshinowo, A. Forchel, and Y. Arakawa. Rapid carrier relaxation in self-assembled $\text{In}_x\text{Ga}_{1-x}\text{As}/\text{GaAs}$ quantum dots. *Physical Review B*, 54:11532–11538, 1996.
- [47] D. Elvira, R. Hostein, B. Fain, L. Monniello, A. Michon, G. Beaudoin, R. Braive, I. Robert-Philip, I. Abram, I. Sagnes, and A. Beveratos. Single $\text{InAs}_{1-x}\text{P}_x/\text{InP}$ quantum dots as telecommunications-band photon sources. *Physical Review B*, 84:195302, 2011.
- [48] G. A. Narvaez, G. Bester, and A. Zunger. Carrier relaxation mechanisms in self-assembled $(\text{In}, \text{Ga})\text{As}/\text{GaAs}$ quantum dots: Efficient $p \rightarrow s$ Auger relaxation of electrons. *Physical Review B*, 74:075403, 2006.
- [49] T. S. Sosnowski, T. B. Norris, H. Jiang, J. Singh, K. Kamath, and P. Bhattacharya. Rapid carrier relaxation in $\text{In}_{0.4}\text{Ga}_{0.6}\text{As}/\text{GaAs}$ quantum dots characterized by differential transmission spectroscopy. *Physical Review B*, 57:R9423–R9426, 1998.
- [50] T. Müller, F. F. Schrey, G. Strasser, and K. Unterrainer. Ultrafast intraband spectroscopy of electron capture and relaxation in InAs/GaAs quantum dots. *Applied Physics Letters*, 83(17):3572–3574, 2003.
- [51] L. Zhang, T. F. Boggess, K. Gundogdu, M. E. Flatté, D. G. Deppe, C. Cao, and O. B. Shchekin. Excited-state dynamics and carrier capture in $\text{InGaAs}/\text{GaAs}$ quantum dots. *Applied Physics Letters*, 79(20):3320–3322, 2001.
- [52] J. Siegert, S. Marcinkevičius, and Q. X. Zhao. Carrier dynamics in modulation-doped InAs/GaAs quantum dots. *Physical Review B*, 72:085316, 2005.
- [53] C. Kammerer, C. Voisin, G. Cassaboïs, C. Delalande, Ph. Roussignol, F. Klopff, J. P. Reithmaier, A. Forchel, and J. M. Gérard. Line narrowing in single semiconductor quantum dots: Toward the control of environment effects. *Physical Review B*, 66:041306, 2002.
- [54] C. Cohen-Tannoudji, J. Dupont-Roc, and G. Grynberg. *Atom-Photon Interactions: Basic Processes and Applications*. Wiley Science Paperback Series.
- [55] C. Santori, D. Fattal, and Y. Yamamoto. *Single-photon Devices and Applications*. John Wiley & Sons.
- [56] N. Gisin, G. Ribordy, W. Tittel, and H. Zbinden. Quantum cryptography. *Review of Modern Physics*, 74:145–195, 2002.
- [57] E. Knill, R. Laflamme, and G. J. Milburn. A scheme for efficient quantum computation with linear optics. *Nature*, 409:46–52, 2001.
- [58] A. Aspect, J. Dalibard, and G. Roger. Experimental Test of Bell’s Inequalities Using Time-Varying Analyzers. *Physical Review Letters*, 49:1804–1807, 1982.
- [59] A. Dousse, J. Suffczynski, A. Beveratos, O. Krebs, A. Lemaître, I. Sagnes, J. Bloch, P. Voisin, and P. Senellart. Ultrabright source of entangled photon pairs. *Nature*, 466:217, 2010.
- [60] C. L. Salter, R. M. Stevenson, I. Farrer, C. A. Nicoll, D. A. Ritchie, and A. J. Shields. An entangled-light-emitting diode. *Nature*, 465:595, 2010.
- [61] M. Müller, S. Bounouar, K. D. Jöns, M. Glassl, and P. Michler. On-demand generation of indistinguishable polarization-entangled photon pairs. *Nature Photonics*, 8:224–228, 2014.
- [62] H. Kamada, H. Gotoh, J. Temmyo, T. Takagahara, and H. Ando. Exciton Rabi oscillation in a single quantum dot. *Physical Review Letters*, 87:246401, 2001.
- [63] A. Zrenner, E. Beham, S. Stuffer, F. Findeis, M. Bichler, and G. Abstreiter. Coherent properties of a two-level system based on a quantum-dot photodiode. *Nature*, 418:612, 2002.
- [64] H. Jayakumar, A. Predojević, T. Huber, T. Kauten, G. S. Solomon, and G. Weihs. Deterministic photon pairs and coherent optical control of a single quantum dot. *Physical Review Letters*, 110:135505, 2013.

- [65] A. J. Ramsay. A review of the coherent optical control of the exciton and spin states of semiconductor quantum dots. *Semiconductor Science and Technology*, 25(10):103001, 2010.
- [66] Serge Haroche. Nobel lecture: Controlling photons in a box and exploring the quantum to classical boundary. *Review of Modern Physics*, 85:1083–1102, 2013.
- [67] E. M. Purcell. Spontaneous emission probabilities at radio frequencies. *Physical Review*, 69:681, 1946.
- [68] J. M. Gérard, B. Sermage, B. Gayral, B. Legrand, E. Costard, and V. Thierry-Mieg. Enhanced spontaneous emission by quantum boxes in a monolithic optical microcavity. *Physical Review Letters*, 81(5):1110–1113, 1998.
- [69] P. Lodahl, A. Floris van Driel, I. S. Nikolaev, A. Irman, K. Overgaag, D. Vanmaekelbergh, and W. L. Vos. Controlling the dynamics of spontaneous emission from quantum dots by photonic crystals. *Nature*, 430:654–657, 2004.
- [70] O. Gazzano, S. Michaelis de Vasconcellos, C. Arnold, A. Nowak, E. Galopin, I. Sagnes, L. Lanco, A. Lemaître, and P. Senellart. Bright solid-state sources of indistinguishable single photons. *Nature Communications*, 4:1425, 2013.
- [71] R. J. Thompson, G. Rempe, and H. J. Kimble. Observation of normal-mode splitting for an atom in an optical cavity. *Physical Review Letters*, 68:1132–1135, 1992.
- [72] J. P. Reithmaier, G. Sek, A. Löffler, C. Hofmann, S. Kuhn, S. Reitzenstein, L. V. Keldysh, V. D. Kulakovskii, T. L. Reinecke, and A. Forchel. Strong coupling in a single quantum dot semiconductor microcavity system. *Nature*, 432:197–200, 2004.
- [73] T. Yoshie, A. Scherer, J. Hendrickson, G. Khitrova, H. M. Gibbs, G. Rupper, C. Ell, O. B. Shchekin, and D. G. Deppe. Vacuum Rabi splitting with a single quantum dot in a photonic crystal nanocavity. *Nature*, 432:200, 2004.
- [74] E. Peter, P. Senellart, D. Martrou, A. Lemaître, J. Hours, J. M. Gérard, and J. Bloch. Exciton-photon strong-coupling regime for a single quantum dot embedded in a microcavity. *Physical Review Letters*, 95:067401, 2005.
- [75] K. Hennessy, A. Badolato, M. Winger, D. Gerace, M. Atatüre, S. Gulde, S. Fält, E. L. Hu, and A. Imamoglu. Quantum nature of a strongly correlated coupled single quantum dot-cavity system. *Nature*, 445:896–899, 2007.
- [76] C. H. Bennett and D. P. DiVincenzo. Quantum information and computation. *Nature*, 404:247–255, 2000.
- [77] K. M. Birnbaum, A. Boca, R. Miller, A. D. Boozer, T. E. Northup, and H. J. Kimble. Photon blockade in an optical cavity with one trapped atom. *Nature*, 436:87–90, 2005.
- [78] A. Faraon, I. Fushman, D. Englund, N. Stoltz, P. Petroff, and J. Vučković. Coherent generation of non-classical light on a chip via photon-induced tunnelling and blockade. *Nature Physics*, 4:859–863, 2008.
- [79] K. Müller, A. Rundquist, K. A. Fischer, T. Sarmiento, K. G. Lagoudakis, Y. A. Kelaita, C. Sánchez Muñoz, E. del Valle, F. P. Laussy, and J. Vučković. Coherent generation of nonclassical light on chip via detuned photon blockade. *Physical Review Letters*, 114:233601, 2015.
- [80] L. Besombes, K. Kheng, L. Marsal, and H. Mariette. Acoustic phonon broadening mechanism in single quantum dot emission. *Physical Review B*, 63:155307, 2001.
- [81] P. Borri, W. Langbein, S. Schneider, U. Woggon, R. L. Sellin, D. Ouyang, and D. Bimberg. Ultralong dephasing time in InGaAs quantum dots. *Physical Review Letters*, 87:157401, 2001.
- [82] I. Favero, G. Cassaboïs, R. Ferreira, D. Darson, C. Voisin, J. Tignon, C. Delalande, G. Bastard, Ph. Roussignol, and J. M. Gérard. Acoustic phonon sidebands in the emission line of single InAs/GaAs quantum dots. *Physical Review B*, 68:233301, 2003.
- [83] C. B. Duke and G. D. Mahan. Phonon-Broadened Impurity Spectra. I. Density of States. *Physical Review*, 139:A1965–A1982, 1965.
- [84] O. Verzeelen, R. Ferreira, and G. Bastard. Polaron lifetime and energy relaxation in semiconductor quantum dots. *Physical Review B*, 62:R4809–R4812, 2000.
- [85] T. Grange, R. Ferreira, and G. Bastard. Polaron relaxation in self-assembled quantum dots: Breakdown of the semiclassical model. *Physical Review B*, 76:241304, 2007.

- [86] S. Hameau, Y. Guldner, O. Verzellen, R. Ferreira, G. Bastard, J. Zeman, A. Lemaître, and J. M. Gérard. Strong electron-phonon coupling regime in quantum dots: Evidence for everlasting resonant polarons. *Physical Review Letters*, 83:4152–4155, 1999.
- [87] O. Verzellen, R. Ferreira, and G. Bastard. Excitonic polarons in semiconductor quantum dots. *Physical Review Letters*, 88:146803, 2002.
- [88] F. Vallée. Time-resolved investigation of coherent LO-phonon relaxation in III – V semiconductors. *Physical Review B*, 49:2460–2468, 1994.
- [89] H. D. Robinson and B. B. Goldberg. Light-induced spectral diffusion in single self-assembled quantum dots. *Physical Review B*, 61:R5086–R5089, 2000.
- [90] L. Besombes, K. Kheng, L. Marsal, and H. Mariette. Few-particle effects in single CdTe quantum dots. *Physical Review B*, 65:121314, 2002.
- [91] A. Berthelot, I. Favero, G. Cassaboïs, C. Voisin, C. Delalande, Ph. Roussignol, R. Ferreira, and J. M. Gérard. Unconventional motional narrowing in the optical spectrum of a semiconductor quantum dot. *Nature Physics*, 2(11):759–764, 2006.
- [92] I. Favero, A. Berthelot, G. Cassaboïs, C. Voisin, C. Delalande, Ph. Roussignol, R. Ferreira, and J. M. Gérard. Temperature dependence of the zero-phonon linewidth in quantum dots: An effect of the fluctuating environment. *Physical Review B*, 75:073308, 2007.
- [93] A. V. Khaetskii and Y. V. Nazarov. Spin relaxation in semiconductor quantum dots. *Physical Review B*, 61:12639–12642, 2000.
- [94] M. Paillard, X. Marie, P. Renucci, T. Amand, A. Jbeli, and J. M. Gérard. Spin relaxation quenching in semiconductor quantum dots. *Physical Review Letters*, 86:1634–1637, 2001.
- [95] R. Loudon. *The Quantum Theory of Light*. Oxford University Press.
- [96] M. O. Scully and M. S. Zubairy. *Quantum optics*. Cambridge University Press.
- [97] B. R. Mollow. Power spectrum of light scattered by two-level systems. *Physical Review*, 188:1969–1975, 1969.
- [98] C. Matthiesen, A. N. Vamivakas, and M. Atatüre. Subnatural linewidth single photons from a quantum dot. *Physical Review Letters*, 108:093602, 2012.
- [99] A. V. Kuhlmann, J. Houel, D. Brunner, A. Ludwig, D. Reuter, A. D. Wieck, and R. J. Warburton. A dark-field microscope for background-free detection of resonance fluorescence from single semiconductor quantum dots operating in a set-and-forget mode. *Review of Scientific Instruments*, 84:073905, 2013.
- [100] Y. M. He, Y. He, Y. J. Wei, W. Dian, M. Atatüre, C. Schneider, S. Höfling, M. Kamp, C.-Y. Lu, and J.-W. Pan. On-demand semiconductor single-photon source with near-unity indistinguishability. *Nature Nanotechnology*, 8:213–217, 2013.
- [101] R. N. E. Malein, T. S. Santana, J. M. Zajac, A. C. Dada, E. M. Gauger, P. M. Petroff, J. Y. Lim, J. D. Song, and B. D. Gerardot. Screening nuclear field fluctuations in quantum dots for indistinguishable photon generation. *Physical Review Letters*, 116:257401, 2016.
- [102] A. Högele, S. Seidl, M. Kroner, K. Karrai, R. J. Warburton, B. D. Gerardot, and P. M. Petroff. Voltage-controlled optics of a quantum dot. *Physical Review Letters*, 93:217401, 2004.
- [103] T. Volz, A. Reinhard, M. Winger, A. Badolato, K. J. Hennessy, E. L. Hu, and A. Imamoglu. Ultrafast all-optical switching by single photons. *Nature Photonics*, 6:605, 2012.
- [104] M. N. Makhonin, J. E. Dixon, R. J. Coles, B. Royall, I. J. Luxmoore, E. Clarke, M. Hugues, M. S. Skolnick, and A. M. Fox. Waveguide coupled resonance fluorescence from on-chip quantum emitter. *Nano Letters*, 14(12):6997–7002, 2014.
- [105] G. Reithmaier, M. Kaniber, F. Flassig, S. Lichtmannecker, K. Müller, A. Andrejew, J. Vučković, R. Gross, and J. J. Finley. On-chip generation, routing, and detection of resonance fluorescence. *Nano Letters*, 15(8):5208–5213, 2015.
- [106] A. Kurzman, A. Ludwig, A. D. Wieck, A. Lorke, and M. Geller. Photoelectron generation and capture in the resonance fluorescence of a quantum dot. *Applied Physics Letters*, 108(26):263108, 2016.
- [107] M. Bayer and A. Forchel. Temperature dependence of the exciton homogeneous linewidth in $\text{In}_{0.60}\text{Ga}_{0.40}\text{As}$ /GaAs self-assembled quantum dots. *Physical Review B*, 65:041308, 2002.

- [108] W. Langbein, P. Borri, U. Woggon, V. Stavarache, D. Reuter, and A. D. Wieck. Radiatively limited dephasing in InAs quantum dots. *Physical Review B*, 70:033301, 2004.
- [109] M. Hayne, O. Razinkova, S. Bersier, R. Heitz, L. Müller-Kirsch, M. Geller, D. Bimberg, and V. V. Moshchalkov. Optically induced charging effects in self-assembled GaSb/GaAs quantum dots. *Physical Review B*, 70:081302, 2004.
- [110] D. V. Regelman, E. Dekel, D. Gershoni, E. Ehrenfreund, A. J. Williamson, J. Shumway, A. Zunger, W. V. Schoenfeld, and P. M. Petroff. Optical spectroscopy of single quantum dots at tunable positive, neutral, and negative charge states. *Physical Review B*, 64:165301, 2001.
- [111] M. Ediger, P. A. Dalgarno, J. M. Smith, B. D. Gerardot, R. J. Warburton, K. Karrai, and P. M. Petroff. Controlled generation of neutral, negatively-charged and positively-charged excitons in the same single quantum dot. *Applied Physics Letters*, 86(21):211909, 2005.
- [112] J. J. Finley, D. J. Mowbray, M. S. Skolnick, A. D. Ashmore, C. Baker, A. F. G. Monte, and M. Hopkinson. Fine structure of charged and neutral excitons in InAs-Al_{0.6}Ga_{0.4}As quantum dots. *Physical Review B*, 66:153316, 2002.
- [113] E. S. Moskalenko, V. Donchev, K. F. Karlsson, P. O. Holtz, B. Monemar, W. V. Schoenfeld, J. M. Garcia, and P. M. Petroff. Effect of an additional infrared excitation on the luminescence efficiency of a single InAs/GaAs quantum dot. *Physical Review B*, 68:155317, 2003.
- [114] Y. Igarashi, M. Shirane, Y. Ota, M. Nomura, N. Kumagai, S. Ohkouchi, A. Kirihaara, S. Ishida, S. Iwamoto, S. Yorozu, and Y. Arakawa. Spin dynamics of excited trion states in a single InAs quantum dot. *Physical Review B*, 81:245304, 2010.
- [115] A. Hartmann, Y. Ducommun, E. Kapon, U. Hohenester, and E. Molinari. Few-particle effects in semiconductor quantum dots: Observation of multicharged excitons. *Physical Review Letters*, 84:5648–5651, 2000.
- [116] S. Mukamel. *Principles of Nonlinear Optics and Spectroscopy*. Oxford University Press.
- [117] R. G. Neuhauser, K. T. Shimizu, W. K. Woo, S. A. Empedocles, and M. G. Bawendi. Correlation between fluorescence intermittency and spectral diffusion in single semiconductor quantum dots. *Physical Review Letters*, 85:3301–3304, 2000.
- [118] G. Sallen, A. Tribu, T. Aichele, R. André, L. Besombes, C. Bougerol, M. Richard, S. Tatarenko, K. Kheng, and J. Ph. Poizat. Subnanosecond spectral diffusion measurement using photon correlation. *Nature Photonics*, 4:696, 2010.
- [119] M. Abbarchi, T. Kuroda, T. Mano, M. Gurioli, and K. Sakoda. Bunched photon statistics of the spectrally diffusive photoluminescence of single self-assembled GaAs quantum dots. *Physical Review B*, 86:115330, 2012.
- [120] K. Konthasinghe, J. Walker, M. Peiris, C. K. Shih, Y. Yu, M. F. Li, J. F. He, L. J. Wang, H. Q. Ni, Z. C. Niu, and A. Muller. Coherent versus incoherent light scattering from a quantum dot. *Physical Review B*, 85:235315, 2012.
- [121] C. Santori, D. Fattal, J. Vučković, G. S. Solomon, E. Waks, and Y. Yamamoto. Submicrosecond correlations in photoluminescence from InAs quantum dots. *Physical Review B*, 69:205324, 2004.
- [122] B. Piętka, J. Suffczyński, M. Goryca, T. Kazimierzczuk, A. Golnik, P. Kossacki, A. Wismolek, J. A. Gaj, R. Stępniewski, and M. Potemski. Photon correlation studies of charge variation in a single GaAlAs quantum dot. *Physical Review B*, 87:035310, 2013.
- [123] D. Chen, G. R. Lander, K. S. Krowpman, G. S. Solomon, and E. B. Flagg. Characterization of the local charge environment of a single quantum dot via resonance fluorescence. *Physical Review B*, 93:115307, 2016.
- [124] J. Gomis-Bresco, G. Munoz-Matutano, J. Martinez-Pastor, B. Alén, L. Seravalli, P. Frigeri, G. Trevisi, and S. Franchi. Random population model to explain the recombination dynamics in single InAs/GaAs quantum dots under selective optical pumping. *New Journal of Physics*, 13(2):023022, 2011.
- [125] M. Grundmann and D. Bimberg. Theory of random population for quantum dots. *Physical Review B*, 55:9740–9745, 1997.
- [126] J. M. Gérard and H. Mariette. Recent advances in quantum dot physics. *Comptes Rendus Physique*, 9(8):775 – 776, 2008.

- [127] P. Borri, W. Langbein, S. Schneider, U. Woggon, R. L. Sellin, D. Ouyang, and D. Bimberg. Rabi oscillations in the excitonic ground-state transition of InGaAs quantum dots. *Physical Review B*, 66:081306, 2002.
- [128] A. Muller, Q. Q. Wang, P. Bianucci, C. K. Shih, and Q. K. Xue. Determination of anisotropic dipole moments in self-assembled quantum dots using Rabi oscillations. *Applied Physics Letters*, 84(6):981–983, 2004.
- [129] T. Huber, A. Predojević, G. S. Solomon, and G. Weihs. Effects of photo-neutralization on the emission properties of quantum dots. *Optics Express*, 24(19):21794–21801, 2016.
- [130] J. Houel, A. V. Kuhlmann, L. Greuter, F. Xue, M. Poggio, B. D. Gerardot, P. A. Dalgarno, A. Badolato, P. M. Petroff, A. Ludwig, D. Reuter, A. D. Wieck, and R. J. Warburton. Probing single-charge fluctuations at a GaAs/AlAs interface using laser spectroscopy on a nearby InGaAs quantum dot. *Physical Review Letters*, 108:107401, 2012.
- [131] C. Arnold, V. Loo, A. Lemaître, I. Sagnes, O. Krebs, P. Voisin, P. Senellart, and L. Lanco. Cavity-Enhanced Real-Time Monitoring of Single-Charge Jumps at the Microsecond Time Scale. *Physical Review X*, 4:021004, 2014.
- [132] A. Berthelot, G. Cassaboïs, C. Voisin, C. Delalande, R. Ferreira, Ph. Roussignol, J. Skiba-Szymanska, R. Kolodka, A. I Tartakovskii, M. Hopkinson, and M. S. Skolnick. Voltage-controlled motional narrowing in a semiconductor quantum dot. *New Journal of Physics*, 11(9):093032, 2009.
- [133] D. Bajoni, E. Semenova, A. Lemaître, S. Bouchoule, E. Wertz, P. Senellart, and J. Bloch. Polariton light-emitting diode in a GaAs-based microcavity. *Physical Review B*, 77:113303, 2008.
- [134] C. Kistner, T. Heindel, C. Schneider, A. Rahimi-Iman, S. Reitzenstein, S. Höfling, and A. Forchel. Demonstration of strong coupling via electro-optical tuning in high-quality QD-micropillar systems. *Optics Express*, 16(19):15006–15012, 2008.
- [135] A. K. Nowak, S. L. Portalupi, V. Giesz, O. Gazzano, C. Dal Savio, P.-F. Braun, K. Karrai, C. Arnold, L. Lanco, I. Sagnes, A. Lemaître, and P. Senellart. Deterministic and electrically tunable bright single-photon source. *Nature Communications*, 5:3240, 2014.
- [136] N. Somaschi, V. Giesz, L. De Santis, J. C. Loredó, M. P. Almeida, G. Hornecker, S. L. Portalupi, T. Grange, C. Antón, J. Demory, C. Gómez, I. Sagnes, N. D. Lanzillotti-Kimura, A. Lemaître, A. Aufferes, A. G. White, L. Lanco, and P. Senellart. Near-optimal single-photon sources in the solid state. *Nature Photonics*, 10:340, 2016.
- [137] F. Hofbauer, S. Grimminger, J. Angele, G. Böhm, R. Meyer, M. C. Amann, and J. J. Finley. Electrically probing photonic bandgap phenomena in contacted defect nanocavities. *Applied Physics Letters*, 91(20):201111, 2007.
- [138] R. J. Glauber. The quantum theory of optical coherence. *Physical Review*, 130:2529–2539, 1963.
- [139] C. Matthiesen, M. Geller, C. H. H. Schulte, C. Le Gall, J. Hansom, Z. Li, M. Hugues, E. Clarke, and M. Atatüre. Phase-locked indistinguishable photons with synthesized waveforms from a solid-state source. *Nature Communications*, 4:1600, 2013.
- [140] M. Metcalfe, G. S. Solomon, and J. Lawall. Heterodyne measurement of resonant elastic scattering from epitaxial quantum dots. *Applied Physics Letters*, 102(23):231114, 2013.
- [141] S. M. Ulrich, S. Ates, S. Reitzenstein, A. Löffler, A. Forchel, and P. Michler. Dephasing of triplet-sideband optical emission of a resonantly driven InAs/GaAs quantum dot inside a microcavity. *Physical Review Letters*, 106:247402, 2011.
- [142] A. Ulhaq, S. Weiler, S. M. Ulrich, R. Rossbach, M. Jetter, and P. Michler. Cascaded single-photon emission from the Mollow triplet sidebands of a quantum dot. *Nature Photonics*, 6:238, 2012.
- [143] Y. He, Y.-M. He, J. Liu, Y.-J. Wei, H. Y. Ramírez, M. Atatüre, C. Schneider, M. Kamp, S. Höfling, C.-Y. Lu, and J.-W. Pan. Dynamically controlled resonance fluorescence spectra from a doubly dressed single InGaAs quantum dot. *Physical Review Letters*, 114:097402, 2015.
- [144] H. Paul. Interference between independent photons. *Reviews of Modern Physics*, 58:209–231, 1986.
- [145] R. Hanbury Brown and R. Q. Twiss. A new type of interferometer for use in radio astronomy. *The London, Edinburgh, and Dublin Philosophical Magazine and Journal of Science*, 45:663–682, 1954.
- [146] R. Hanbury Brown and R. Q. Twiss. Correlation between photons in two coherent beams of light. *Nature*, 177:27–29, 1956.

- [147] R. Hanbury Brown and R. Q. Twiss. A test of a new type of stellar interferometer on sirius. *Nature*, 178:1046–1048, 1956.
- [148] J. T. Höffges, H. W. Baldauf, T. Eichler, S. R. Helmfrid, and H. Walther. Heterodyne measurement of the fluorescent radiation of a single trapped ion. *Optics Communications*, 133:170, 1997.
- [149] H. Walther. Single atom experiments in cavities and traps. *Proceedings of the Royal Society of London A: Mathematical, Physical and Engineering Sciences*, 454(1969):431–445, 1998.
- [150] J. Claudon, J. Bleuse, N. S. Malik, M. Bazin, P. Jaffrennou, N. Gregersen, C. Sauvan, Ph. Lalanne, and J. M. Gérard. A highly efficient single-photon source based on a quantum dot in a photonic nanowire. *Nature Photonics*, 4:174, 2010.
- [151] A. V. Kuhlmann, J. Prechtel, J. Houel, A. Ludwig, D. Reuter, A. D. Wieck, and R. J. Warburton. Transform-limited single photons from a single quantum dot. *Nature Communications*, 6:8204, 2015.
- [152] S. Weiler, D. Stojanovic, S. M. Ulrich, M. Jetter, and P. Michler. Postselected indistinguishable single-photon emission from the Mollow triplet sidebands of a resonantly excited quantum dot. *Physical Review B*, 87:241302, 2013.
- [153] L. Monniello, A. Reigue, R. Hostein, A. Lemaître, A. Martinez, R. Grousson, and V. Voliotis. Indistinguishable single photons generated by a quantum dot under resonant excitation observable without postselection. *Physical Review B*, 90:041303, 2014.
- [154] T. Legero, T. Wilk, M. Hennrich, G. Rempe, and A. Kuhn. Quantum beat of two single photons. *Physical Review Letters*, 93:070503, 2004.
- [155] A. Kiraz, M. Ehrl, Th. Hellerer, Ö. E. Müstecaplıoğlu, C. Bräuchle, and A. Zumbusch. Indistinguishable photons from a single molecule. *Physical Review Letters*, 94:223602, 2005.
- [156] R. Lettow, Y. L. A. Rezus, A. Renn, G. Zumofen, E. Ikonen, S. Götzinger, and V. Sandoghdar. Quantum interference of tunably indistinguishable photons from remote organic molecules. *Physical Review Letters*, 104:123605, 2010.
- [157] F. Dubin, D. Rotter, M. Mukherjee, S. Gerber, and R. Blatt. Single-ion two-photon source. *Physical Review Letters*, 99:183001, 2007.
- [158] H. Bernien, L. Childress, L. Robledo, M. Markham, D. Twitchen, and R. Hanson. Two-Photon Quantum Interference from Separate Nitrogen Vacancy Centers in Diamond. *Physical Review Letters*, 108:043604, 2012.
- [159] J. Bylander, I. Robert-Philip, and I. Abram. Interference and correlation of two independent photons. *The European Physical Journal D - Atomic, Molecular, Optical and Plasma Physics*, 22(2):295–301, 2003.
- [160] R. B. Patel, A. J. Bennett, K. Cooper, P. Atkinson, C. A. Nicoll, D. A. Ritchie, and A. J. Shields. Postselective two-photon interference from a continuous nonclassical stream of photons emitted by a quantum dot. *Physical Review Letters*, 100:207405, 2008.
- [161] R. B. Patel, A. J. Bennett, I. Farrer, C. A. Nicoll, D. A. Ritchie, and A. J. Shields. Two-photon interference of the emission from electrically tunable remote quantum dots. *Nature Photonics*, 4(9):632–635, 2010.
- [162] A. Lebreton, I. Abram, R. Braive, I. Sagnes, I. Robert-Philip, and A. Beveratos. Unequivocal differentiation of coherent and chaotic light through interferometric photon correlation measurements. *Physical Review Letters*, 110:163603, 2013.
- [163] L. Mandel. Coherence and indistinguishability. *Optics Letters*, 16(23):1882–1883, 1991.
- [164] C. K. Hong, Z. Y. Ou, and L. Mandel. Measurement of subpicosecond time intervals between two photons by interference. *Physical Review Letters*, 59:2044–2046, 1987.
- [165] L. Mandel and E. Wolf. *Optical Coherence and Quantum Optics*. Cambridge University Press.
- [166] S. Gerber, D. Rotter, M. Hennrich, R. Blatt, F. Rohde, C. Schuck, M. Almendros, R. Gehr, F. Dubin, and J. Eschner. Quantum interference from remotely trapped ions. *New Journal of Physics*, 11(1):013032, 2009.
- [167] L. Mandel. Quantum effects in one-photon and two-photon interference. *Reviews of Modern Physics*, 71:S274–S282, 1999.

- [168] K. Konthasinghe, M. Peiris, Y. Yu, M. F. Li, J. F. He, L. J. Wang, H. Q. Ni, Z. C. Niu, C. K. Shih, and A. Muller. Field-field and photon-photon correlations of light scattered by two remote two-level InAs quantum dots on the same substrate. *Physical Review Letters*, 109:267402, 2012.
- [169] M. Halder, A. Beveratos, R. T. Thew, C. Jorel, H. Zbinden, and N. Gisin. High coherence photon pair source for quantum communication. *New Journal of Physics*, 10(2):023027, 2008.
- [170] M. Halder, A. Beveratos, N. Gisin, V. Scarani, C. Simon, and H. Zbinden. Entangling independent photons by time measurement. *Nature Physics*, 3:692–695, 2007.
- [171] M. Larqué, A. Beveratos, and I. Robert-Philip. Entangling single photons on a beamsplitter. *The European Physical Journal D*, 47(1):119–125, 2008.
- [172] H. Jayakumar, A. Predojević, T. Kauten, T. Huber, G. S. Solomon, and G. Weihs. Time-bin entangled photons from a quantum dot. *Nature Communications*, 5:4251, 2014.
- [173] C. H. H. Schulte, J. Hansom, A. E. Jones, C. Matthiesen, C. Le Gall, and M. Atatüre. Quadrature squeezed photons from a two-level system. *Nature*, 525:222–225, 2015.
- [174] D. F. Walls and P. Zoller. Reduced quantum fluctuations in resonance fluorescence. *Physical Review Letters*, 47:709–711, 1981.
- [175] Z. Y. Ou, C. K. Hong, and L. Mandel. Detection of squeezed states by cross correlation. *Physical Review A*, 36:192–196, 1987.
- [176] W. Vogel. Homodyne correlation measurements with weak local oscillators. *Physical Review A*, 51:4160–4171, 1995.
- [177] S. Gerber, D. Rotter, L. Slodička, J. Eschner, H. J. Carmichael, and R. Blatt. Intensity-field correlation of single-atom resonance fluorescence. *Physical Review Letters*, 102:183601, 2009.
- [178] A. J. Bennett, J. P. Lee, D. J. P. Ellis, I. Farrer, D. A. Ritchie, and A. J. Shields. A semiconductor photon-sorter. *Nature Nanotechnology*, 11:857–860, 2016.
- [179] U. Rengstl, M. Schwartz, T. Herzog, F. Hargart, M. Paul, S. L. Portalupi, M. Jetter, and P. Michler. On-chip beamsplitter operation on single photons from quasi-resonantly excited quantum dots embedded in gaas rib waveguides. *Applied Physics Letters*, 107(2):021101, 2015.
- [180] M. Kaniber, F. Flassig, G. Reithmaier, R. Gross, and J. J. Finley. Integrated superconducting detectors on semiconductors for quantum optics applications. *Applied Physics B*, 122(5):1–10, 2016.
- [181] N. Ptrljaga, C. Benthams, J. O’Hara, B. Royall, E. Clarke, L. R. Wilson, M. S. Skolnick, and A. M. Fox. On-chip interference of single photons from an embedded quantum dot and an external laser. *Applied Physics Letters*, 108(25):251101, 2016.
- [182] M. M. Karow, P. Munnelly, T. Heindel, M. Kamp, S. Höfling, C. Schneider, and S. Reitzenstein. On-chip light detection using monolithically integrated quantum dot micropillars. *Applied Physics Letters*, 108(8):081110, 2016.
- [183] C. P. Dietrich, A. Fiore, M. G. Thompson, M. Kamp, and S. Höfling. GaAs integrated quantum photonics: Towards compact and multi-functional quantum photonic integrated circuits. *Laser and Photonics Reviews*, 7 2016.
- [184] M. Schwartz, U. Rengstl, T. Herzog, M. Paul, J. Kettler, S. L. Portalupi, M. Jetter, and P. Michler. Generation, guiding and splitting of triggered single photons from a resonantly excited quantum dot in a photonic circuit. *Optics Express*, 24(3):3089–3094, 2016.

La fluorescence de résonance des boîtes quantiques semiconductrices pour la génération de photons indiscernables

Les boîtes quantiques uniques de semiconducteurs, qui sont considérées comme des systèmes à deux niveaux dans le modèle de l'atome artificiel, sont des structures prometteuses pour la réalisation de dispositifs intégrés tels que des sources de photons uniques pour des applications en information quantique. Cependant, contrairement à de véritables atomes, ce sont des systèmes de matière condensée qui souffrent du couplage à leur environnement solide, conduisant à une dégradation de la cohérence des photons émis. Une façon d'éviter ce couplage, et ainsi d'améliorer la cohérence des photons jusqu'à celle imposée par la limite radiative $T_2=2T_1$, est d'exciter une boîte quantique strictement à la résonance à basse température. À l'aide d'un montage expérimental permettant de découpler spatialement les chemins d'excitation et de détection, nous avons montré qu'un contrôle fin de l'environnement électrostatique lié au dopage résiduel de ces nanostructures reste néanmoins un enjeu majeur pour répondre au problème largement rencontré de l'inhibition de la fluorescence de résonance des boîtes quantiques. Parallèlement, grâce à des expériences d'optique quantique et de spectroscopie optique de haute résolution, nous avons montré que le régime de diffusion Rayleigh résonnante, où les boîtes quantiques émettent des photons uniques ayant le temps de cohérence du laser d'excitation, constitue une voie originale pour l'élaboration de sources "ultra-cohérentes" de photons uniques présentant de forts degrés d'indiscernabilité. Dans ce régime où le laser contrôle la cohérence des photons et où la limite radiative devient alors une contrainte secondaire, deux photons émis successivement par une même boîte quantique restent indiscernables sur des échelles de temps jamais obtenues auparavant pour un nano-émetteur solide (jusqu'à une dizaine de nanosecondes, à comparer aux temps de vie et de décohérence des porteurs dans une boîte quantique de l'ordre de la centaine de picosecondes).

Mots-clés: boîtes quantiques, système à deux niveaux, limite radiative, fluorescence de résonance, diffusion Rayleigh résonnante, photons uniques, photons indiscernables.

The resonance fluorescence of single semiconductor quantum dots for the generation of indistinguishable photons

Single semiconductor quantum dots, which are considered as two-level systems in the artificial atom model, are promising structures for the realization of integrated devices such as single photon sources for quantum information applications. However, contrary to genuine atoms, they are condensed matter systems which suffer from the coupling to their solid environment, leading to a degradation of the coherence of the emitted photons. One possibility to avoid this coupling, thereby improving the coherence of the photons until the one imposed by the radiative limit $T_2 = 2T_1$, is to perform strictly resonant excitation of a quantum dot at low temperature. Using an experimental setup that spatially decouples the excitation and detection paths, we showed that a fine control of the electrostatic environment related to the nanostructures residual doping remains a major challenge to answer the widely encountered problem of the inhibition of the resonance fluorescence of a quantum dot. Meanwhile, thanks to quantum optics experiments and high resolution optical spectroscopy, we demonstrated that the resonant Rayleigh scattering regime where quantum dots emit single photons with the laser coherence time, paves the way to the development of "ultra-coherent" sources of single photons with high degrees of indistinguishability. In this regime where the laser tailors the coherence of the photons and where the radiative limit becomes a secondary requirement, two photons emitted successively by the same quantum dot are indistinguishable on time scales never obtained before for a solid nano-emitter (up to ten nanoseconds, comparing to the carriers lifetime and decoherence time of about a hundred of picoseconds).

Keywords: quantum dots, two-level system, radiative limit, resonance fluorescence, resonant Rayleigh scattering, single photons, indistinguishable photons.